PROPERTIES AND PERFORMANCE OF A CERAMIC COMPOSITE COMPONENT

by

Thomas John Dunyak

Dissertation submitted to the Faculty of the

Virginia Polytechnic Institute and State University

in partial fulfillment of the requirements for the degree of

DOCTOR OF PHILOSOPHY

in

Engineering Mechanics

APPROVED:

W. W. Stinchcomb, Chairman

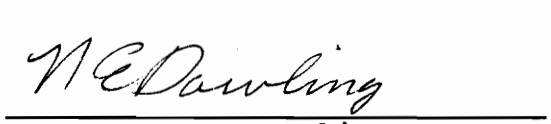

N. E. Dowling

D. P. H. Hasselman

D. T. Mook

K. L. Reifsnider

February, 1991

Blacksburg, Virginia

PROPERTIES AND PERFORMANCE OF A CERAMIC COMPOSITE COMPONENT

by

Thomas John Dunyak

Committee Chairman: Wayne W. Stinchcomb

Engineering Science and Mechanics

(ABSTRACT)

This dissertation culminates a three year research program investigating the properties and performance of a tubular, ceramic composite component. Eight test specimens were fabricated using an injection molding process with a borosilicate glass matrix reinforced with chopped graphite fibers. These specimens were then tested under quasi-static and cyclic loading at room temperature.

Due to the infancy of CMC materials and, especially, CMC components, the program included a very broad-based investigation into many areas which are considered well-established for more conventional materials, and a very extensive and diverse set of achievements were realized. A tubular CMC test specimen representing an engineering component was designed and fabricated. A high

temperature multiaxial test facility for ceramic matrix composite components was developed and installed at Virginia Tech. Nondestructive and destructive test methods for CMC components were developed, and a thorough investigation of the failure mechanisms in injection molded CMC tubes subjected to room temperature, quasi-static and cyclic loading was conducted in spite of a very limited quantity of material. As a result of this investigation, performance limiting defects in the injection molded tubes were identified. In addition, a generalized modeling approach was investigated for the analysis of complex, composite components which includes the effects of damage development under static and cyclic loading. All of these topics are discussed in detail in this dissertation.

ACKNOWLEDGEMENTS

It is impossible to acknowledge all of those people who have made this program of study possible. However, the following people deserve special recognition for their support and inspiration.

Dr. Stinchcomb and Dr. Reifsnider who provided a delicate balance between inspiring me to tackle the world and keeping me focused on the problems at hand. Throughout my entire three year stay at Virginia Tech, they always treated me as a full-fledged colleague and, more importantly, as a friend.

Dr. Dowling, Dr. Hasselman, and Dr. Mook for serving as committee members and for their advice throughout this program.

The ESM Faculty for their outstanding instruction and genuine interest in the well-being of their students. I didn't quite realize the quality of the education I had received until I left Tech and compared my background to that of my peers.

Dr. Duke and his graduate students for their help and guidance with the wide variety of NDE methods we investigated.

Barb Wengert and Shelia Collins for their understanding and assistance when it came to answering phone calls, leaving messages, typing reports, or whatever.

The wide group of graduate students who provided everything from technical support in the laboratories to moral support at the Balcony on Friday afternoons.

My parents, John and Nancy Dunyak, for their continuous encouragement and inspiration from the first day I stepped onto a school bus at age six. After 25 years of schooling, they are still asking me how my school work is going.

Most importantly, my wife, Terri, and daughter, Ashley, for putting their life on hold so that I could fulfill a dream.

TABLE OF CONTENTS

LIST OF FIGURES

LIST OF TABLES

1.0 INTRODUCTION

The art and science associated with ceramic composites has reached the critical threshold of large scale applications to primary engineering structures. Hence, many applications associated with aircraft engines, heat exchangers, regenerators, turbines, and heat engines (to name a few) are being planned. One of the primary constraints on making this major step to applications is the extent to which the associated technical community can make the transition from properties of materials to the performance of engineering components.

Making this transition requires comprehensive characterization and understanding (i.e., philosophy and rigorous modeling) of long-term behavior. For example, information from quasi-static tests, modulus of rupture tests and fracture toughness tests is not sufficient to design a complex component such as a heat exchanger tube which may experience multiaxial stresses and anisotropic fibrous reinforcement. This program has been a first step directed towards meeting these needs for the transition from properties to performance. In general, the program was a pioneering effort at Virginia Tech in the mechanical characterization of ceramic composite components. The program extended beyond the limited characterization of small samples and coupons to the comprehensive mechanical

characterization of a complex engineering component, a tube, subjected to static and cyclic loading.

The general objective of the program was to develop the ability to characterize the properties and performance of injection molded ceramic composite tubes reinforced with chopped fibers subjected to static and cyclic uniaxial loading at room temperature keeping in perspective the more general problems of continuous fiber reinforcement, multiaxial loadings, and elevated temperatures. Specific objectives included

- Development of a test specimen design based on detailed analyses of several design options and input from the specimen supplier and the test frame manufacturer.
- Development, installation, and verification of a high stiffness, biaxial test facility.
- Development, evaluation, and application of destructive and nondestructive test techniques for ceramic composite tubes.
- Investigation of damage development and failure mechanisms in a ceramic composite component under cyclic loadings.
- Development of strength prediction methods for reinforced injection molded ceramic composite components.

- Identification of needs and directions for future research.

All of these objectives were met and, in most cases, exceeded in this research program.

This dissertation presents the results of the above research program. As imagined, the program is a very broad based investigation into the performance of CMC components which is far different from most narrowly focused doctoral research programs. However, considering the infancy and very limited applications of CMC materials, this type program was essential in order to develop good, scientifically based methods for the investigation of CMC components.

This dissertation is divided into six main chapters associated with the characterization of ceramic composite components. Although each chapter in itself contains specific results and information, the collection of all six areas combine to develop a complete and unified research program. The six main chapters include literature review, specimen design and fabrication, test facility development, test method development, experimental program, and analytical modelling.

Following the introductory chapter, we present a detailed literature review related to this program. Due to the broad based, pioneering effort of the program, the

literature is profuse with articles and papers describing work with some, but limited, applicability to this program. Therefore, Chapter 2 is a summary of the more relevant papers. In some cases, a paper which had a very limited application or which duplicated the work in another paper was omitted.

Chapter 3 presents a detailed description of the specimen design and fabrication. Throughout this program, we found the fabrication process significantly affected the performance of the specimens. In all of the specimens, the critical material defects were the result of the fabrication process as opposed to the true performance limitations of the material system. Therefore, in order to fully understand the factors which limit performance, we must understand the specimen design and fabrication process. As a result, this chapter should not be overlooked.

One of the main objectives of the proposed program involved the development, installation and verification of a high stiffness, biaxial test facility for the testing of ceramic composites. The facility is completely computer controlled and includes an integrated data acquisition system. This test facility is truly unique, and therefore, a detailed description of the test facility and its capabilities are provided in Chapter 4.

As stated above, this work was a pioneering effort in the characterization of CMC components and required the development of destructive and nondestructive test methods. Chapter 5 provides a complete summary of the successful and unsuccessful test methods we attempted to develop or apply in this program. Out of all the work performed in this program, this chapter probably contains the most significant and useful information since these test methods are applicable to almost any CMC component.

Chapter 6 contains the results of the experimental program. Throughout this entire program, we have attempted to go beyond the simple characterization of the material in order to truly understand how the material behaves and what controls the performance of the material. This chapter summarizes our understanding of the material behavior. Although there are many things we still do not understand, this chapter presents a detailed description of the critical defects and how these defects effect the failure modes under quasi-static and cyclic loadings.

Chapter 7 presents an analytical approach for the analysis of damage progression in composite components with complex geometries and loadings. Originally, this approach was to be limited to injection molded CMC's under quasi-static loadings. However, the approach is general enough to be applied to a much broader range of problems as shown in Section 7.5. Unfortunately, this chapter is the

most incomplete portion of the entire program due to the limited number of specimens and the limited work scope in this area. As a result, the satisfaction of correlating predicted results with measured data is left for future research programs.

The final chapter summarizes the major results and reiterates the needs and directions for future work discussed throughout the main body of the text. Overall, we feel this dissertation contains a wealth of information which far exceeds the initial objectives of the program. Therefore, we invite the reader to sit back and enjoy.

2.0 LITERATURE REVIEW

The field of ceramic matrix composites is a new but rapidly growing field. As a result, the conferences held throughout the country are presenting an increased number of papers related to ceramic matrix composites. The typically polymer based composite conferences are routinely holding sessions on high temperature composites. In addition, the typically sintered ceramics conferences are holding sessions on reinforced ceramics. All of this attention directed toward ceramic composites is leading to a virtual explosion in the amount of information available in the open literature, and this information explosion in the area of ceramic matrix composites will continue to grow. Therefore, this literature review is simply a snapshot of the current literature applicable to this research.

Historically, ceramic composites have been approached from two separate directions. On one hand, parts of the traditional composites communities have turned their attention to high temperature composites. On the other hand, the sintered ceramics communities have looked to fiber reinforcements as a means of increasing ceramic toughness. As the field continues to grow and mature, these two directions are blending, and a specific community

dedicated to the development of ceramic matrix composites is forming.

Since both of these areas are well established, the literature is profuse with information on composites and ceramics. Unfortunately, most of this information can not be applied directly to ceramic composites. For example, consider the development of test methods for tensile strength. ASTM has established well defined guidelines for the characterization of tensile strength of polymeric composites (1). Similarly, the ceramics community routinely measures tensile strength at elevated temperatures. Unfortunately, the two procedures are different, and neither method directly applies to ceramic matrix composites. For polymeric composites, ASTM requires flat specimens loaded in uniaxial tension. However, precision alignment and gripping in a high temperature environment are not covered. The elevated temperature tensile strength of sintered ceramics is typically measured in a flexure mode due to the brittleness of the material and the gripping limitations. However, flexure testing is totally unacceptable for composites. Eventually, the two procedures must be integrated, and the resulting problem areas resolved. The ceramics composites community is just beginning to tackle these types of issues, and although the field is rapidly growing, the amount of current literature directly applicable to ceramic composites is limited.

This chapter will provide a detailed review of literature that directly applies to injection molded ceramic composite components. The remainder of this appendix will be grouped into five main areas. The first area will review test methods and specimen design. The second area will cover nondestructive test methods, and the third section will describe damage characterization under long term cyclic loading. The fourth section will review tensile strength prediction methods for injection molded components, and the final section will present a brief summary.

2.1 Test Methods and Specimen Design

The majority of high temperature tests conducted on ceramic matrix composites still consist of flexural loading of beam specimens. For example, References 2 through 6 use flexure specimens as a primary means of measuring quasi-static and fatigue properties. Several advantages make flexure testing extremely attractive. First, flexure tests require a relatively small amount of material compared to other types of mechanical tests, and ceramic composites are very expensive. Second, the fixturing is very simple and capable of very precise alignment. Relatively low loads are required for flexure testing. As a result, the fixturing can be fabricated with high

temperature materials which are capable of withstanding the test environment. In addition, since the loads are small and the deflections large, the crosshead deflection provides a good measurement of the specimen deflection which eliminates the need for high temperature extensometry.

Although these advantages contribute to a relatively simple and inexpensive test, they do not contribute to the quality of data produced by a flexure test. Flexural loading generates nonuniform stress and strain fields throughout the gage section of the specimen, and local failures can significantly change these fields. For example, as the outer ply on the tensile side of a specimen fails, the neutral axis shifts and changes the stress and strain fields. As a result, very little specific data is produced beyond the initial failure. Due to the limitations of flexure testing, investigators are turning towards uniaxial tension tests as the primary means of data generation, and several of the problem areas associated with high temperature tension testing are now being addressed.

References 7 through 11 discuss elevated testing techniques for uniaxial tension or fatigue. All the authors except Southern Research Institute (7) recommend a rigid gripping system with precision alignment capabilities. SRI incorporates a flexible alignment system

with a chain pivot to eliminate bending. Although the flexible system provides better alignment, it is difficult to use. In addition, the flexible system can not handle compressive loadings and is limited to a loading frequency of 30 seconds per cycle which does not permit high cycle fatigue testing. All of these researchers located the grips outside the heating unit.

Most authors incorporated some type of radiant heating unit. These units are relatively common and can be purchased from a variety of suppliers. Bartolotta et. al. (8) have developed an induction heating system for high temperature testing. They have shown the induction system provides better specimen access and thermal control without affecting the material properties of the specimen (12). Holmes et. al. (9) used a combination induction-radiant heating system. A SiC susceptor is placed around the specimen and inductively heated. The SiC susceptor then radiantly heats the gage length of the specimen. Holmes claims this system provides excellent temperature control, minimal furnace interference, and can be used for any composite system.

Most investigators used commercially available contacting extensometers. However, in some cases, the extensometers were modified with a counter balance to improve attachment or reduce out of plane loadings. Holmes et. al. (9) designed an new counter-force extensometer

arrangement (13) to balance the bending moment induced by the extensometer rods. The tips of the extensometer and counter-loading rods contacted shallow conical depressions ground into the edge of the specimen. These conical depressions served to accurately locate the contacting rods and to prevent possible extensometer slippage. Holmes et. al. also noted the extensometer should contact the face of the specimen as opposed to the edges when edge delamination could occur. Although optical and laser extensometry is quickly developing, it is interesting to note that none of the investigators used an optical or laser extensometer.

Although all of the specimens designs were different, most of the designs have some very similar characteristics. They all consist of a dog-boned shaped plate specimen with a uniform gage section. Holmes (9) and Bartolotta (8) were able to use shorter specimens due the small size of the induction furnaces. Most of the specimens contained a single radius in the transition region. However, the specimen presented by Holmes contained two radii. In most cases, end tabs were attached to the specimens to facilitate gripping.

Larsen, Stuchly, and Adams (14) at the IIT Research Institute also investigate the development of elevated test techniques. Generally, the methods they developed were significantly different from the methods described earlier. Therefore, their work will be considered separately.

Larsen, Stuchly, and Adams elected to place the grips inside the furnace. They believed this minimized the temperature gradients in the specimen, and reduced the amount of material required to perform the test. The testing in this program was limited to 900°C. Therefore, hot grips were more easily used. They also strongly recommended an optical extensometer for elevated strain measurements. Sighting flags were bonded to the specimen to provide a displacement window. Like all of the previous authors, a dog-boned specimen was developed for uniaxial tension testing. In addition, a typical SiC resistance furnace was used to heat the specimen and grips.

Although the work in references 7 through 14 relates to uniaxial testing of flat specimens as opposed to tubular components, many of these developments lay the groundwork for the development of test methods for complex engineering components. In addition, Ellis and Gayda (15) associated with the Advanced High Temperature Engine Materials Technology Program (HITEMP) have identified the development of structural benchmark test methods as a primary goal over the next several years, and high temperature, multiaxial loading of tubular components is of key interest. Unfortunately, as of the second HiTEMP Review in November of 1989, they have just started and have very little progress to report.

2.2 Nondestructive Examination Methods

The extension of nondestructive inspection (NDI) techniques from polymeric composites to ceramics composites has been relatively simple, and even the application of these techniques to complex engineering shapes is straight forward. Reference 16 provides an excellent review of relatively standard NDE techniques. Examples of the application of these techniques to ceramic composites are provided in references 17 to 24, and two papers reviewing techniques developed for polymeric short fiber composites are provided in References 25 and 26. Most of the current work in NDE of ceramic matrix composites deals with the development of advanced techniques such as computed tomography, acousto-ultrasonics, or microfocus x-rays. References 27 and 28 provide good summaries of the recent work in these advanced technology areas.

Although several NDI techniques have been developed to "see" into a material or specimen, very little work has been done to correlate the observed defects to the performance of ceramic matrix composites. For example, Kautz and Klima (28) have used microfocus x-rays to image voids and inclusions on the order of 20μm. However, most performance limiting defects are much larger than this size. In light of this gap between NDE results and performance reported in the literature, one of the main

goals of this program was to correlate the NDE results to performance and, based on this correlation, identify the critical defects which control performance.

2.3 Damage Process Characterization Under Long Term Cyclic Loading

In order to model the performance of injection molded ceramic matrix composites, the damage development process must be thoroughly characterized. However, not a single piece of literature on the damage development of injection molded ceramic matrix composites was located. Therefore, the literature search was expanded to include continuous fiber reinforced ceramics and short fiber polymeric composites. Three sources (29,30,9) were located which considered the long term behavior and damage development of continuous ceramic matrix composites under fatigue loading.

Minfold and Prewo (29) investigated the room temperature fatigue behavior of unidirectional and crossply laminates of different LAS glass matrices reinforced with continuous SiC fiber, and Prewo later continued this work in Reference 30. Holmes et. al. (9) considered the elevated temperature fatigue behavior of Si_3N_4 reinforced with unidirectional, continuous SCS-6 SiC fibers. In addition to simple stress-life results, all three of the references provide excellent information on stiffness

reduction versus cycles. Minford and Prewo also show residual strength curves for the SiC/LAS composites. None of these references investigated fatigue crack propagation through the specimens.

References 30 and 9 describe an apparent fatigue limit at the matrix cracking stress for unidirectional materials. For cyclic loads below the matrix cracking stress, the stiffness of the unidirectional material did not change as a function of cycles, and all of the specimens survived 10^5 cycles without a failure. In addition, the residual tensile strength after fatigue loading was approximately the same as the strength of the as-fabricated material. For cyclic loads above the matrix cracking stress, all the unidirectional specimens failed in fatigue and showed stiffness degradations throughout the test.

Several sources were located on the damage development of short fiber polymeric composites (31-37). Two of these papers (36,37) were extremely informative and will be covered in greater detail. Wang and Chim (36) investigated the fatigue damage and degradation in fiber reinforced sheet molding compound with random fiber distributions. The observed fatigue damage was generally characterized by microcrack density, characteristic crack length, and distribution of crack orientations. Typically, high cyclic stresses induced fatigue damage with large microcrack densities and short characteristic crack lengths. However,

low cyclic stresses tended to produce low microcrack densities and long characteristic cracks. In addition, the structural response of the SMC illustrated continuous stiffness degradations, and higher cyclic stresses produced higher magnitudes and rates of stiffness reduction and shorter fatigue lives.

Although the SMC is generally considered macroscopically isotopic, Wang and Chim observed several local phenomena which are expected to correlate more closely with the damage development in injection molded components. In matrix dominated areas, the microcracking and crack propagation was found to be predominantly normal to the loading direction. In fiber dominated regions with fibers oriented parallel to the loading direction, the microcracks developed mainly in the matrix parallel to the loading. However, the microcracks had very short lengths limited by the interfiber spacing. In a chopped fiber strand oriented at an angle to the loading direction, microcracks with long characteristic lengths initiated and grew along the fiber/matrix interface. Overall, the predominate failure modes were matrix failure and fiber pullout. Fiber fractures were rarely observed in the SMC material.

Lang, Manson, and Hertzberg (37) investigated fatigue fracture in injection molded polymeric composites. Their specimens had known non-homogeneous fiber orientations

throughout the specimens. They looked at several types of specimens with variations in fiber volume, matrix ductility, and fibre-matrix adhesion. Depending on the combination of these parameters, completely different fracture patterns were observed. For example, a specimen with a "semi-ductile" matrix, 18% fiber volume fraction, and "good" fiber-matrix adhesion exhibited crack growth perpendicular to the loading direction regardless of the fiber orientations. However, the same material and geometry with 26% fiber volume showed crack growths parallel to the fiber orientations and parallel to the loading directions indicating failure at the fiber-matrix interface. A specimen with a "brittle" matrix, 18% fiber volume, and poor fiber-matrix adhesion also exhibited crack growth parallel to the fiber orientations and parallel to the loading directions. This review will focus on the results of the "brittle" matrix specimens.

SEM investigation of the fracture surfaces for the brittle matrix specimen indicates variations in the surface depending on fracture mode. Lang, Manson and Hertzberg considered three different fiber orientations with respect to the crack plane. In areas of fibers oriented at large angles to the crack plane, fiber pullout was much more apparent under monotonic or fast fracture loadings than under stable crack growth conditions. Detailed examination of the fiber-matrix interface regions also indicated

interface failure under fast fracture and matrix failure near the interface under stable crack propagation conditions. For fibers at intermediate angles to the crack plane, damage was predominantly characterized by shear failure of the fiber-matrix interface. In some cases, fiber failures due to bending were observed. For fibers at small angles to the crack plane, no significant differences in the fracture surfaces were observed between stable crack growth and fast fracture. In both cases, the damage was primarily characterized by failure of the fiber-matrix interface.

Overall, References 36 and 37 provide the best insight into the damage development process for injection molded composites. As shown in these papers, nonhomogeneous fiber orientations clearly have a significant effect of the failure process. For the case of injection molded ceramic composites, similar observations are required in order to characterize the damage development process under long term cyclic loading.

2.4 Tensile Strength Prediction Methods for Injection Molded Composites

The development of strength prediction methods for fiber reinforced injection molded composites is a very complicated yet relevant problem which has received little

attention. The application of strength prediction techniques to injection molded ceramic matrix composites has not been addressed at all. Typically, two different classifications of short fiber composites are considered. The first class considers short fibers which are aligned in the loading direction. The second class of problems considers randomly orientated short fiber composites which are isotropic in the plane of the specimen. Unfortunately, neither of these classifications directly applies to injection molded components where the flow of the molding compound generates non-uniform fiber orientations throughout the component.

This section will describe four general approaches to the short fiber problem. Although several papers exist for each approach, this review will be limited to seven papers which form the basis of these approaches. For each approach, a brief summary of the method will be presented. Then, the limitations of each approach and the applicability to injection molded ceramic matrix composites will be discussed.

One of the first strength prediction methods for short fiber composites was proposed by H. T. Hahn in October of 1975 (38). Hahn proposed that the uniaxial tensile strength (X) can be determined from

$$X = \int_0^{\pi} h(\theta) X_\theta d\theta \qquad (2.1)$$

where $h(\theta)$ is the through the thickness fiber distribution function and X_θ is the off-axis failure stress. The basic unit in this formulation is a ply reinforced with discontinuous fibers aligned in one direction. In Reference 38, Hahn shows relatively good correlation between the predicted and experimental strength data for random fiber composites. Hahn assumes the orientation of each ply in the laminate is arbitrary so that the laminate as a whole is isotropic in its plane. Unfortunately, this assumption is not valid for injection molded components. Due to the flow of the material, the laminate is not isotropic in its plane. Therefore, the theory must be modified to be used for fiber reinforced, injection molded components.

In 1981, Fukuda and Chou (39) proposed a theory for the strength of aligned short fiber composites based on a modified rule of mixtures approach. They proposed the uniaxial tensile strength (X) can be expressed as

$$X = \frac{\sigma_{fu}}{K} V_f + \sigma_m'(1-V_f) \qquad (2.2)$$

Where σ_{fu} is the ultimate tensile strength of the fiber, V_f is the fiber volume fraction, σ_m' is the matrix stress at

the ultimate tensile strain of the fibers, and K is the stress concentration of the fiber ends on an adjacent fiber. The stress concentration factor can then be found based on the work by Hedgepeth (40), Hedgepeth and Van Dyke (41), or Fukuda and Kawata (42). Fukuda and Chou also determined probability distributions for the alignment of fiber ends. In 1982, Manders and Chou (43) expanded this approach to include the probability of strength distributions along the length of the fibers.

Unfortunately, this method has three major assumptions which are violated in injection molded ceramic composites. First, Fukuda and Chou define σ_m' as the matrix stress at fiber failure thereby assuming the fibers fail before the matrix. In ceramic composites, generally the reverse is true, and the matrix fails before the fibers. Second, Fukuda and Chou assume the specimen fails entirely by fiber failure. However, for short fiber ceramic composites, fiber pullout may be the predominate failure mode. Lastly, the method is restricted to axially aligned fibers systems, and off-axis fiber orientations are not considered.

Sanadi and Piggott (44 and 45) proposed a similar approach based on the rule mixtures. In this case,

$$X = \beta_3\beta_4 V_f\sigma_{fu} + V_m\sigma_{mu} \qquad (2.3)$$

where β_3 is a fiber direction factor, β_4 is a fiber length factor, V_f is the fiber volume fraction, σ_{fu} is the ultimate fiber strength, V_m is the matrix volume fraction, σ_{mu} is the matrix stress at fiber failure. In reference 36, Sanadi and Pigott assume β_3 and β_4 are independent of each other. β_3 is based on matrix transformation equations, and β_4 is based on a shear lag analysis. Later, Sanadi and Piggott (45) combine the two factors in a slip coefficient. Although this approach eliminates the restriction of aligned fiber systems, the approach still does not consider fiber pullout, matrix failure prior to fiber failures, and non-homogeneous fiber distributions in the plane of the specimen.

S.S. Wang et. al. (46) approached the strength of randomly oriented sheet molding compound (SMC) from a fracture mechanics viewpoint. They considered the random short fiber SMC as a macroscopically planer, isotropic, elastic solid and determined the critical stress intensity factors, K_{IQ} and K_{IIQ}. They found both of these values were independent of crack length and could be used as material constants. For mixed-mode fracture, they found the stress intensity factors, K_I and K_{II}, follow the relationship:

$$(K_I/K_{IQ})+(K_{II}/K_{IIQ})^2=1 \qquad (2.4)$$

By modelling the SMC as an macroscopically isotropic solid, Wang et. al. smeared the local orientation effects into global fracture toughness values. Unfortunately, for the injection molded composite problem, the material is not macroscopically isotropic, and the local orientation effects dominate the failure. Therefore, this approach can not be used for the strength prediction of injection molded composites.

In 1987, Kageyama and Chou (47) also investigated the fracture toughness of short fiber composites. In this case, they considered whisker reinforced ceramic matrix composites and looked at the local effects of fiber orientations and locations. Their work incorporates a fracture mechanics analysis with both fiber pullout and crack deflection. Based on a distributed dislocation method, Kageyama and Chou calculated K_I and K_{II} as a function of fiber orientation. Once the fiber distribution is known, they can calculate an equivalent stress intensity factor, K_{eq}, and failure occurs when

$$K_{eq} > K_{cm} \tag{2.5}$$

where K_{cm} is the critical stress intensity factor for the matrix. Unfortunately, K_{cm} may be difficult to determine, and the interphase region may have an entirely different K_{cm} for fiber pullout than for crack deflection. In

addition, Kageyama and Chou limited their analysis to random fiber distributions and orientations. Therefore, the method must be applied to known, nonhomogeneous fiber distributions.

All of these methods assume a weakest link concept for specimen failure. In other words, once a single point fails on the specimen, the entire specimen fails. However, for injection molded components, a progressive failure may be more apparent. For example, locations with fibers oriented at 90 degrees to the loading axis may fail at relatively low loads. However, the load from the failed regions is simply transferred to locations with more highly aligned fibers, and complete failure of the component occurs at a much higher load than the initial failure. Unfortunately, analysis of a progressive failure is much more difficult than a weakest link analysis.

Overall, four different approaches to predict strength of aligned or random short fiber reinforced composites have been considered. Hahn's approach and Kageyama and Chou's approach may be expanded to injection molded composites. In both cases, the methods must be modified to include the effects of known fiber distributions and orientations. In addition, the question of progressive failure must be addressed.

2.5 Summary

This literature review has attempted to summarize the available literature which bears on this research effort. Several works were discussed in the areas of test methods, nondestructive examination and testing, strength prediction methods and damage development characterization. Although a significant amount of work has been completed in each of these areas, applications to injection molded ceramic matrix composites are very limited and sometimes nonexistent. Nevertheless, these works still provide a very strong foundation for the proposed research effort.

3.0 TEST SPECIMEN DESIGN, ANALYSIS AND FABRICATION

The main objective of this program is to initiate the transition from properties of laboratory coupons to the performance of engineering components. Therefore, a test specimen was designed which fully represents an engineering component. In this case, we selected a tubular configuration, and several variations of tubular test specimens were designed. All of the designs were then analyzed using half-length, axisymmetric finite element models to determine the stress distributions in the specimen. Based on the results from these analyses and on input from the grip manufacturer, we selected a final design for fabrication. The following three sections present detailed descriptions of the design options, analysis of each design, final design selection and fabrication of the selected design.

3.1 Specimen Design Options

Prior to developing potential specimen designs, a set of design criteria were established. Due to manufacturing considerations, the length of the tube cannot exceed 8.00 inches. In addition, the minimum length of the specimen is 6.00 inches in order to accommodate a 4.0 inch slot furnace and 1.0 inch length grip regions external to the furnace.

The gage section was limited to a 1.00 inch minimum inside diameter and a .100 inch maximum wall thickness. This combination of gage section diameter and wall thickness should provide a relatively uniform shear stress distribution through the thickness when subjected to torsional loadings. The furnace will produce a 1.00 inch uniform temperature region. As a result, a minimum 1.00 inch uniform gage length was specified. Finally, in order to reduce bending stresses due to the gripping loads, graphite plugs will be inserted in the ends of the tube.

Based on this set of criteria, four designs were developed and analyzed in detail. All of the designs consists of an 8.00 inch molded tube with a 1.0 inside diameter. However, all of the designs have slightly different grip and grip to gage section transition regions. The first design, shown in Figure 3.1, includes 1.4 inch long, molded conical grip regions which are tapered from 2.0 inches diameter at the outside end of the grip region to 1.50 inches diameter at the inside of the grip region adjacent to the transition region. The gage section is 2.0 inches long with a 0.100 inch wall thickness, and the transition from the grip region to the gage section is provided by a circular arc with an 8.92 inch radius. This circular arc forms a transition region which is tangent at both the gage section interface and the conical grip region interface. The specimen has 1.4 inch graphite plugs bonded

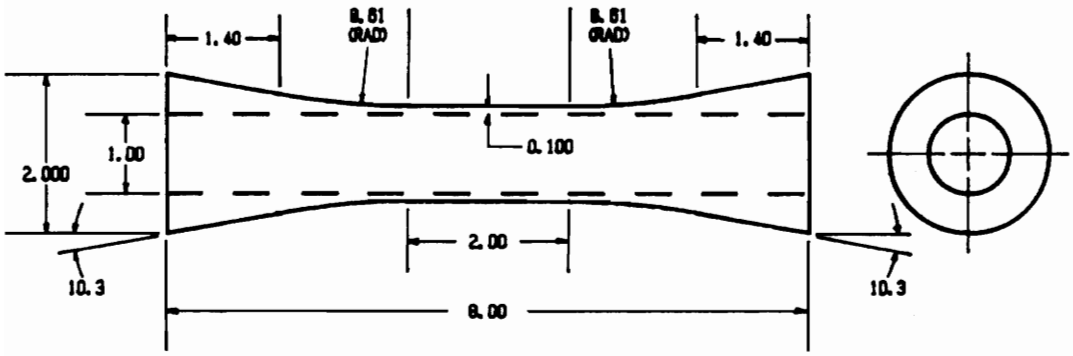

Figure 3.1 The Short Conical Specimen.

into the ends of the molded tube. This design configuration will be called the short conical specimen.

The second design, shown in Figure 3.2, is based on 1.9 inch long, molded conical grip regions which are tapered from 2.21 inches diameter at the outside end of the grip region to 1.50 inches diameter at the inside of the grip region adjacent to the transition region. The gage section is 1.0 inch long with a 0.100 inch wall thickness, and the transition from the grip region to the gage section is provided by a circular arc with an 8.61 inch radius. This circular arc also forms a transition region which is tangent at both the gage section interface and the conical grip region interface. The specimen has 1.9 inch graphite plugs bonded into the ends of the molded tube. This design configuration will be called the long conical specimen.

The third design contains a cylindrical grip region as shown in Figure 3.3. In this case, the molded grip regions are 1.35 inches in length with a uniform outside diameter of 1.52 inches. The grip regions are connected to a 2.00 inch gage section by circular transition regions with an 8.92 inch radius. The wall thickness in the gage section is also 0.100 inches. After molding, the grip regions are then machined to $1.5000 \pm .0005$ inch diameter, and 1.40 inch graphite plugs are bonded into the ends. This design will be termed the short cylindrical specimen.

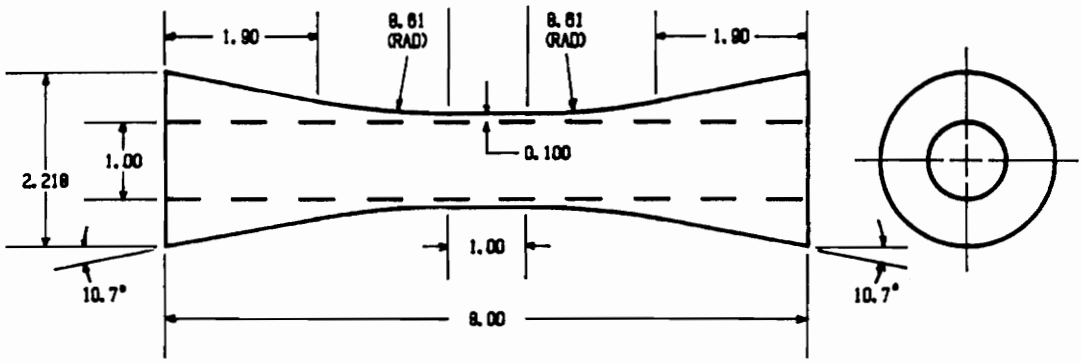

Figure 3.2 The Long Conical Specimen.

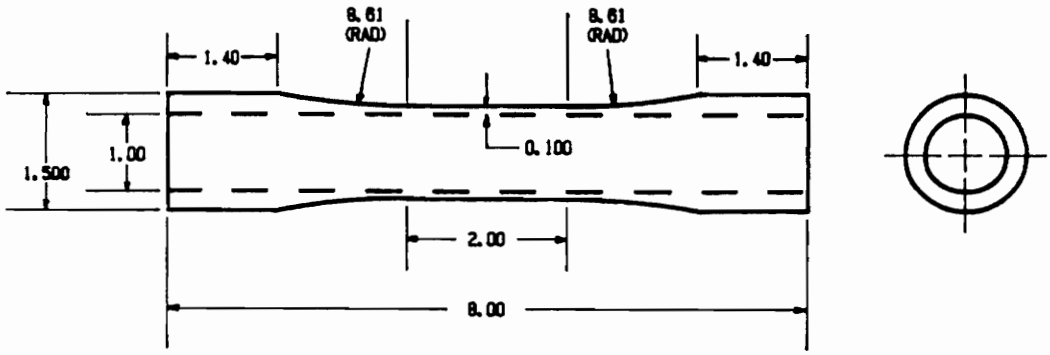

Figure 3.3 The Short Cylindrical Specimen.

The fourth design, shown in Figure 3.4, is based on longer cylindrical grip regions where the molded grip regions are 1.85 inches in length with a uniform outside diameter of 1.52 inches. The grip regions are connected to a 1.00 inch gage length by circular transition regions with an 8.92 inch radius. Again, the wall thickness in the gage section is 0.100 inches. After molding, the grip regions are then machined to 1.5000±.0005 inch diameter, and 1.90 inch graphite plugs are then bonded into the ends. This design will be termed the long cylindrical specimen.

3.2 Specimen Analysis

3.2.1 Model Development.

The four designs were analyzed using the ANSYS PC/LINEAR finite element code[48]. Half-length, axisymmetric models of the tube assemblies (including plugs) were developed for all four specimens using 4-node isoparametric elements (STIF 42) The finite element meshes for each of these models are shown in Figure 3.5.

Estimated material properties for HMU graphite fibers in a borosilicate glass matrix (0.5 inch fiber length, 25 to 30% fiber volume) were provide by UTRC (United Technologies Research Center) and are shown in Table 3.1. For this analysis, r, ϕ, and z are the cylindrical

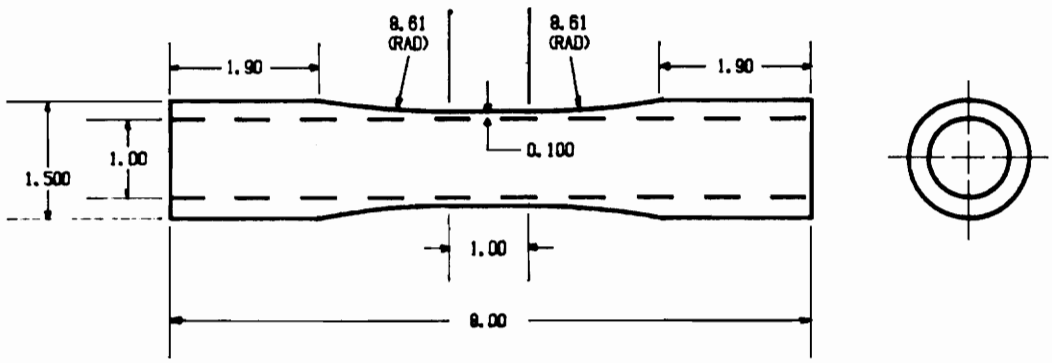

Figure 3.4 The Long Cylindrical Specimen.

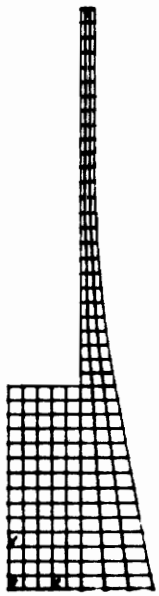

SHORT CONICAL MODEL

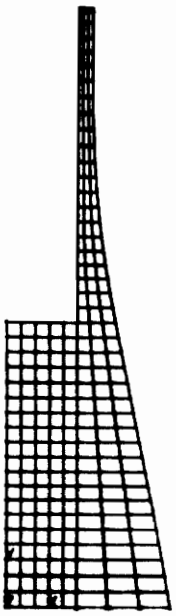

LONG CONICAL MODEL

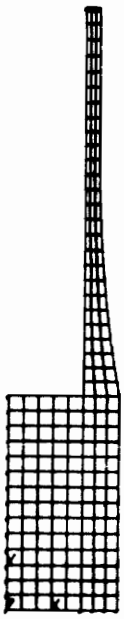

SHORT CYLINDRICAL MODEL

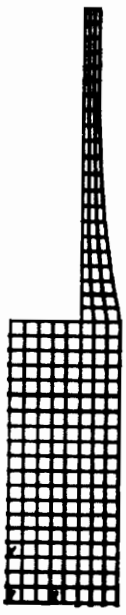

LONG CYLINDRICAL MODEL

Figure 3.5 The Finite Element Meshes.

Table 3.1 Material Properties.

HMU Graphite Fibers in a Borosilicate Glass Matrix

(0.5 inch Fiber Length, 25 to 30% Fiber Volume)

E_r = 5000 ksi	$G_{\phi z}$ = 800 ksi	$NU_{\phi z}$ = .30
E_ϕ = 8500 ksi	G_{rz} = 800 ksi	NU_{rz} = .43
E_z = 8500 ksi	$G_{r\phi}$ = 800 ksi	$NU_{r\phi}$ = .43

r-Ten Strength = 1.5 ksi rz-Shear Strength = 5.5 ksi

ϕ-Ten Strength = 15.0 ksi rϕ-Shear Strength = 5.5 ksi

z-Tensile Strength = 15.0 ksi

HLM Grade Graphite

E_r = 2300 ksi	$G_{\phi z}$ = 880 ksi	$NU_{\phi z}$ = .30
E_ϕ = 2300 ksi	G_{rz} = 880 ksi	NU_{rz} = .30
E_z = 2300 ksi	$G_{r\phi}$ = 880 ksi	$NU_{r\phi}$ = .30

r-Ten Strength = 2.5 ksi r-Comp Strength = 6.2 ksi

ϕ-Ten Strength = 2.5 ksi ϕ-Comp Strength = 6.1 ksi

z-Ten Strength = 2.5 ksi z-Comp Strength = 6.1 ksi

coordinates in the radial, hoop and axial directions respectively. The material properties of the plug are based on a HLM grade graphite supplied by the Great Lakes Carbon Corporation. These properties are also shown in Table 3.1. Although shear strengths of the graphite plugs were not available, the shear stresses in the graphite plugs were very small, and therefore, shear failure of the plug was not considered.

Two boundary conditions were imposed on the models. The first boundary condition corresponds to the base of the conical specimens contacting the bottom of the grip as a result of the preloading. In this case, we set $U_z=0$ along the base of the conical tube. The second boundary conditions arises from the symmetry of the specimen about the z-axis. In order to satisfy compatibility along the centerline of the specimen, we set $U_r=0$ at r=0. These boundary conditions are shown in Figure 3.6 for the long conical specimen.

The applied loads in the specimen consist of axial, tensile loads in the gage section and grip loads in the grip region. The axial loads in the gage section were applied by means of a distributed pressure load σ_z along the top of the specimen. The magnitude of the pressure loads equals the tensile failure stress of the material (15.0 ksi) in the gage section. For all of these designs, the 15.0 ksi failure stress is produced by a 5.18 kip axial

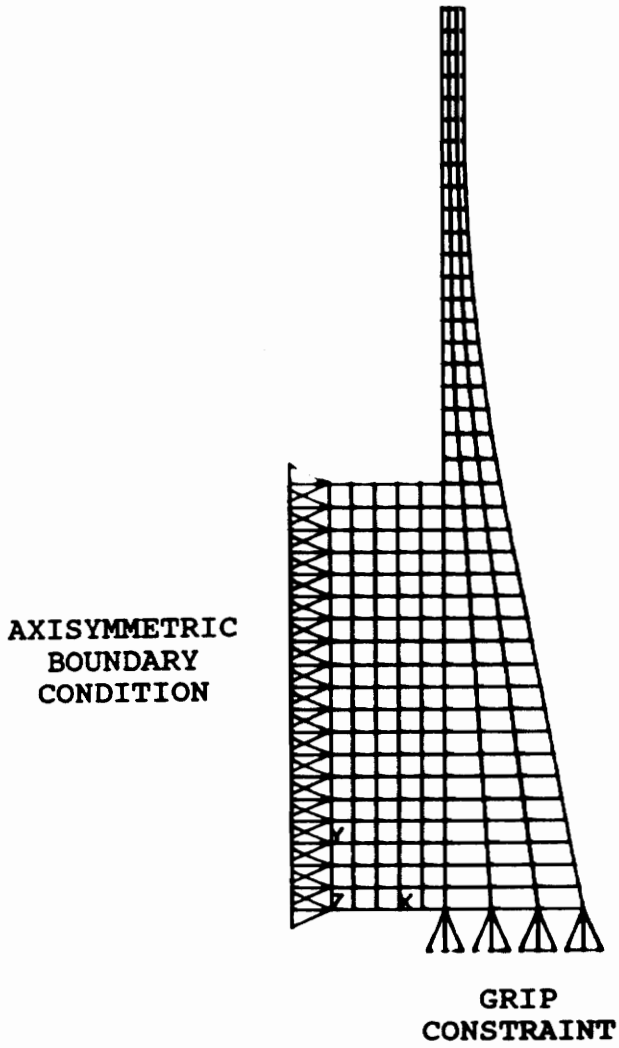

Figure 3.6 Boundary Conditions on the Long Conical Model.

load. The grip loads consist of uniformly distributed radial and axial loads at the grip interface nodes. In the case of the conical specimens, a compliant layer will be placed between the specimen and the grip housing in order to absorb some of the manufacturing variations. Therefore, as a first approximation, we assume this compliant layer cannot transfer shear or frictional forces leaving normal forces as the only type of forces acting across the interface.

For the two cylindrical specimens, the axial failure load (5.18 kips) must be counteracted by frictional forces along the gripping length. If we assume a friction factor of 0.6 between the tube material and the grip housing based on Reference 50 for glass on steel, the minimum radial load to hold the specimen is given by 5.18/0.6 or 8.64 kips. In order to provide some margin above the minimum grip load, we applied a 10 kip total radial, grip load on the model.

This completes the development of the ANSYS PC/LINEAR finite element models. All of these analyses were then executed on a HP VECTRA personnel computer. The results of these analyses are described in the following sections.

3.2.2 Design Allowables

In order to evaluate the acceptability of each the designs, two types of stress criteria must be specified.

First, we will specify a 1.05 maximum allowable stress concentration factor in the transition region near the gage section. Second, the allowable design stresses for the tube and the plug in the grip region must be specified. Unfortunately, the failure stresses provided by UTRC and Great Lakes Carbon are approximated and, in some cases, nonexistent. Therefore, we will develop a set of allowable design stresses based on the provided information. For the tube, we will specify a design tensile stress at 50% of the provided tensile strengths, and the design compressive stresses will specified at 100% of the tensile strengths. The design shear stresses will be 50% of the provided shear strengths. For the plug, the design tensile stresses will be equal to 50% of the provided tensile strengths, and the design compressive stresses will be equal to 50% of the provided compressive strengths. The design shear stress of the plug will be 25% of the provided tensile strength. The resulting allowable design stresses are in Table 3.2. Notice, these design stresses will only be used in the vicinity of the grip region and the plug since the applied stresses in the gage section equal the provided failure stress. As a result, the stress in the grip region should have a 100% safety factor at failure in the gage section.

Table 3.2 Allowable Design Stresses.

Component	Mode	Design Stress
Tube	r - Tens	0.75 Ksi
Tube	r - Comp	1.5 Ksi
Tube	ϕ - Tens	7.5 Ksi
Tube	ϕ - Comp	15.0 Ksi
Tube	z - Tens	7.5 Ksi
Tube	z - Comp	15.0 Ksi
Tube	rz - Shr	2.3 Ksi
Plug	r - Tens	1.2 Ksi
Plug	r - Comp	3.1 Ksi
Plug	ϕ - Tens	1.2 Ksi
Plug	ϕ - Comp	3.0 Ksi
Plug	z - Tens	1.2 Ksi
Plug	z - Comp	3.0 Ksi
Plug	rz - Shr	0.63 Ksi

3.2.3 Finite Element Results.

All four models were used for detailed analyses of the stress distributions due to two different load cases. The first load case considered grip loads only, and the second load case considered grip loads plus axial loads. The short models and the long conical model exhibited higher stresses than the long cylindrical models. In addition, the radial compressive stresses did not meet the design criteria in either the tube or the plug. Therefore, we will only present the results for the long cylindrical model.

The first load case we considered investigates the internal stresses in the long cylindrical model when subjected to radial grip loads only. The maximum stresses for this load case are presented in Table 3.3. We next considered the combined grip loads plus axial loads on the long cylindrical model, and Table 3.4 summarizes the maximum grip stresses for this load case. Notice, the predicted stresses from both load cases meet the allowable design stresses. Figure 3.7 presents the axial stress contours in the tube as a result of the combined loading. As shown in Figure 3.7, the stress concentration factor at the gage section is 1.03 which is acceptable. Therefore, this design meets all of the design criteria.

Table 3.3 Grip Stresses for the Long Cylindrical model Subjected to Grip Loads Only.

COMPONENT	STRESS	TENS/COMP	MAGNITUDE	ALLOWABLE
Tube	σ_r	Tens	0.07	0.75
Tube	σ_r	Comp	1.49	1.50
Tube	σ_z	Tens	0.48	7.50
Tube	σ_z	Comp	0.55	15.00
Tube	σ_ϕ	Tens	0.14	7.50
Tube	σ_ϕ	Comp	2.60	15.00
Tube	τ_{rz}	Shear	0.21	2.30
Plug	σ_r	Tens	0.13	1.20
Plug	σ_r	Comp	0.95	3.00
Plug	σ_z	Tens	0.04	1.20
Plug	σ_z	Comp	0.26	3.00
Plug	σ_ϕ	Tens	0.13	1.20
Plug	σ_ϕ	Comp	0.95	3.00
Plug	τ_{rz}	Shear	0.17	0.63

Table 3.4 Grip Stresses for the Long Cylindrical model Subjected to Grip and Axial Loads.

COMPONENT	STRESS	TENS/COMP	MAGNITUDE	ALLOWABLE
Tube	σ_r	Tens	0.13	0.75
Tube	σ_r	Comp	1.49	1.50
Tube	σ_z	Tens	7.37	7.50
Tube	σ_z	Comp	3.05	15.00
Tube	σ_ϕ	Tens	0.64	7.50
Tube	σ_ϕ	Comp	3.88	15.00
Tube	τ_{rz}	Shear	1.03	2.30
Plug	σ_r	Tens	0.00	1.20
Plug	σ_r	Comp	1.28	3.00
Plug	σ_z	Tens	1.15	1.20
Plug	σ_z	Comp	0.08	3.00
Plug	σ_ϕ	Tens	0.00	1.20
Plug	σ_ϕ	Comp	1.28	3.00
Plug	τ_{rz}	Shear	0.35	0.63

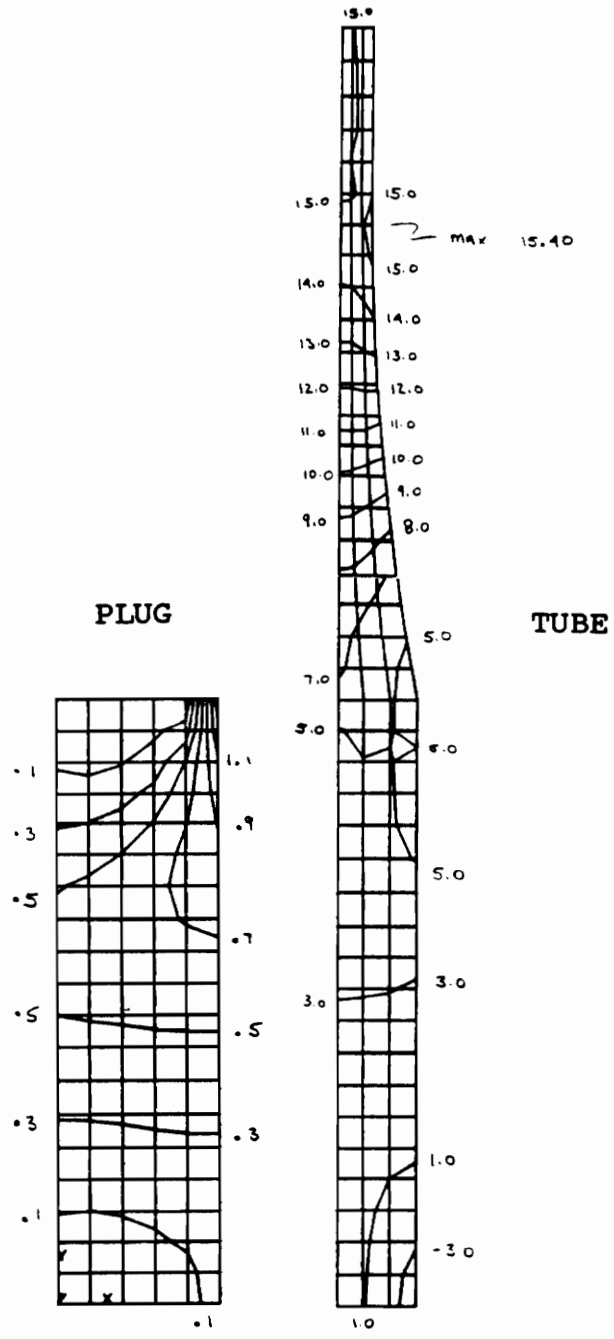

Figure 3.7 Axial Stress Contours for the Long Cylindrical Model Subjected to Grip Plus Axial Loads.

3.2.2 Model Verification

In order to verify the sensitivity of the models, several parameter studies were performed using the long cylindrical model. The first parameter study considered the effects of a refined mesh throughout the tube. The second parameter study investigated the effects of variations in the shear stiffness of the material. The shear stiffness used throughout the previous analyses was based on an engineering judgement by UTRC. Therefore, we considered the effect increasing the shear stiffness from 800 ksi to 2500 ksi. The third parameter study investigated the effects of the distribution of the applied loads along the grip length. For this study we considered the ramp loading distribution as opposed to a uniform distribution in the original model. Comparison of the results of each of these parameter studies to the original finite element results indicates none of the parameters had any significant effect on the stress distributions within the model.

As a final verification check, we compared the finite element results to the results of a plane deformation elasticity solution for an infinite tube. The development of the plane deformation elasticity solution is described in Reference 49. For the finite element results, we considered the load case with a 10 kip grip load uniformly

distributed throughout the grip region. The uniform grip load is equivalent to a uniform external pressure of 1.41 ksi. The elasticity solution considers an infinite tube with two layers subjected to a 1.41 ksi external pressure. The inner layer models the graphite plug with an inner radius of 0.00 inches and a outer radius of 1.00 inches. The outer layer models the reinforced tube with an inner radius of 1.00 inches and an outer radius of 1.50 inches. The material properties for two layers are identical to the material properties used in the finite element analyses. Figures 3.8 and 3.9 compare the compressive radial stresses and the compressive hoop stresses for the two solutions. The finite element results are taken at z=0.75 which corresponds to the center of the grip. Comparison of the two sets of results shows excellent agreement between the two solutions.

Based on these parameter studies and the verification check, we feel the finite element models are behaving correctly and are producing accurate results for the assumptions used in the development of the models. Unfortunately, some of these assumptions can not be verified with these types of analyses. The two main assumptions which fall into this category are the assumption of a uniform applied load distribution in the grips and the assumption of uniform material properties throughout the tube. As will be described later, the

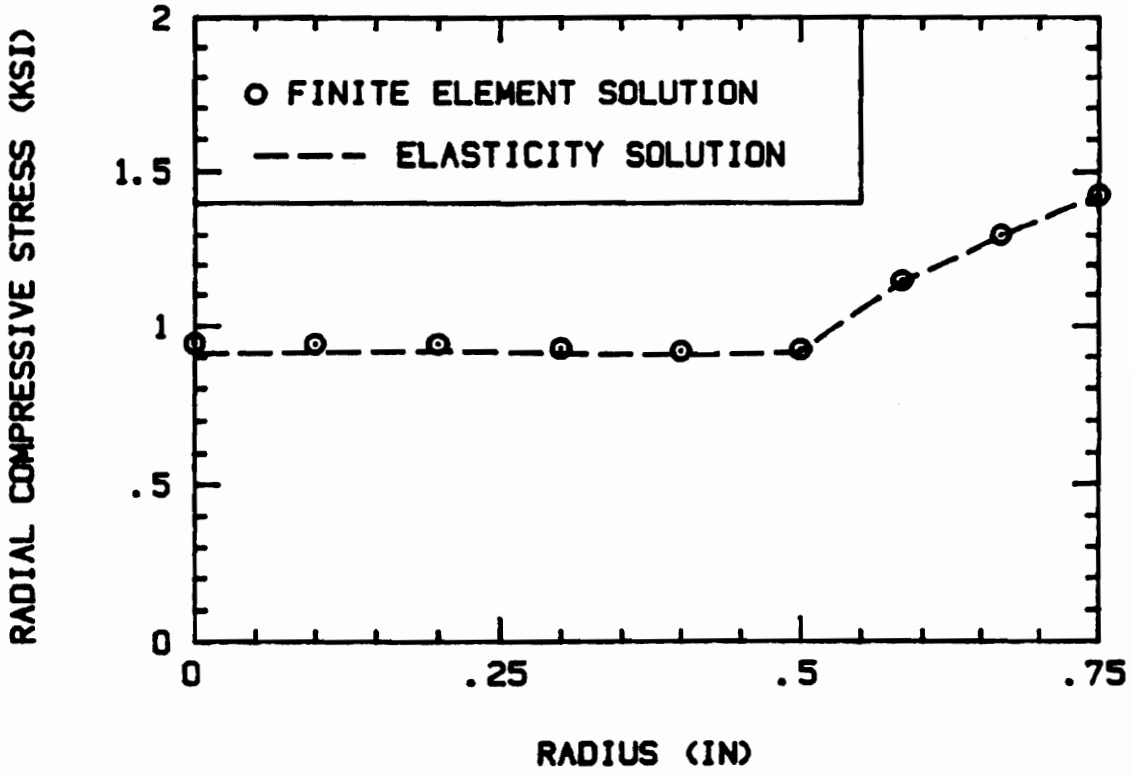

Figure 3.8 Comparison of the Compressive Radial Stresses for the Finite Element and Elasticity Solutions.

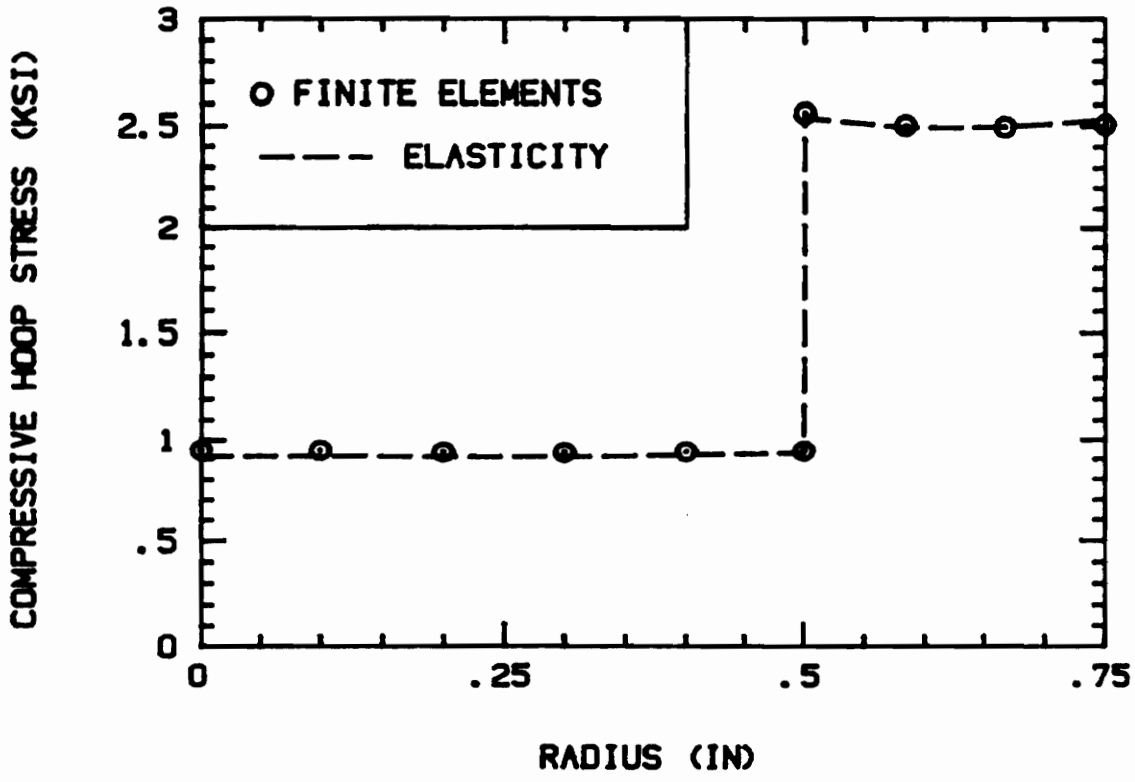

Figure 3.9 Comparison of the Compressive Hoop Stresses for the Finite Element and Elasticity Solutions.

material properties are not uniform along the length of the tube. As a result, the specimens consistently failed outside the gage section.

3.3 Final Design Selection

Based on the finite element analyses, the only design which satisfied all of the design criteria was the long cylindrical specimen. In addition, the grip manufacturer (Instron Corporation) strongly recommended a cylindrical grip region. They felt the conical designs require very high tolerances on the cone angle, and these tolerances are difficult, if not impossible, to hold. The cylindrical designs are not as sensitive to machining tolerances. Therefore, based on the finite element analyses and Instron's recommendation, the long cylindrical design was selected for fabrication.

3.4 Specimen Fabrication

Several methods were investigated for fabrication of the test specimens. These methods include chemical vapor infiltration (CVI), hot pressing, matrix transfer, and injection molding. All of the these methods are summarized in Reference 3. The first three methods can be used to fabricate a continuous fiber reinforced specimen. However,

injection molding is limited to chopped fiber materials. Although all of these methods are still in the highly developmental stages, the injection molding process is further developed and was capable of producing the complex tubular shape.

Therefore, in order to avoid a long and costly specimen fabrication program, the specimens were fabricated by an injection molding process with chopped fiber reinforcement. Unfortunately, an injection molding process offers very little control over fiber distribution and fiber directions in the finished specimen. The fiber distributions vary through the thickness, along the length and around the circumference. These variations are dependent on the flow of the composite compound into the mold. As a result, detailed identification of the fiber flow pattern is difficult but yet crucial. Variability between individual chopped fiber reinforced specimens will also be greater than that between continuous reinforced specimens. In order to avoid most of the fiber distribution concerns with chopped fibers and to work with a higher strength component, we recommend a change to a continuous fiber reinforced specimen when the material systems have been developed and fabrication methods have been successfully demonstrated.

Several material systems, including SiC/SiC, LAS Glass/SiC, LAS Glass/Graphite, and Borosilicate

Glass/Graphite, were considered for the specimens. SiC/SiC is not compatible with the injection molding process and was immediately ruled out. Although initially the LAS Glass systems were very attractive, the specimen manufacturer (United Technologies Research Center - UTRC) was not experienced with fabrication of complex tubular configurations with this material. However, UTRC did have experience with the fabrication of straight sided tubes with the Borosilicate Glass/Graphite system. Therefore, in order to avoid an extensive material development program, a Borosilicate Glass/Graphite system was selected for the specimens. Although the Borosilicate Glass/Graphite system is limited to 600°F, it does provide an excellent fiber reinforced brittle matrix composite for room temperature investigations. In addition, all of the damage characteristics of ceramic matrix composites including fiber bridging, fiber pullout, and fiber matrix disbonding can be observed in the Borosilicate Glass/Graphite system.

The details of the fabrication process are considered proprietary by UTRC and will not be covered in this report. However, since the fabrication process is critical to the state of material of the specimen, a brief summary of the process is provided. A diagram of the injection molding assembly is shown in Figure 3.10. Glass beads and chopped fibers are thoroughly mixed and then added to the reservoir. The mixture is heated to produce a viscous

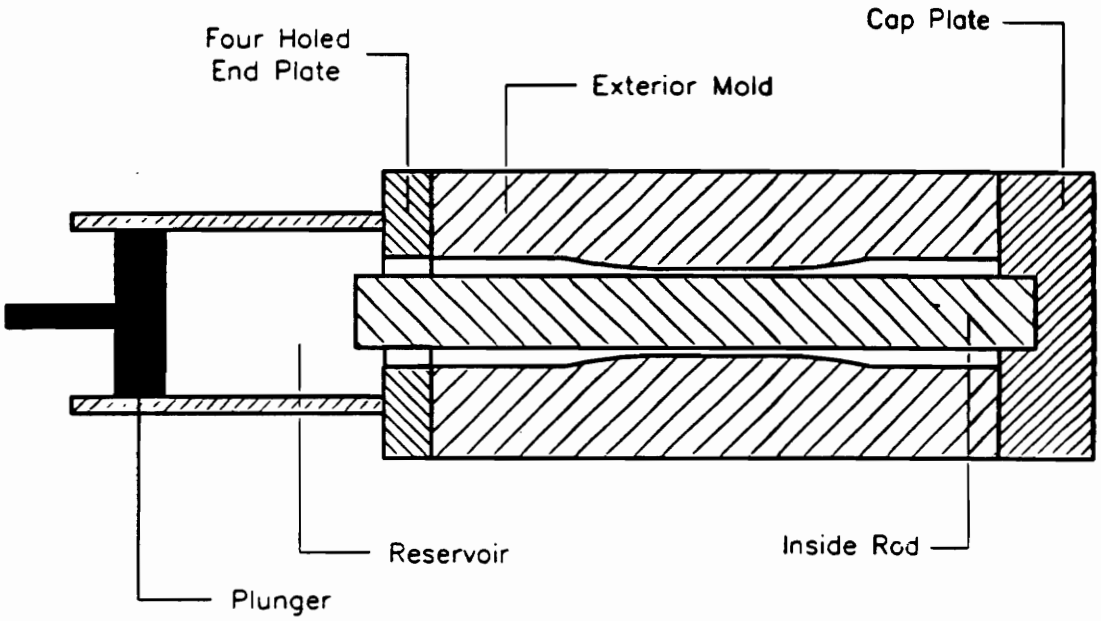

Figure 3.10 The Injection Molding Assembly.

molding compound and then pushed from the reservoir, through four symmetrically placed holes in the end plate, and into the mold. This end plate with four holes is very important to the fiber flow pattern and should be remembered when viewing the results of the NDE methods. The assembly is then cooled prior to removing the interior rod and exterior mold. The exterior mold is a continuous piece of graphite and must be machined in half for removal. The surface finish on the outside of the tube is very good and no additional machining is required in the gage section or transition regions. The inside rod is also made of graphite and must be removed by machining. In some cases, a scale was left on the inside surface of the tube, and this scale will affect some of the NDE results as will be discussed later. The outside of the grip regions are then machined in order to obtain proper gripping tolerances. In retrospect, the outside machining of the grip areas is probably unnecessary.

In order to accurately reference the various parts of the tube, the tube is divided into five regions (Figure 3.11). The terms upstream and downstream are based on the flow direction of the molding compound and are required due to differences in the fiber distributions in the different regions. For example, the fiber distribution in the upstream transition region is significantly different than the distribution in the downstream transition region.

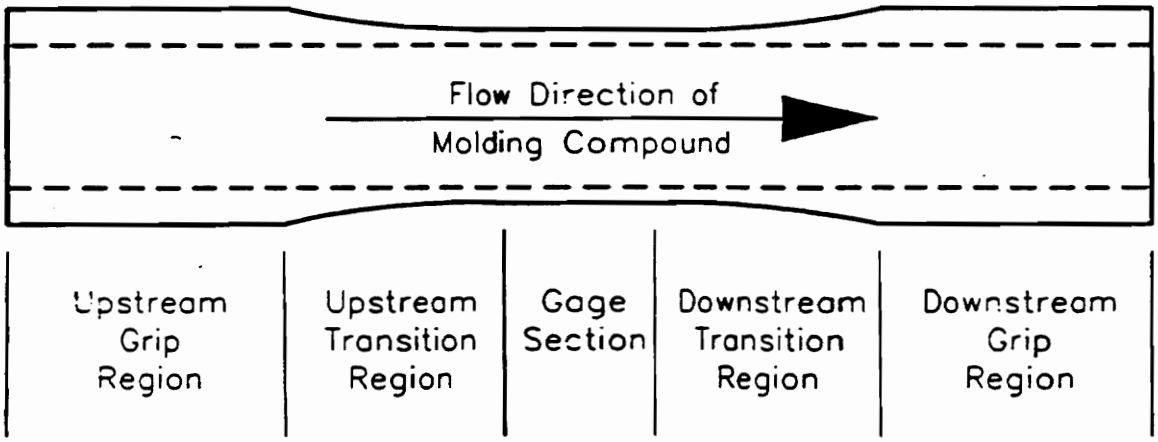

Figure 3.11 Regions of the Tube.

These differences have a major effect on the failure location in the specimen and are readily observed by some of the NDE methods.

Eight specimens were fabricated and were used throughout this investigation. The first specimen (118-89) was fabricated with 0.5 inch chopped graphite fibers. Figure 3.12 presents a photograph of Specimen 118-89 with strain gages attached and the end plugs removed. During fabrication, the specimen did not release cleanly from the mold, and several large chips were taken from the surface of the specimen. Examples of these types of chips are shown in Figure 3.13. Specimen 119-89 was fabricated with 0.38 inch fibers and also contained chips. Further investigation of the molding assembly indicated the chips were due to a poor surface finish in the transition regions of the graphite mold. The molds were then reworked, and the chip problem was nearly eliminated. All the subsequent specimens were fabricated with a 0.38 inch chopped graphite fiber. In addition to the chips in specimens 118-89 and 119-89, specimen 262-89 contained a small 1.0 inch axial stress crack extending from the downstream transition region and halfway into the gage section. Similarly, specimen 264-89 contained a 3.0 inch axial crack extending from the downstream transition region, through the gage section, and nearly along the entire length of the upstream transition region. These cracks are thought to be the

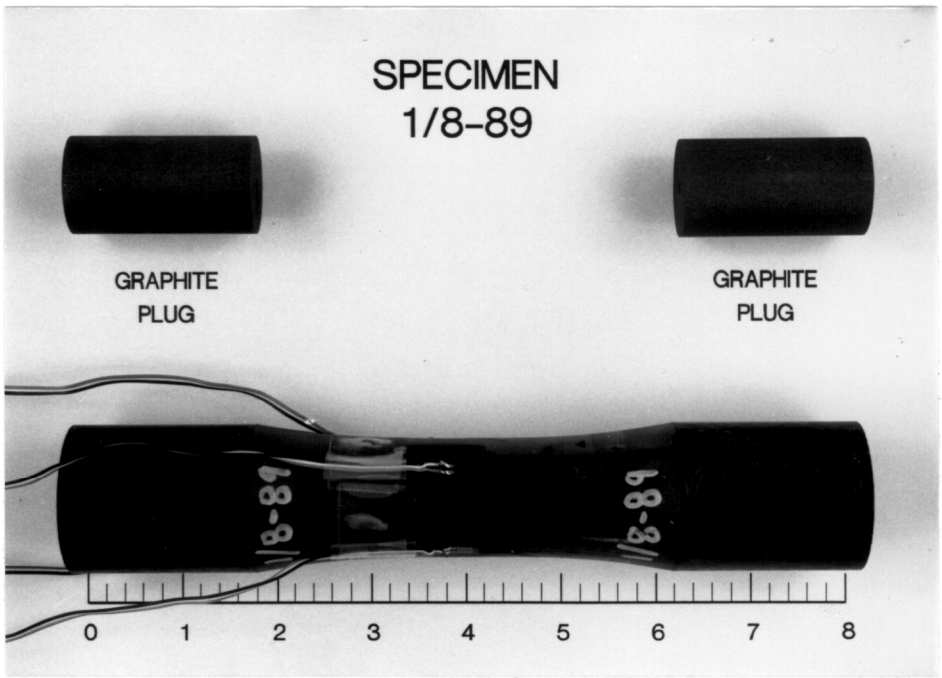

Figure 3.12 Specimen 118-89 with Strain Gages Attached and End Plugs Removed.

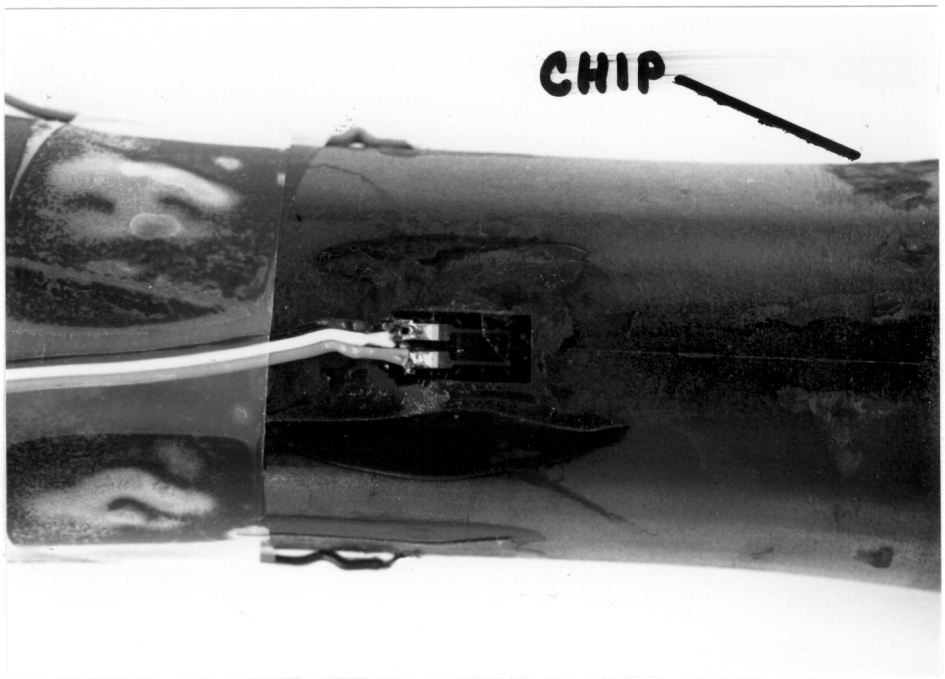

Figure 3.13 Surface Chips in Specimen 118-89.

result of final machining of the inside diameter. Specimens 258-89 through 261-89 did not have any visible defects on the surface. Physical property data for all of the test specimens are summarized in Table 3.5.

Table 3.5 Physical Property Data for the Specimens.

Composite Number	Glass Type	Fiber Type	Fiber Length (inch)	Volume Fiber (%)	Apparent Porosity (%) After ID Bore	Apparent Porosity (%) After Machining	Bulk Density (g/cc)	Comments
118-89	CGW 7070	HMU-PVA-3k	0.50	27		1.32	1.98	deliverable- surface damage in reduction region
119-89	CGW 7070	HMU-PVA-3k	0.37	27		0.31	2.03	deliverable- surface damage in reduction region
258-89	CGW 7070	HMU-PVA-3k	0.37	27	5.52	1.97	1.98	deliverable- no visible defects
259-89	CGW 7070	HMU-PVA-3k	0.37	27	2.58	2.48	1.98	deliverable- no visible defects
260-89	CGW 7070	HMU-PVA-3k	0.37	27	1.62	4.65	1.92	deliverable- no visible defects
261-89	CGW 7070	HMU-PVA-3k	0.37	27		1.95	1.95	deliverable- no visible defects
262-89	CGW 7070	HMU-PVA-3k	0.37	27		1.57	1.97	deliverable- 1" crack in gauge sect.
264-89	CGW 7070	HMU-PVA-3k	0.37	27		2.86	1.94	deliverable- 3" crack in gauge sect.

4.0 TEST FACILITY DEVELOPMENT

One of the main goals achieved in this program was the development, installation, and performance verification of a multiaxial test facility for ceramic composites. This type of facility combines the complexity of a biaxial test frame with the stringent alignment and stiffness requirements needed to successfully test ceramic materials. The development of the facility was a cooperative effort between the Materials Response Group at Virginia Tech, Instron Corporation, and United Technologies Research Center (UTRC). The result of this cooperative effort is a high stiffness test frame and advanced hydraulic grips with precision alignment capabilities. The entire test facility can be completely controlled with a digital computer, and by the end of 1990, the facility will be equipped with an Instron short furnace and capacitance extensometer for high temperature testing up to 1500°C in an oxidative environment.

4.1 The Test Frame

The test frame is a two post system rated for 100 kips axial and 50 kip-inches torsional loads (Figure 4.1). A high stiffness frame was required to reduce the amount of twist in the crosshead under rated loads. Twist tends to

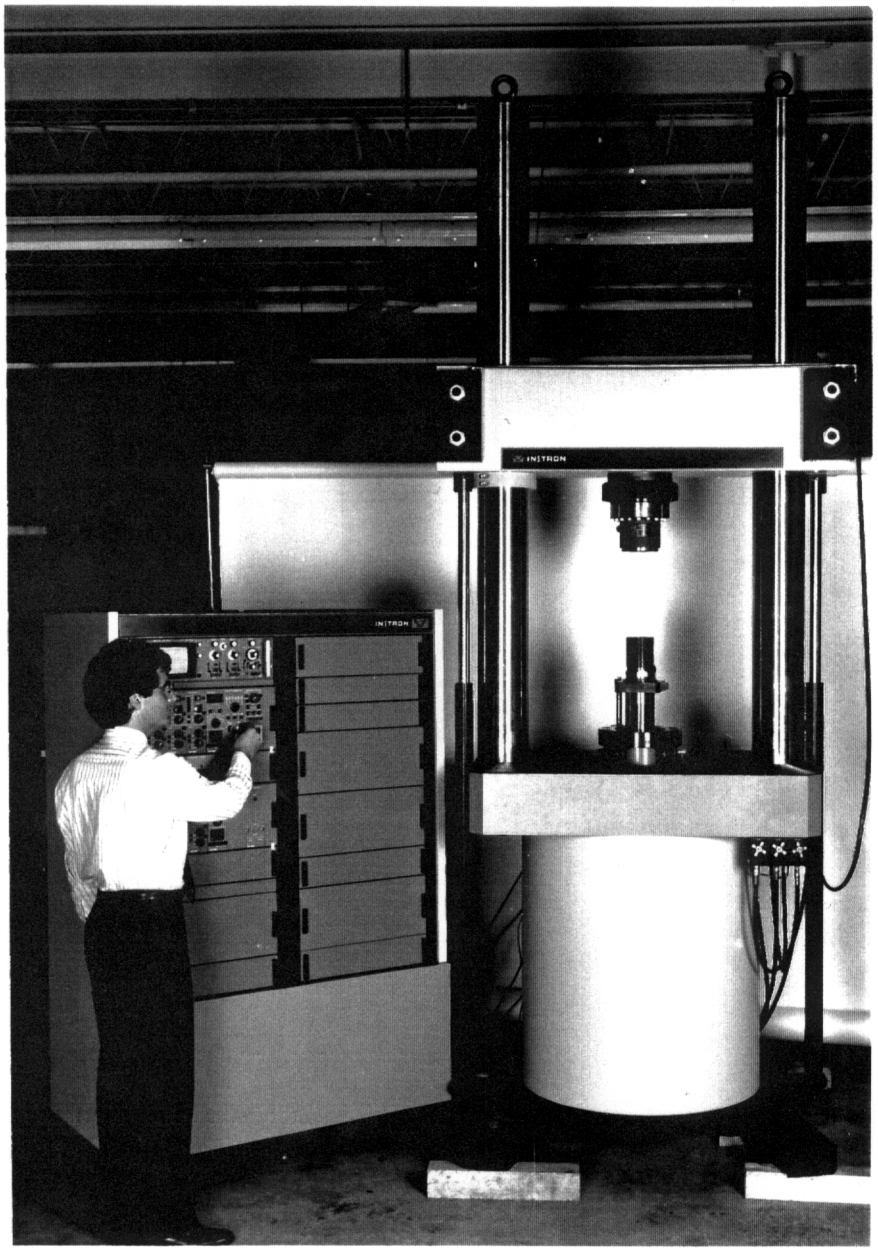

Figure 4.1 The Test Frame.

introduce a bending moment into the specimen under torsional loading, and even a slight amount of bending can be very detrimental to the performance of a ceramic composite. The stiffness of the frame is rated at 5.0×10^6 lbs/inch axial and 3.8×10^6 inch-lbs/deg torsional at 40 inches separation between crosshead and base. The load cell and actuators are rated at 50 kips axial and 25 kip-inches torsional. The actuators are top mounted to also reduce the amount of twist, and a hydraulic bearing for the actuator has been included to improve the alignment and compressive stability of the actuator piston.

4.2 The Hydraulic Grips

The major thrust of the cooperative effort was the development of the hydraulic grips. The grips contain a collet assembly designed to hold a 1.5 inch diameter cylinder 1.5 inches long. Figure 4.2 shows a sectional view of the grips without a specimen. When activated, the piston moves upward forcing the collet into the head assembly and thereby causing the collet to grip the specimen. The piston travel and, hence, the gripping load is limited by the aluminum spacer plate shown in Figure 4.2. The base of the grips are water cooled, and once the head is modified for cooling channels, the grips will be

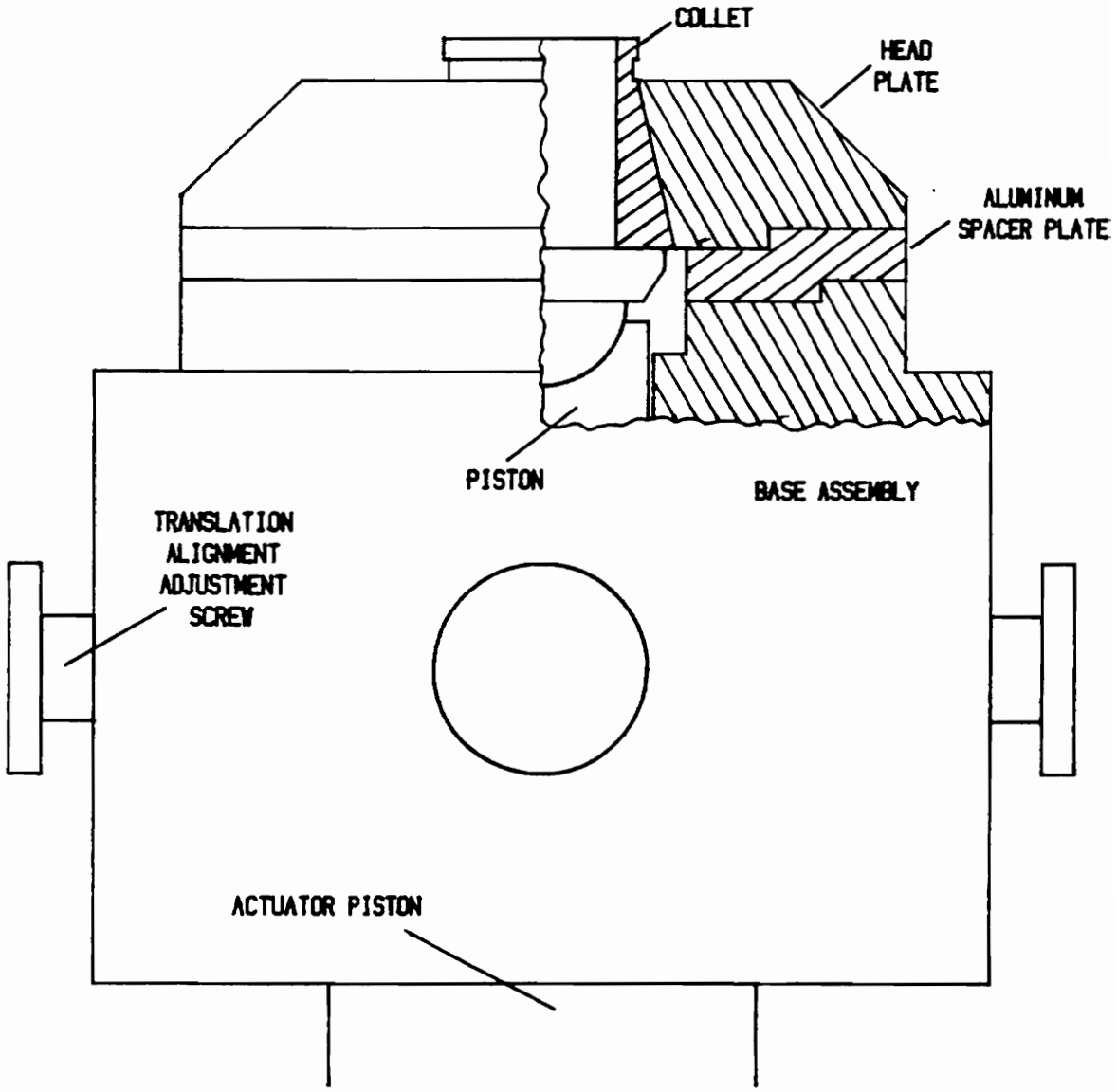

Figure 4.2 A Sectional View of the Hydraulic Grips.

able to operate in close proximity to the high temperature furnace.

The grips are also equipped with precision alignment capabilities. The X-axis translational alignment is controlled by adjusting the alignment screws shown in Figure 4.2. A similar set of adjustments controls the Y-axis alignment. The rotational alignment is controlled by the alignment screws located on the bottom of the grip. This set of adjustments permits the grips to be aligned about an axis out of the page. A similar set of adjustments controls the rotational alignment about the X-axis. With this combination of alignment controls, we can easily align the system and essentially eliminate all of the bending moments except those which are induced by the curvature of the specimen itself. As a result, the probability of premature failure due to specimen misalignment is greatly reduced.

4.3 Test System Control and Data Acquisition

In addition to the standard control console, the test facility is equipped with the Instron Intelligent Interface. The Intelligent Interface permits control of the test frame with a personal computer through an HP-IB bus, and Instron has a variety of software packages for system control. All of these packages are written in HP

Basic and, therefore, require the HP operating system. In our case, we equipped an HP Vectra ES12 (an MS-DOS machine) with an HP viper board which contains the HP operating system. This combination of an MS-DOS computer and an HP board provides a wide range of flexibility. All of the application programs can be run in an HP environment, and then the data transferred into a MS-DOS format for use with any of the MS-DOS programs such as LOTUS 1-2-3, Harvard Graphics, etc.

Two of the Instron Application Packages were used in this program. The first package is called the Proof-Test Package. This program is used to conduct quasi-static, uniaxial tensile tests. It combines test system control with data acquisition and data reduction to produce a very complete package. The major limitation with the program is its inability to control the torsional channel. Therefore, the package can not be used to run a pure torsion or a combined tension-torsion quasi-static test.

The second Instron Application Package used in this program was the Biaxial-Block Program. The package is configured to control the test frame for cyclic loading spectrums. In addition, the Biaxial Block Program also monitors the current status of the test on the computer screen. Figure 4.3 contains a printout of a sample status screen from a test conducted in this program.

STATUS

AXIS	LOOP	SEQNCE	BLOCK	EVENT	1/2 CYCLES	UNITS LOAD	UNITS POS'N	UNITS STRAIN
AXIAL	1	1	1	2	100047	KIP	ins	%
TORS'N	1	1	1	2	100047	KIPins	degrees	%

PEAKS

AXIS	LOAD MAX	LOAD MIN	POSITION MAX	POSITION MIN	STRAIN MAX	STRAIN MIN	CURRENT LOAD	CURRENT POS'N	CURRENT STRAIN
AXIAL	+2.5E+0	-5.0E-3	+1.1E-2	+5.9E-3	+5.3E-2	-2.3E-3	+2.5E+0	+1.1E-2	+5.2E-2
TORS'N	+1.9E-2	-1.5E-2	+5.0E-3	+1.2E-3	+0.0E+0	+0.0E+0	-1.1E-2	+2.5E-3	+0.0E+0

AE COUNTS: 25 LOAD/STROKE: +4.90E+2 LOAD/%STRAIN: +4.64E+1

Figure 4.3 A Sample Status Screen Printout.

The loading spectrum is divided into events, blocks, and sequences. An event is defined by the control modes (for example load and torque), the minimum and maximums for the waveforms, the type of waveforms (sine, square, triangular, etc), the cycling frequencies, the phase lag between the axial and the torsional channel, and the number of waveform repeats. A block consists of a collection of events, and a sequence is made up of a collection of blocks. Figure 4.4 diagrams a tensile waveform for three events, two blocks and one sequence. The first event (EV1) consists of two relatively slow, high loading cycles. The second event (EV2) consists of four medium loading cycles at a faster rate, and the third event consists of eight low loading cycles. The first block (BL1) consists of the events EV1-EV2-EV1, and the second block (BL2) consists of the events EV1-EV1-EV3-EV1-EV1. The two blocks are then combined in order to form a sequence. As can be imagined, events can be defined and linked to simulate almost any form of spectrum loading. Therefore, this control package can be a very important tool for any program involving performance simulation in a testing frame.

The main limitation of the Biaxial Block Program was its inability to collect and store data as opposed to simply monitor the data. One of the achievements in this program, was the upgrade of the Biaxial Block Program to overcome this limitation. Currently, the program can

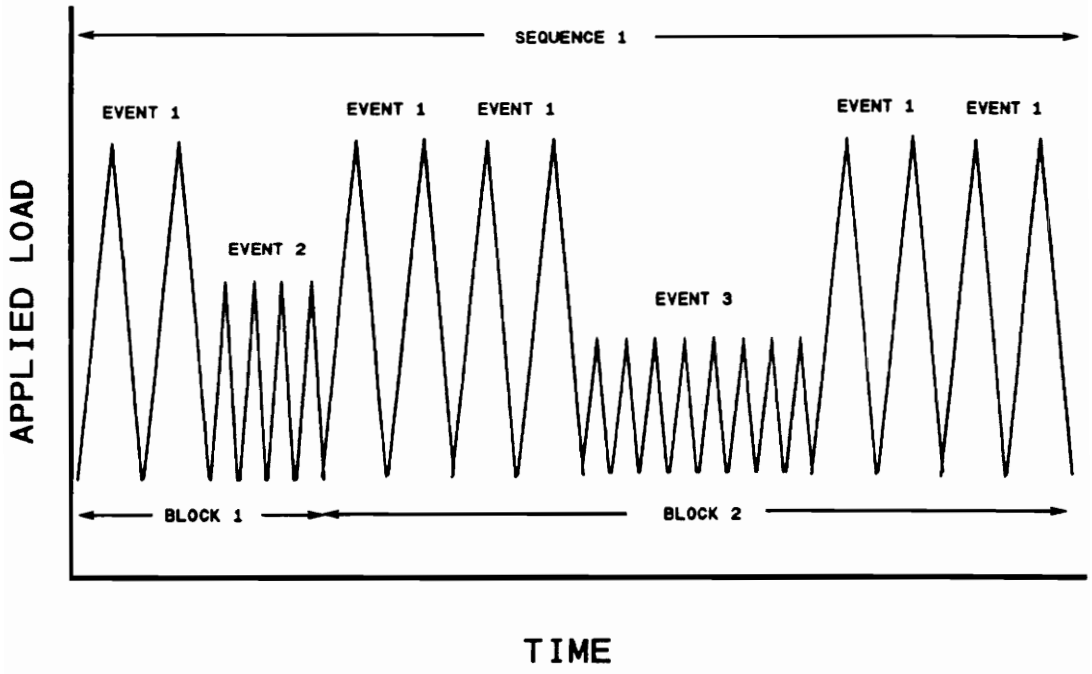

Figure 4.4 A Schematic Diagram of a Tensile waveform Containing Three Events, Two Blocks and One Sequence.

collect up to 9000 data points (1000 measurements on nine channels) and then store these data points on disk for post-processing. One of the data channels could be from an external source such as the Acoustic Emission counts from an AE system through an HP voltmeter. In addition to data collection, the computer also monitors stiffness in the form of Stroke/Load and Strain/load. Overall, the Instron Intelligent Interface and its supporting software provide a wide variety of flexibility and capabilities not available with the standard control console.

4.4 Test Facility Performance

The performance of the system was evaluated through a series of tests conducted at the Instron facility in Canton, Massachusetts and at the temporary installed site in Room 4 of Randolph Hall. A complete summary of the test facility specifications is contained in Appendix 1. In general, the performance of the test facility was excellent. The machine exhibited excellent control and very little "bumping" when switching control modes. In a cyclic load control mode, the machined operated very smoothly at 5 hz with little of no distortion of the response signal as compared to the input control signal. Although the system could operate at slightly higher frequencies, it could not reach a cyclic frequency of 10 Hz

without over-driving the input signal due to the 5 gpm hydraulic power supply and the flow rate of the servo-valves.

In load control, the system produced a very smooth loading curve for the quasi-static tensile tests. However, quasi-static tensile testing in stroke control proved to be inadequate. We found the controller could not provide a smooth ramp during a quasi-static test in stroke control due to the stiffness of the load train. For typical test frames, the stiffness of the load column is low enough to permit relatively large actuator strokes in comparison to the amount of strain induced in the specimen since most of the stroke is absorbed in the load train and not the specimen. For a high stiffness load frame, the compliance of the loading column is reduced, and therefore, more of the stroke is taken up by the specimen. As a result, very small actuator strokes induce relatively large strains in the specimen. In addition, these materials have very small strains to failure which compound the problem. One possible alternative to help this problem would be to replace the 5 gpm servovalves with 1 gpm valves. The lower flow rate servovalve would provide better control of the actuator. However, the lower flow rate servovalve would reduce the allowable cycling frequency from over 5 cycles/second to only 1 cycle/second, and for high cycle

fatigue tests, this reduction in cycling rate would be unacceptable.

A second problem developed during the cyclic test series when the specimen began to slip out of the top grip. Several attempts were made to clean the specimen and even slightly roughen the specimen surface in the grip region. Although these modifications appeared to reduce the problem, the specimen continued to slip out of the grips. After consulting with Instron, the head of the grip was disassembled, and the aluminum spacer plate removed. The thickness of the spacer plate was then reduced by 0.010 inches, and the grip reassembled. For the remainder of the testing program, no slippage was observed in the top grip. Apparently, this problem has been resolved.

The final area of concern with the test frame involved zero drift in the electronics, especially the axial load channel. Over the course of a cyclic test (some of which lasted over 4 days), the zero balance on the load channel drifted up to 5% of the 20% load range. The other channels also experienced some zero drift. The main cause of this drift was probably the inadequate temperature control in the temporary test facility. Once the facility is moved to its permanent location in Hancock Hall, the temperature variations will be minimal, and the problem may be resolved.

In spite of these minor problems, the facility performed very well. The alignment is excellent. The electronics are very smooth in load control. The cycling frequencies were acceptable for cyclic fatigue testing, and the computer control capabilities were easy to use. Although several problems will arise when the high temperature furnace is mounted, the test facility should prove to be a very capable and user-friendly system for the high temperature testing of CMC's.

5.0 TEST METHOD DEVELOPMENT

One of the main emphases of this program is the development and application of test methods for ceramic composite tubes subjected to uniaxial stresses. These test methods will lay the foundation for the development of test methods for multiaxial loadings. In general, the methods are based on relatively standard or established techniques developed for isotropic or polymeric composite materials. However, in most cases the techniques had to modified to accommodate the ceramic composite materials. Two of the largest areas of test method development have already been covered under test specimen design and test facility development. The remaining areas include nondestructive test methods and testing procedures. Section 5.1 summarizes an extensive report on the investigation of nondestructive test methods[50] prepared for Oak Ridge National Laboratories. These methods focus on the characterization of the state of material prior to, during, and after testing. Section 5.2 considers the destructive testing procedures such as test system control, strain measurement techniques, loading rates, data acquisition, etc.

5.1 Evaluation and Application of Nondestructive Examination Techniques

In order to fully understand and model the damage process in a ceramic composite component, the development of damage in the test specimens must be thoroughly characterized. This characterization includes the evaluation of the initial state of material, the identification of damage modes, the determination of the interaction between damage modes, and the identification of final state of material. In addition, an understanding of the progression from the initial state to the final state of the material is required.

The initial state of material consists of a wide variety of factors. Some of these factors include porosity distribution, fiber orientation and distribution, initial defects (large voids, microcracks, etc), residual stress states, and the quality of fiber/matrix bonding. As the specimen is tested under mechanical and/or thermal loading, the initial state of material will change and damage may develop. For example, the stiffness of a material may change during fatigue loading due to the development of matrix microcracks. Eventually, the specimen will fail, and the specimen must again be examined in order to determine the failure modes and the final state of material.

In order to monitor the various states of material and characterize the damage development process, some type of nondestructive evaluation (NDE) of the component must be performed. These NDE results are used to determine the critical defects which control the performance of the specimen. Currently, a wide variety of defects can be located and identified in a ceramic composite specimen. However, the effects of these defects on the damage development process and, hence, performance in a ceramic composite are virtually unknown. For example, failure of an unreinforced ceramic or glass can be governed by a small void or a crack of a few microns. However, polymeric composites can be insensitive to flaws on the order of a few millimeters.

The effect of defects on the response of ceramic composites is expected to fall somewhere between these two extremes. Some of the first information on the sensitivity of ceramic composites to initial defects was provided by Marshall and Evans[51]. They introduced controlled surface flaws into specimens by Vickers and Knoop indentations. Some of these flaws produced cracks and chipping which extended across more than 10 fibers. In all of their tests, the crack initiation stress level was not altered by the presence of the induced flaws, and in most cases, the first matrix cracks did not even initiate from the indentations.

Similar results were observed in this program. Specimen 118-89 contained several large surface chips produced in the manufacturing process, as shown in Figure 3.8. The largest chip was on the order of 0.25 inches in diameter and 0.015 inches deep. Nevertheless, the failure due to quasi-static tensile loading occurred in a region well removed from the defects. In addition, the failure load of specimen 118-89 which contained these large surface defects was nearly identical to the failure load of specimen 261-89 which contained no surface defects. Under cyclic loading, the specimen performance also did not appear to be affected by the surface defects. In addition, the one inch axial stress crack in the gage section of specimen 264-89 did not appear to influence the tensile performance of the specimen under cyclic loading. Conversely, the three inch initial crack in specimen 262-89 significantly lowered the performance of the specimen. All of these results will be discussed in detail in the following chapter. Based on the observed results, the performance of the CMC tubes is less sensitive to large surface chips and cracks than manufacturing defects in the transition region. However, as indicated by specimen 262-89, the performance is not completely insensitive to defects.

Initially, we could not identify the critical defects in the injection molded tubes. As a result, we undertook a

very broad based examination of NDE methods for ceramic composites. A list of the examined methods is shown in Table 5.1. Each of these methods was applied to specimen 118-89 to determine the applicability of the method to ceramic composite components. In some cases, the methods required modifications to handle the tubular configurations. Detailed descriptions of the applied methods and results of the investigations are contained in Reference 50.

In addition to the NDE techniques examined above, a form of thermography called SPATE (Stress Pattern Analysis of Thermographic Emissions) was investigated and used throughout the cyclic test matrix. SPATE is an in-situ test method which lends itself very well to monitoring damage development during cyclic testing[52]. In short, the SPATE system measures the cyclic variations in the thermal emissions in a specimen and correlates these emissions to the applied cyclic loads. For isotropic materials subjected to fully reversed loading, the measured emissions can be directly converted to stresses producing a full field stress pattern in the specimen. The damage development can then be directly monitored by changes in the stress field. In the case of non-isotropic materials, the conversion from thermal emissions to stresses in not straight-forward; and in the case of the injection molded specimens with large variations in fiber orientations, a

Table 5.1 Evaluated NDE Methods.

Acoustic Methods	X-Ray Methods
C-Scans	Film Radiography
Scanning Acoustic Microscopy	Computed Tomography
Acoustic Emissions	
Acousto-Ultrasonics	

Other Methods
Thermography
SPATE
Optical Microscopy
Scanning Electron Microscopy

direct transition from emissions to stresses is impossible. Nevertheless, the evolution of damage can still be monitored by changes in the calculated, albeit inaccurate, stress fields. Therefore, the method is still extremely valuable in the location of damage regions and monitoring how this damage develops until failure.

Overall, a wide variety of NDE methods were investigated in this program, and based on the results of this investigation, a combination of methods was used to characterize and monitor the state of material of a specimen throughout its life. Prior to testing, x-ray radiographs of each specimen were taken in order to determine the fiber orientations throughout the specimen. During quasi-static testing, acoustic emissions were monitored on specimen 118-89. Unfortunately, the testing program required that the final two quasi-static specimens be tested at the Instron facility in Canton, Massachusetts, and acoustic emission monitoring equipment was not available for these two tests. During cyclic testing, acoustic emissions were monitored and SPATE was applied. After testing, both optical and scanning electron microscopy were used to investigate the failure surfaces. In order to better correlate the damage state and its effect on the performance of the specimen, the actual NDE results for each of the test specimens are presented with the mechanical test results in the following chapter.

5.2 Test Procedure Development

Although ASTM has developed an excellent set of testing procedures for polymeric composites, the application of these procedures to ceramic composites is not always straight-forward due to the brittleness of the material and the eventual goal of high temperature characterization. In addition, ASTM has not established standardized procedures for multiaxial testing. Therefore, as part of this research program, we examined a wide variety of procedures. In this section, we will investigate the areas of gripping, quasi-static test procedures, and cyclic test procedures. For the quasi-static and cyclic procedures, we will discuss extensometry, control modes, and data acquisition. In addition, we will make several comments concerning the effectiveness of the in-situ NDE methods examined above.

5.2.1 Gripping and Alignment.

As described in Chapter 4, the hydraulic grips were specially designed by Instron for this program, and Instron provided detailed instructions on specimen insertion. These instructions are fairly complex, and should be followed rigorously. Overall, once the spacer plate in the top grip was ground down 0.010 inches, the grips worked extremely well. While operating the grips, special care

must be taken not force or even slightly push the specimen into the grips. The specimen must be able to slide freely into the grip before clamping. If the specimen requires pushing it into the grips, it will be extremely difficult to remove, and may even require disassembly of the grip for removal the specimen.

The major question with the Instron procedure concerns the 3000 psi recommended grip pressure. In this program, we used grip pressures from 1500 psi for the low stress cyclic test up to 3000 psi for monotonic tensile tests. None of the specimens exhibited grip damage in the form of crushing. Although the 3000 psi grip pressure seems very high, recall the grips are deflection limited due to the spacer plate. As a result, we do not know how much load has actually been transmitted to hold the specimen. Tolerances in the grip regions of the specimens will also significantly affect the actual grip load applied to the specimen. Since the grips are deflection limited, a specimen with a grip diameter of 1.495 inches may have a significantly lower grip load than a specimen with a 1.499 inch grip diameter. This area of actual applied grip loads and grip tolerances should be more thoroughly investigated to prevent specimen slippage or unnecessarily crushing a weak specimen.

The last area of concern associated with specimen gripping involves the alignment verification. For this program, we aligned the system at installation, and then did not check the alignment throughout the remainder of the program (approximately 2 months). In retrospect, the alignment should have been checked at least once during the course of the program, and we may even consider adding an alignment check as part of the standard test procedure similar to calibration verifications of the extensometer. ASTM Procedure E1012-89 "Standard Practice for Verification of Specimen Alignment under Tensile Loading"[53], contains an excellent description of alignment procedures for flat tensile loaded specimens and would require only minor modifications for developing a procedure for both tensile and torsional alignment verification with tubular specimens.

5.2.2 Quasi-static Testing Procedures.

The quasi-static test series consisted of three tension tests conducted at the Instron facility in Canton, Massachusetts. All three tests used the Instron capacitance extensometer for strain measurements. The first test was performed using the Instron "Proof-Test" package for data acquisition and control. Data were also recorded on an X-Y recorder. This test was run in load

control, and acoustic emissions were monitored throughout the test. The second and third tests were controlled from the console and were run in stroke control at two different stroke rates. No acoustic emissions were recorded for these tests, and data were recorded with an X-Y recorder.

The capacitance extensometer performed very well for all of the tests. The extensometer mounted very easily, and showed no signs of slippage during the test. In addition, the extensometer exerts very small bending loads on the specimen. This extensometer is also capable of testing in elevated temperatures up to 1600°C. Unfortunately, this extensometer is a single axis unit and will require significant modifications in order to measure both axial elongation and angular twist. In addition, the extensometer comes with a stand-alone control module which does not provide the wide set of ranges as compared to the standard control console.

The first test was conducted in load control with a loading rate of 20 lbs/sec (0.8% full scale per sec) and produced a very smooth loading curve up to failure. Unfortunately, a load controlled test does not show the "graceful" failure beyond the ultimate stress for a ceramic composite when compared to a sintered ceramic. Therefore, the remaining two tests were conducted in stroke control. The second test was conducted at 0.00002 in/sec (0.02% full scale per sec). This extremely low rate as compared to the

full scale produced a rough loading curve due to noise or chatter in the control mechanism. The third test was conducted at 0.00005 in/sec (0.05% full scale per sec). Although the loading curve was smoother than that of the second test, it still contained a fairly large amount of noise. Based on the results of these tests, we highly recommend testing all of the specimens in a load control mode. The test facility simply does not have the capability to conduct quasi-static stroke controlled tests which generate smooth loading curves.

The Instron Proof-Test package used for the first test provided excellent test system control, data acquisition, and data reduction capability. The program also stores the data in an HP format. Therefore, with a little bit of work, we can translate the stored HP-ASCII data into an MS-DOS format for use in a spreadsheet such as LOTUS 1-2-3. This data reduction capability is extremely valuable in generating high quality reports and papers for publication. Unfortunately, the Proof-Test package is limited to axial loadings only, and Instron is not planning to expand the program to biaxial loadings in the near future. One approach for multiaxial testing would be to control the test from the console and record the data with a stand-alone data acquisition system (DAS). This approach is very straight-forward, and the Materials Response Group already has the DAS equipment. Regardless of the computer

system that is used for data acquisition and/or control, we highly recommend using a standard X-Y recorder to generate a hard-copy back-up of the test data.

For the first quasi-static test, we mounted a single acoustic emissions transducer on the specimen and recorded AE counts as a function of load. Although, the system occasionally recorded an electronic blip, the system produced very valuable information with a small amount of set-up time or expertise. As a result, we recommend considering AE monitoring for all quasi-static testing, whenever possible.

5.2.3 Cyclic Testing Procedures.

All of the cyclic testing was conducted at Virginia Tech, and as a result, we had more control and knowledge of the actual testing procedures than with the quasi-static test series conducted at the Instron facility. In all of the tests, we used an MTS extensometer with a 1.000 inch gage length to measure strains, and all of the tests were conducted in load control with the Instron Biaxial Block program controlling the test facility.

Throughout the first several tests, extensometry was a major concern. Initially, the extensometer was attached with small rubber bands, and the knife edges were placed directly on the specimen. Since the knife edges are flat

and the specimen is tubular, the actual contact length of the knife edges on the specimen was very small, causing the extensometer to "walk" slightly during testing. As a result, we added a small bead of adhesive along the knife edges in addition to the rubber bands. This small amount of adhesive proved very effective in preventing the walking and avoided machining very complex tabs. Eventually, we plan to switch to the capacitance extensometer for all of the room and high temperature, uniaxial cyclic testing. Therefore, this extensometry question will need to be addressed again.

As stated previously, the Biaxial Block program was used to control the facility for all of the tests, and in some cases, the biaxial block program was also used to record stress-strain data. Two problems arose with the data acquisition end of the Biaxial Block program. First, the system could not record data at the cycling frequency of 5.0 Hz. Therefore, we slowed the cycling frequency to 0.1 cycles per second to record two cyclic stress strain curves with 50 data points each. The second problem we encountered involved data storage while running a test. Due to the storage limitations of the program, we had to store the data after every 1000 data points which required completely stopping the test, storing the data, and then restarting the test. As a result, the test was constantly being interrupted.

For the final two tests, we used the Biaxial Block program simply for test frame control and a stand-alone system for data acquisition. With the Biaxial Block program, we ran the first cycle at 0.1 cycles per second in order to guarantee we captured the initial stress-strain response. Then, the Biaxial Block program was set to cycle at 5.0 Hz until failure or runout without interruptions. The data acquisition system recorded the initial stress-strain response as if it was a quasi-static test and then recorded cyclic data (40 points on two channels for one cyclic stress-strain loop at 5.0 Hz) whenever required. In addition, once the storage buffers were filled with data, we did not have to interrupt the test to store the data. Overall, this combination of the Biaxial Block program and a stand-alone data acquisition system provided the most effective means of test control and data collection. The block program provides all of its capability such as spectrum loading, phasing, and stiffness monitoring. The stand-alone data acquisition system can record data without interrupting the test.

The final area of cyclic test procedures involves the application of NDE methods. Two in-situ methods were considered during the cyclic testing, AE monitoring and SPATE. AE monitoring was plagued with problems throughout the entire cyclic test series. First, interfacing the AE system with the Biaxial Block program was difficult.

Secondly and most importantly, the rate of AE count accumulation due to damage development in the specimen was very slow. As a result, the occasional electronic blip described in the quasi-static test procedures produced a significant number of erroneous AE counts which completely masked the real AE counts. Therefore, AE monitoring during cyclic tests with the system used is this program in not recommended.

Although SPATE worked very well for some of the high cycle fatigue specimens, the SPATE system had limitations in monitoring the damage development for the low cycle fatigue specimens and in the early stages of life in the high cycle fatigue specimens. For a relatively large area on the surface of specimen, SPATE requires approximately 20 minutes (6000 cycles at 5.0 Hz) in order to generate a scan with acceptable resolution. Typically, for highly loaded specimens or early in the specimen's life, the specimen is cycled at the specified load level for a predetermined number of cycles, and then the load level is significantly reduced in order to perform the SPATE scan. This lower cyclic stress is selected such that specimen is not additionally damaged while the SPATE scan is taken. Unfortunately, for this material, the specimen had to be cycled at approximately 60% of the UTS in order to generate a signal strong enough to be read by the SPATE, and this load level was high enough to potentially further damage

the specimen and cloud the cyclic test results. Therefore, the SPATE could not effectively be used for specimens with very short lives or early in the life of a specimen where damage was accumulating at a fairly high rate. Nevertheless, for high cycle fatigue specimens which show very little damage development over the scanning time, the SPATE system worked very well and should be considered.

5.2.4 Recommended Procedures.

Overall, the gripping and alignment verification procedures are straight forward and fairly well established. The major remaining question concerns the gripping pressure for the specimens. One approach to characterize the gripping pressure is to first map slippage loads for a steel rod as a function of grip pressure and diameter. For example, we could machine a steel rod to 1.500 inches diameter in the grip region and then insert the rod into the grips using a 1500 psi grip pressure. We then put the machine into load control and increase the load until the specimen slips out of the grip. This will give us one data point. This procedure is repeated for grip pressures up to 3000 psi in order to generate a curve relating grip pressure to slippage load for a steel tube with a 1.500 inch diameter. We then machine 0.002 inches off of the grip diameter and generate another curve. Eventually, we will have a

well-defined relationship between grip pressure, grip diameter, and maximum load for a steel rod. For other materials, we can use the same relationships as for the steel by shifting the curves up or down based on the relative coefficient of friction and the bulk modulus for the new material as compared to steel. As a result, we will be able develop a real specification for the required tolerances in the grip region of specimen, and we will avoid unnecessarily crushing the specimen in the grips or having the specimen slip out of the grips in the middle of a test.

In the area of monotonic testing procedures, the limitations of the test facility dictate testing in load control. For biaxial quasi-static testing, we recommend controlling the test from the console and using a stand-alone data acquisition system to record axial load, axial strain, axial stroke, torque, angular twist and rotation. In addition, if AE is monitored, the AE counts can also be recorded by the data acquisition system. For axial loading the capacitance extensometer should provide excellent performance even at high temperatures. However, for biaxial loading, extensometry is still an area which needs to be addressed.

For cyclic testing, we recommend controlling the test with the biaxial-block program developed by Instron and monitoring the data with a stand-alone data acquisition

system. For biaxial tests where we need to monitor all six channels, a high speed data acquisition is required and the data acquisition program developed for the cyclic tests performed in this program needs to be modified. As with the monotonic tests, high temperature biaxial extensometry is a major concern and should be further investigated.

6.0 EXPERIMENTAL TEST RESULTS

Two types of CMC specimens were tested in this program. The majority of the experimental program consisted of room temperature, quasi-static and cyclic tests conducted on the tubular specimens. Detailed results of this portion of the experimental program are presented in Section 6.1. At the conclusion of these tests, rectangular tensile bars were machined from the grips regions of two tubes and then pulled in tension in an attempt to determine the transverse strength of the material. The results of the bar tests are described in Section 6.2.

6.1 Experimental Results for the Tubular Test Specimens

In order to investigate the performance of the ceramic composite tubes, we developed a detailed room temperature test plan in an attempt to maximize the amount of information with the limited number of available test specimens. This test plan consisted of a combination of NDE, mechanical testing, and post-test fractography of the specimens. Each of these areas is discussed in this chapter. Section 6.1.1 presents the NDE results prior to testing. Sections 6.1.2 and 6.1.3 present the mechanical

and in-situ NDE test results for the quasi-static and cyclic test series respectively. Section 6.1.4 contains the post-test inspections and fractography results. Throughout these sections, we discuss observed critical defects and postulate failure modes for the ceramic composite tubes.

6.1.1 NDE Inspection Prior to Testing.

As discussed in Section 5.1, we undertook a very intensive evaluation of NDE methods as applied to the composite tubes. As a result of this investigation, two methods, X-ray radiography and ultrasonic C-scans, were selected to nondestructively interrogate the tubes. Radiographs of Specimens 118-89, 260-89 and 264-89 are shown in Figures 6.1 through 6.3. These radiographs are typical of the radiography results for all of the tubes. The radiographs were taken by placing the x-ray film along the inside circumference of the specimen. The length of the film was one inch shorter than the eight inch tube length. As a result, the outside half inch of the grip regions do not appear in the radiograph. The width of the radiograph corresponds to 0-360° around the circumference.

Evaluation of Figures 6.1 through 6.3 clearly shows the injection molding process produces highly variable fiber orientations throughout the tubular specimens. In the

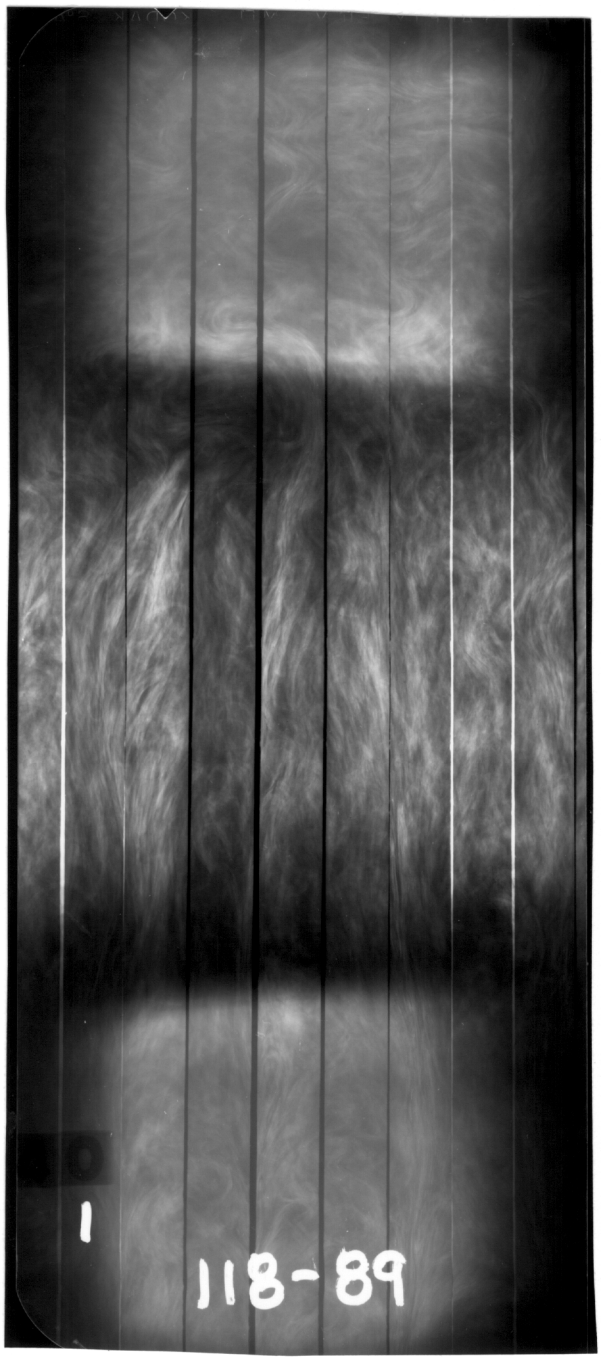

Figure 6.1 Radiograph of Specimen 118-89.

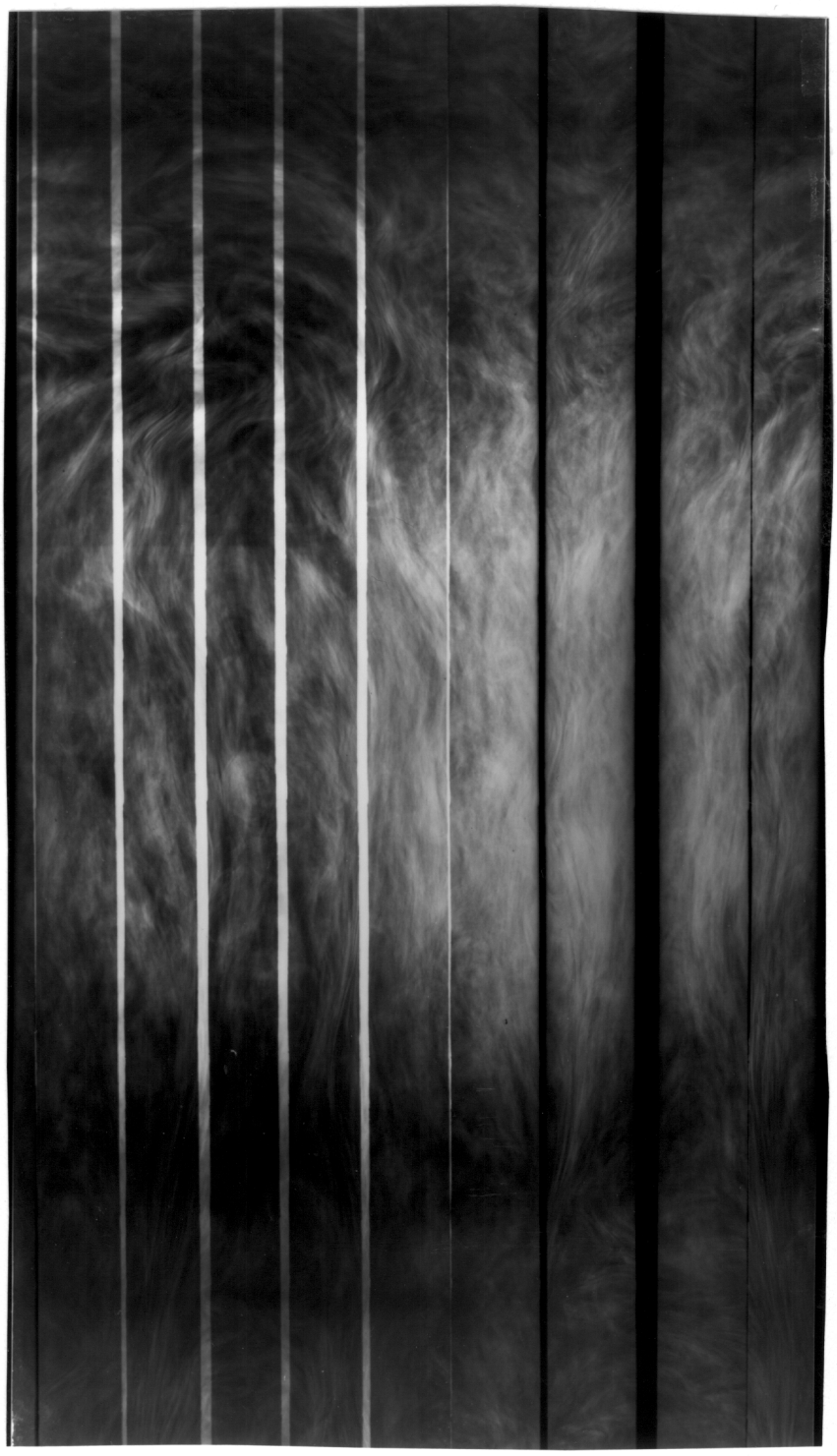

Figure 6.2 Radiograph of Specimen 260-89.

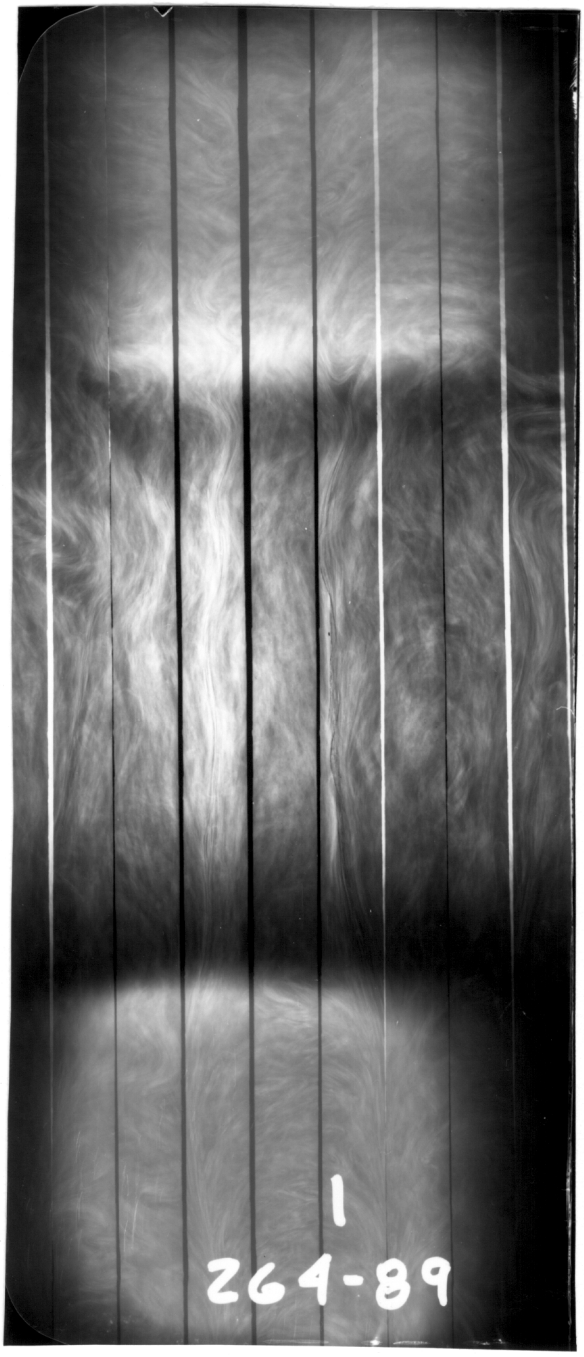

Figure 6.3 Radiograph of Specimen 264-89.

upstream grip regions located at the bottom of the figures, we can see four areas of axially aligned fiber flow regions (termed knit lines). These regions are the result of the four holes in the end plate of the molding apparatus. In some cases, the knit lines extend through the gage section and tend to cusp over in the downstream transition region. In Specimens 262-89 and 264-89, the knit lines even produced axial cracks in the specimens. The location of a crack in Specimen 264-89 is highlighted in Figure 6.3.

In addition to the knit lines, a large amount of in-plane fiber swirling is evident in the downstream transition regions of the tubes. Similar fiber swirling was observed in all of the tubes tested in this program. Radial cross-sections of the tubes also indicate a significant amount of out-of-plane fiber swirling in the downstream transition region. An example of this out-of-plane swirling is shown in Figure 6.4. In retrospect, the combination of in-plane and out-of-plane fiber swirling was the dominate, performance limiting defect in every specimen except 264-89 which contained the 3.0 inch axial crack along a knit line. Unfortunately, none of the NDE methods we investigated provided an indication of the out-of-plane swirling. As a result, one of the critical defects, out-of-plane fiber swirling, was not detected prior to testing.

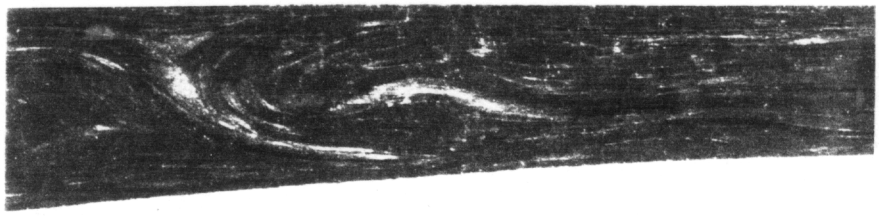

Figure 6.4 Out-of-plane Fiber Swirling.

C-scans were also performed on several specimens. Due to the nature of ultrasonic C-scans, curved surfaces with normals at large angles to the incident wave direction disperse the ultrasonic signals, and these curved regions can not be imaged. As a result, the C-scans of the tubes are limited to the gage length and only part of the transition regions. Figure 6.5 presents the C-scan results for Specimen 261-89. This C-scan image is typical of all of the C-scan results. The light regions in Figure 6.5 are the result of attenuation of the ultrasonic signal due to property variations. Comparison of the C-scan and the radiograph for specimen 261-89 (Figure 6.2) indicates the light regions match with the knit lines. Therefore, these knit lines probably have some type of material variations as compared to the remainder of the specimen, such as different fiber volumes, different porosity, or even large amounts of microcracking. Although these property variations appear significant in the C-scan images, the mechanical test results indicate the variations were not critical defects in these specimens under axial loading, and therefore, they were not investigated in more detail.

6.1.2 Quasi-static Testing Procedures and Results.

Specimens 118-89, 119-89, and 261-89 were tested at room temperature under quasi-static tension until failure.

Figure 6.5 C-scan Results for Specimen 261-89.

Specimen 118-89 was tested in load control at 1000 lbs/min, Specimens 119-89 and 261-89 were tested in stroke control at 0.00002 and 0.00005 in/sec respectively. Stress-strain results for the three tests are shown in Figure 6.6. The strains where measured with an 1.0 inch extensometer, and the stress calculations were based on the cross-sectional area of the gage length. Unfortunately, all three specimens failed in the downstream transition region. Therefore, the peak stresses shown on the stress-strain curves do not correspond to the failure stress of the material since the transition regions have different cross-sectional areas than those of the gage section. In addition, variations in the fiber orientations around the circumference and along the length of the tubes produce non-uniform stress distributions throughout the specimens. Therefore, the presented stresses should simply be considered as nominal stresses in the gage section.

During testing of specimen 118-89 an acoustic emission (AE) transducer was mounted on the specimen, and cumulative AE counts versus load were recorded. The load levels were then converted to nominal stress levels based on the cross-sectional area of the gage section to determine cumulative AE counts as a function of stress (Figure 6.7). Figure 6.8 presents the normalized secant modulus as a function of AE counts for Specimen 118-189. In this case, the secant modulus is defined as the slope of the line

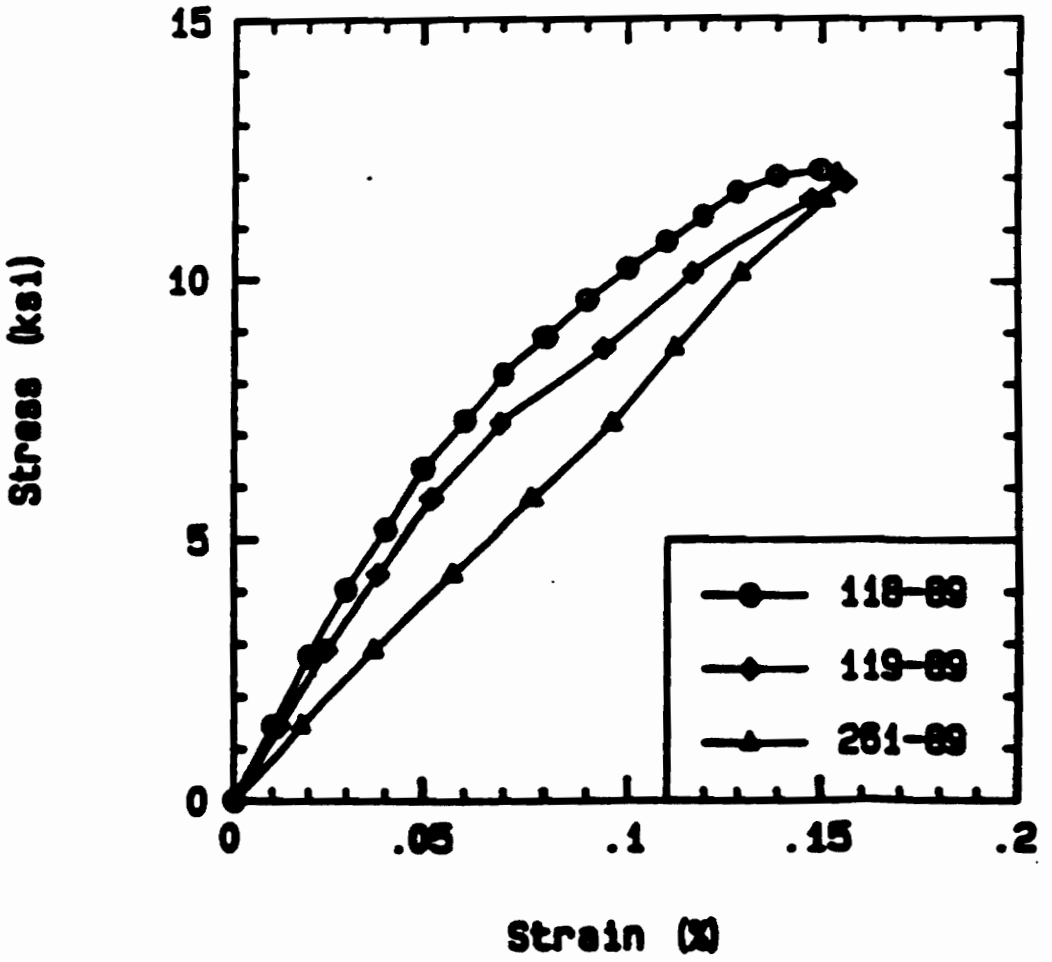

Figure 6.6 Stress-Strain Responses for the Quasi-static Specimens.

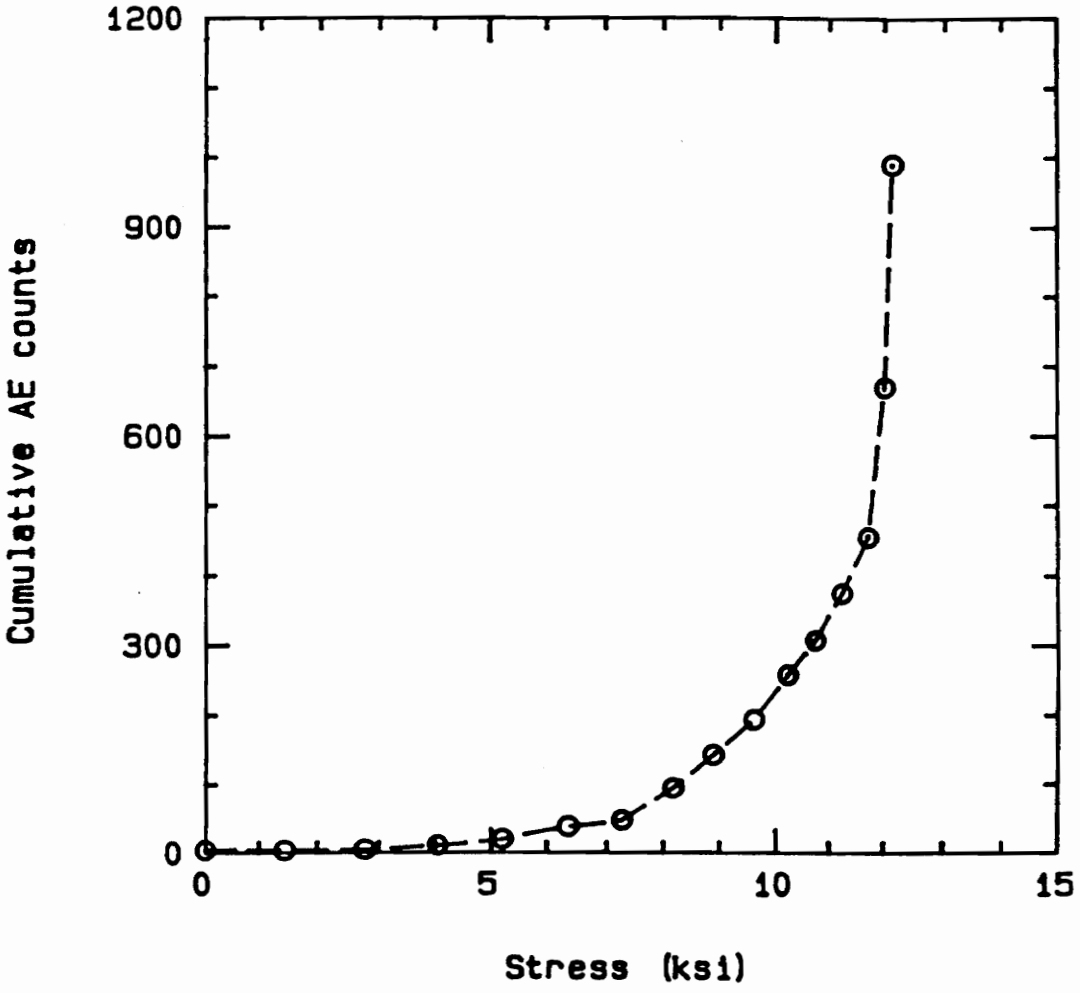

Figure 6.7 Cumulative AE Counts as a Function of Applied Stress.

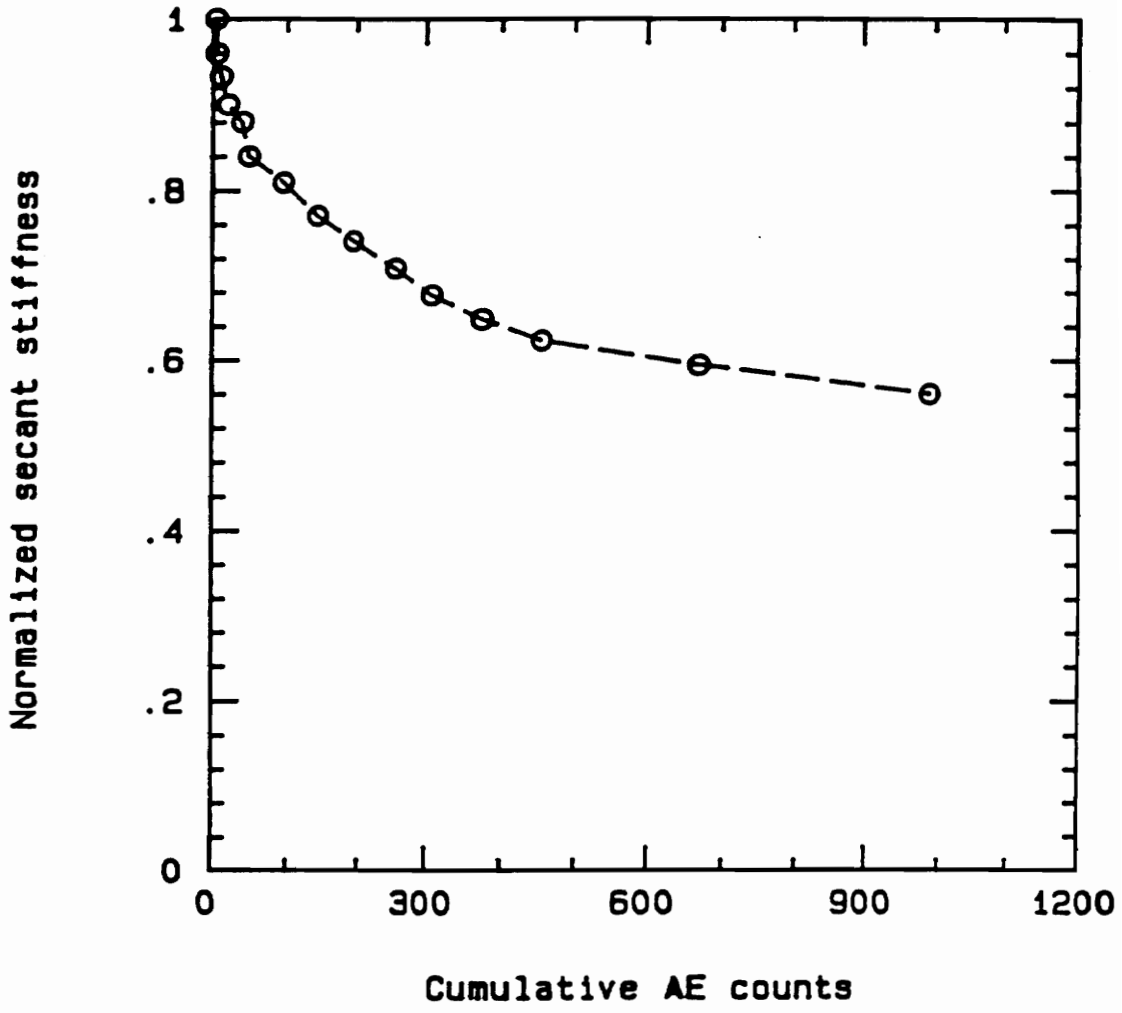

Figure 6.8 Normalized Secant Modulus as a Function of AE Counts.

connecting the origin and the point on the stress-strain curve corresponding to the AE count. This secant modulus is then divided by the tangent modulus at the origin of the stress-strain curve to produce a normalized secant modulus.

Evaluation of Figures 6.7 and 6.8 shows damage, indicated by the acoustic emissions, begins at relatively low stresses and continues to grow at a small rate until a stress of approximately 7.0 ksi. Although the AE counts appears relatively small at 7.0 ksi compared to the total AE counts at failure, the stiffness of the specimen has dropped 20%. Above a stress of 7.0 ksi, the number of acoustic emissions begins to increase exponentially indicating the amount of damage is growing very rapidly. Conversely, the rate of stiffness degradation as a function of AE counts is decreasing.

As with any AE method, monitoring the emissions is relatively simple. However, determining the source of the emission is extremely difficult. In this case, the transition at a stress level of 7.0 ksi may indicate the failure mode of the specimen is changing. At low stress levels, the acoustic emissions may correspond to matrix failures as a result of axial loading and residual thermal stresses. This type of failure would predominantly occur along the knit lines in the gage section where there are regions of highly axially aligned fibers and the smallest cross-sectional area. A small amount of this type of

damage in the gage section would be expected to generate large stiffness reductions. At higher stress levels, the acoustic emissions may correspond to matrix or shear failure in the swirled fiber regions where the fibers are oriented transversely to the axial direction. Since the swirled regions are outside the gage length, damage in these areas would not greatly affect the stiffness measured across the gage length. The large increase in AE counts for stress levels above 12.0 ksi probably indicates the failed locations throughout the swirled fiber regions are linking together leading towards eventual failure.

6.1.3 Cyclic Testing Procedures and Results.

Five tubes were tested under tension-tension (R=.1) cyclic loading at room temperature. The tubes were cycled at 5 Hz, and a 1.0 inch extensometer was attached to the gage section of tube. Periodically, the cycling rate was slowed to 0.05 Hz in order to capture the cyclic stress-strain response and to monitor the stiffness change as a function of life. Loading conditions, fatigue lives, and residual strengths for each specimen are summarized in Table 6.1. In this case, a runout is defined as one million cycles without a failure. After a runout, the specimen was pulled in quasi-static tension in order to determine its residual strength. As in the quasi-static

Table 6.1 Cyclic Test Results.

Specimen	Maximum Cyclic Stress (Ksi)	R	Cycles to Failure	Residual Strength
260-89	7.3 - 60% UTS	0.1	Run Out	10.9 Ksi
259-89	8.5 - 70% UTS	0.1	Run Out	12.4 Ksi
258-89	10.3 - 85% UTS	0.1	Run Out	14.7 Ksi
262-89	11.6 - 95% UTS	0.1	600 Cycles	----
264-89*	10.3 - 85% UTS	0.1	385 Cycles	----

* Specimen 264-89 contained a 3.0 inch longitudinal crack extending from the gage section into the downstream transition region.

test series, all of the specimens failed in the downstream transition region. Therefore, the above stresses or strengths should again be considered as nominal gage section values as opposed to actual cyclic stresses or strengths at the point of failure.

Evaluation of the fatigue data indicates two extremely interesting results. First of all, The material is very insensitive to fatigue loading as evidenced by the run outs when cycled at very high percentages of the UTS. Even Specimen 264-89 which contained a 3.0 inch crack extending into the downstream transition region survived over 300 cycles at 85% of the UTS.

Throughout all of the cyclic tests, stiffness changes were monitored in order to indicate damage development. Figure 6.9 presents the stiffness change as a function of cycles for Specimen 258-89 which was cycled at 85% of UTS for one million cycles. Notice the stiffness of the specimen across the gage length is essentially constant throughout the duration of the tests. Therefore, the amount of damage in the gage section of the specimen is probably minimal as a result of the cyclic loading. Notice this conclusion is limited to the gage section of the specimen since stiffness monitoring gives virtually no information of the damage development outside of the gage length. These results are typical of the stiffness change results for Specimens 259-89 and 260-89. Unfortunately,

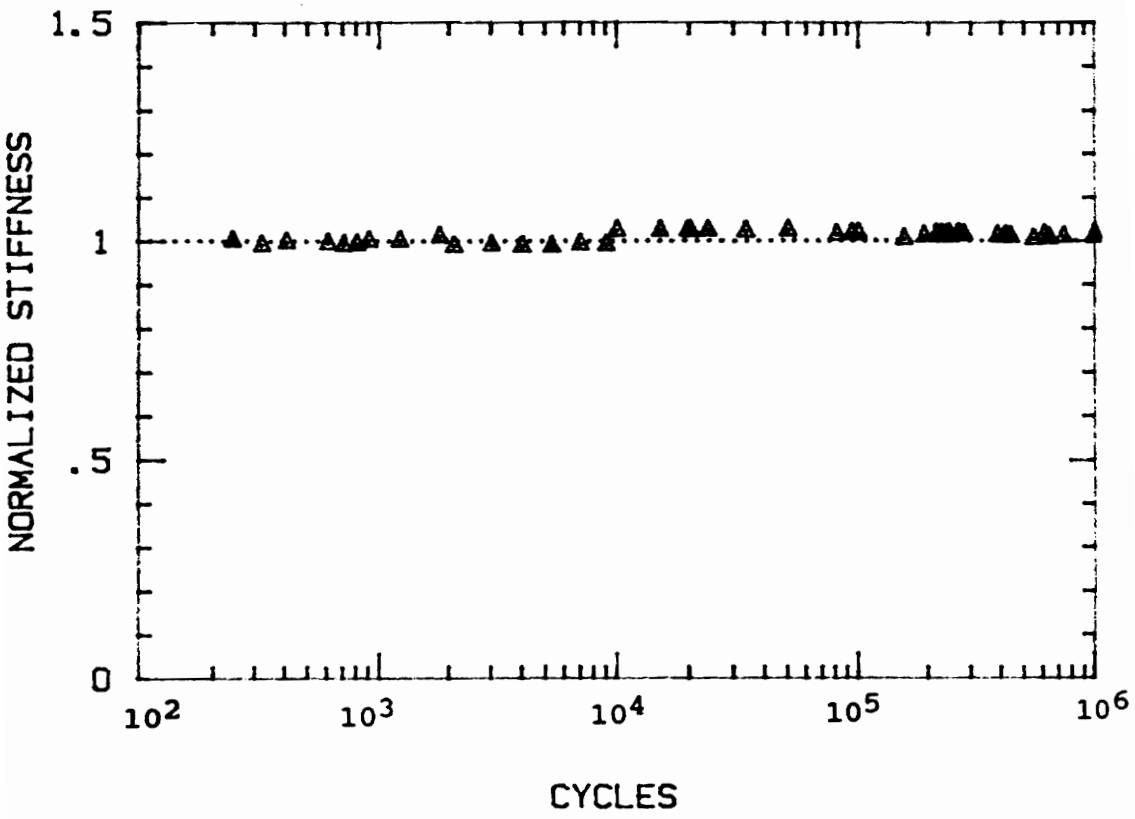

Figure 6.9 Stiffness Change as a Function of Cycles for Specimen 258-89.

the fatigue lives of the other two specimens were too short to collect sufficient data to produce any meaningful stiffness change results.

In order to monitor the damage development in the downstream transition region which is outside the gage length, we monitored the thermal emissions by means of the SPATE system described in Chapter 5. As noted in Chapter 5, a change in the thermal emission pattern is an indication of a change in the stress state in the specimen. Figure 6.10 presents SPATE images for the same region of Specimen 258-85 at four stages in the load history. The appearance of the last image is slightly different because we doubled the imaging time in order to generate a finer image.

The areas labeled "A" and "B" in the first image are of primary importance. First, we want to follow the damage progression in the area marked "A". In this region, we can see a linear discontinuity in the thermal emissions pattern which probably indicates a crack. Notice, as the number of cycles increases, the crack appears to grow and begins to link up with other cracks outside the imaging window. In the region "B", we can see a more pronounced nucleation and crack development throughout the load history. At 20,000 cycles, the crack at "B" is virtually nonexistent; but at 1,000,000 cycles, a crack has developed and is linking up with another crack growing in from the upper left.

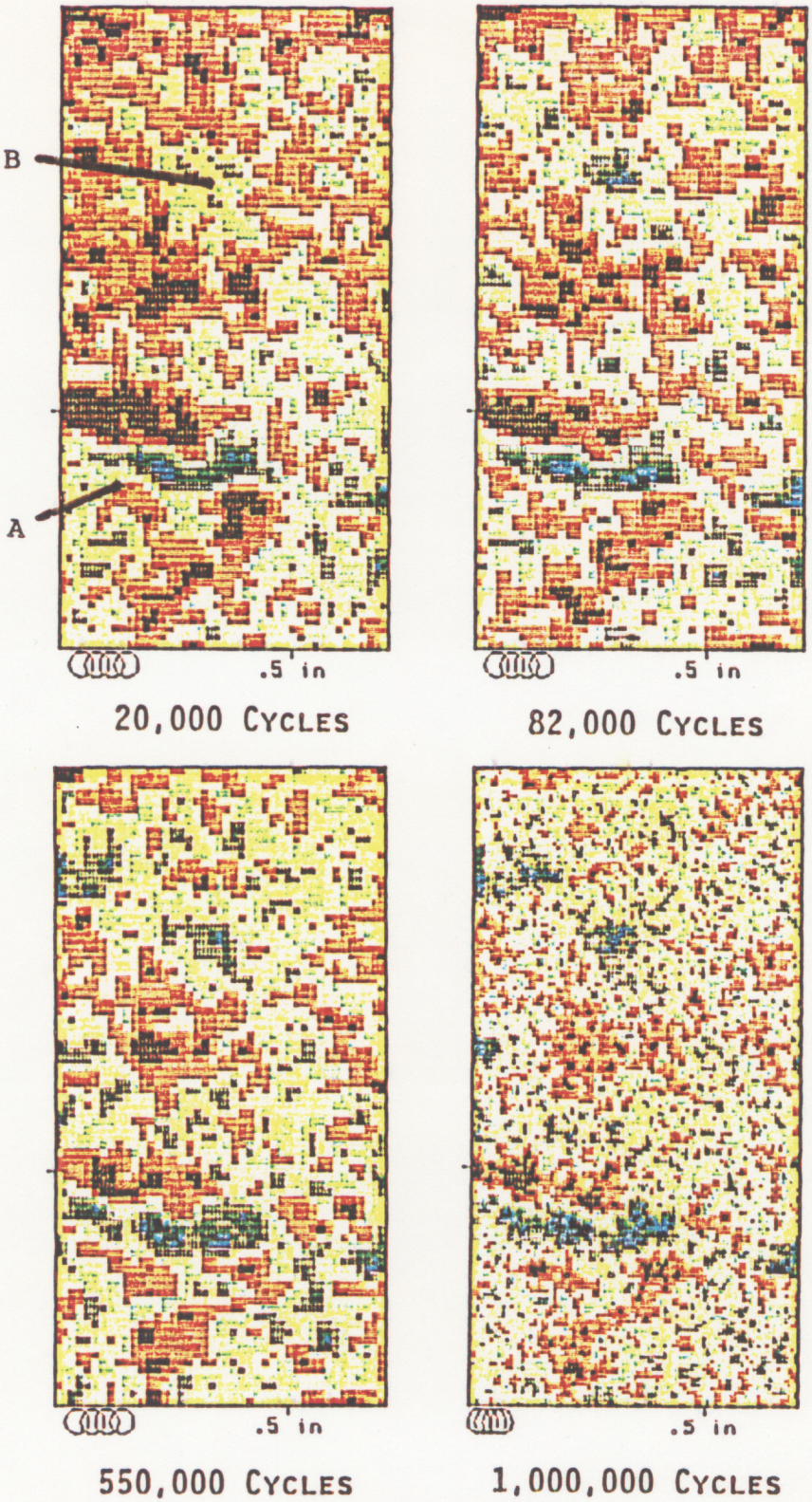

Figure 6.10 Spate Images for Specimen 258-89.

After one million cycles, the specimens were removed from the test frame and inspected with a dye penetrant. The penetrant confirms the existence of fatigue cracks in all of the specimens after one million cycles (Figure 6.11). The locations "A" and "B" from the SPATE images are shown on Specimen 258-89 in Figure 6.11. These results confirm the location of the cracks first observed with the SPATE system. Notice, the fatigue cracks in Specimen 258-89 are closer to the gage section than the cracks in Specimen 260-89. Correlation of the failure surfaces after the residual strength tests and the penetrant inspections, indicate the failure surfaces for Specimens 258-89 and 259-89 went through the observed cracks. The failure surface for Specimen 260-89 only partially followed the observed cracks indicating the fatigue cracks developed under cyclic loads at 60% of UTS were not as critical.

6.1.4 Residual Tensile Strength Results.

After the completion of the dye penetrant inspections the specimens were then pulled in quasi-static tension for residual strength. Figure 6.12 presents the results of the residual strength tests compared to the quasi-static tensile results on the uncycled specimens. Not only is the residual strength of Specimen 258-89 (cycled at 85% of UTS) high than the other two residual strengths, this specimen

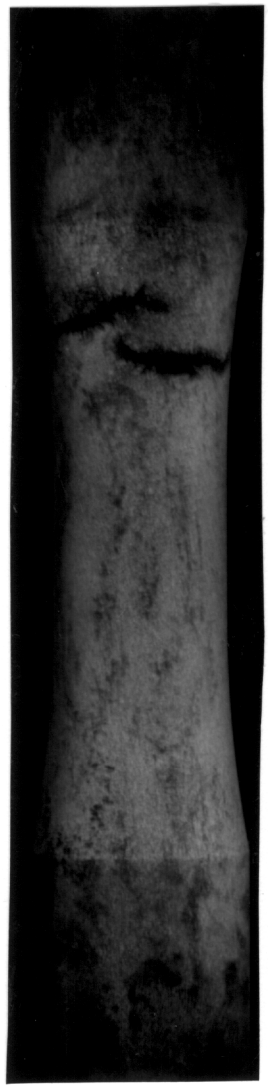

Figure 6.11 Dye Penetrant Inspection Results for Specimen 258-89.

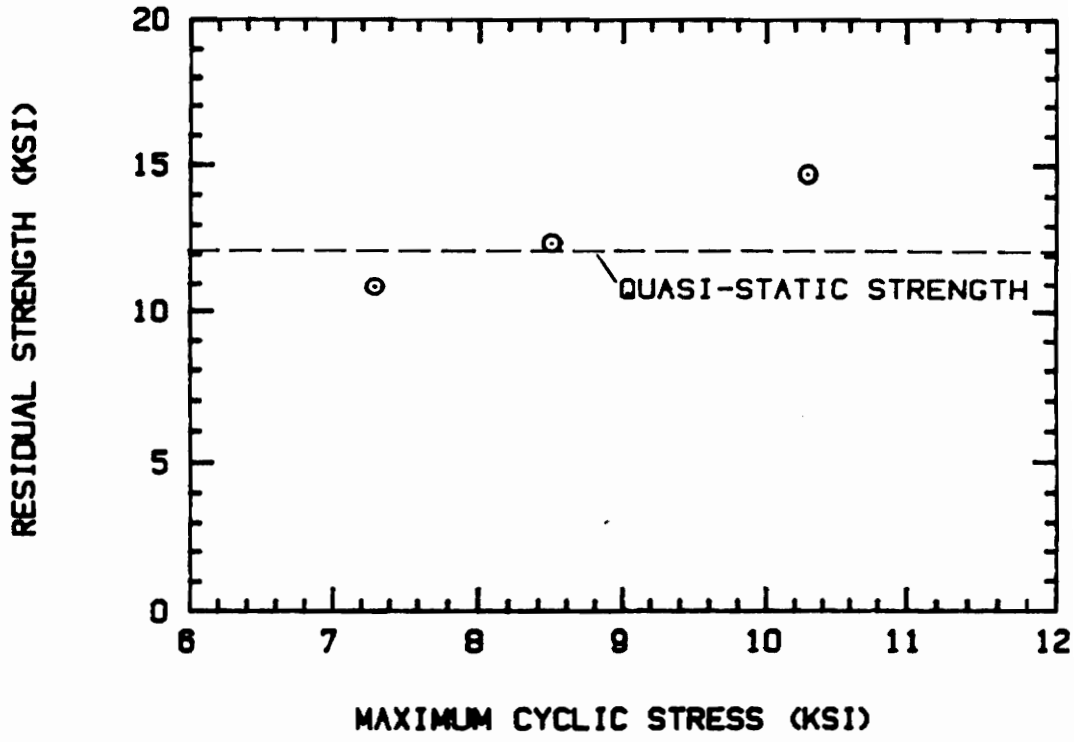

Figure 6.12 Residual Strength Results After One Million Cycles.

exhibited a residual strength 21% greater than the quasi-static strength. Clearly, some type of wear-in phenomenon has occurred.

6.1.5 Post-test Evaluation of the Specimens.

The post-test evaluation of the specimens consist of a fractography investigation of the failed surfaces and radiography of the failed specimens. Figure 6.13 presents a radiograph of a failed half of Specimen 118-89 which failed under a monotonically increasing tensile load. Evaluation of this figure shows the failure surface closely follows the fiber swirling in the downstream transition region. Similar results were observed in all of the quasi-static specimens. Therefore, in-plane fiber swirling should be considered a critical defect for these tubes.

The majority of the post-test evaluation focused on the fractographic analysis of the failure surfaces. Figures 6.14 through 6.16 present photographs of failed specimens. The downstream grip end of Specimen 261-89 has been removed for the bar tests described in the next section. Recall, Specimen 261-89 was loaded in quasi-static tension. Specimen 260-89 was cycled at 65% of the UTS for one million cycles and then pulled in quasi-static tension, and Specimen 258-89 was cycled at 85% of UTS for one million cycles and then pulled in quasi-static tension. Visual

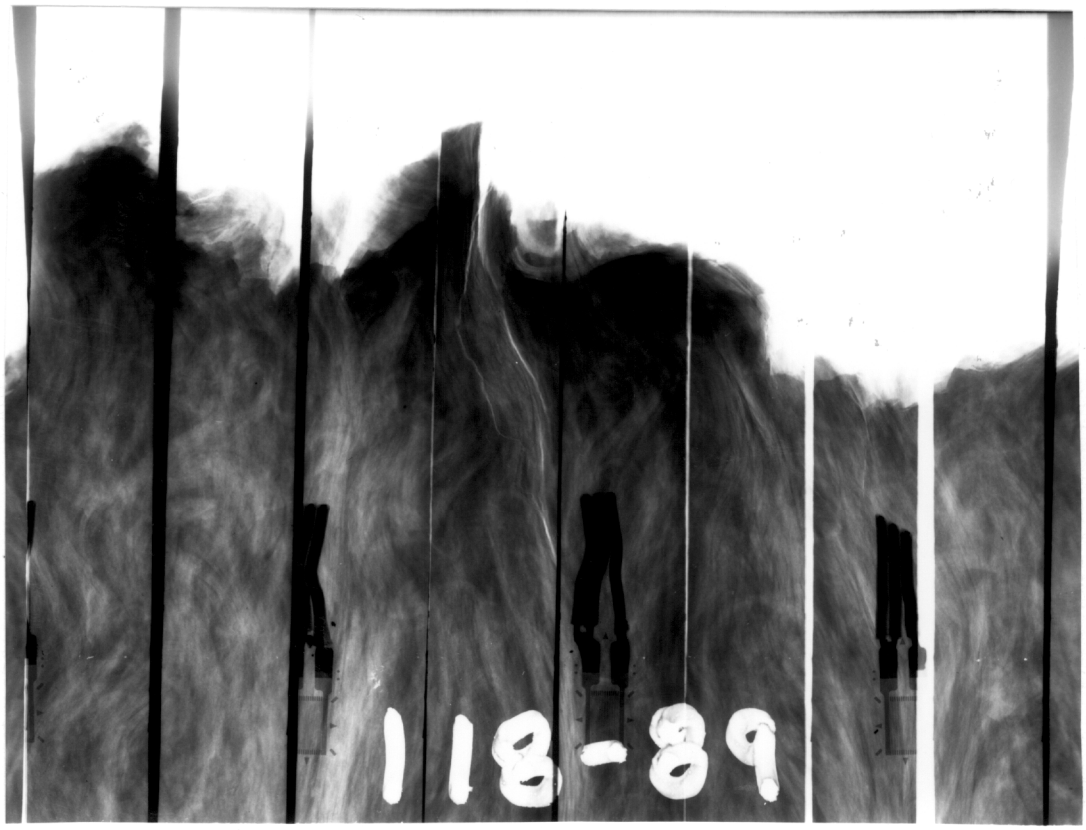

Figure 6.13 Radiograph of Upstream Failure Region of Specimen 118-89.

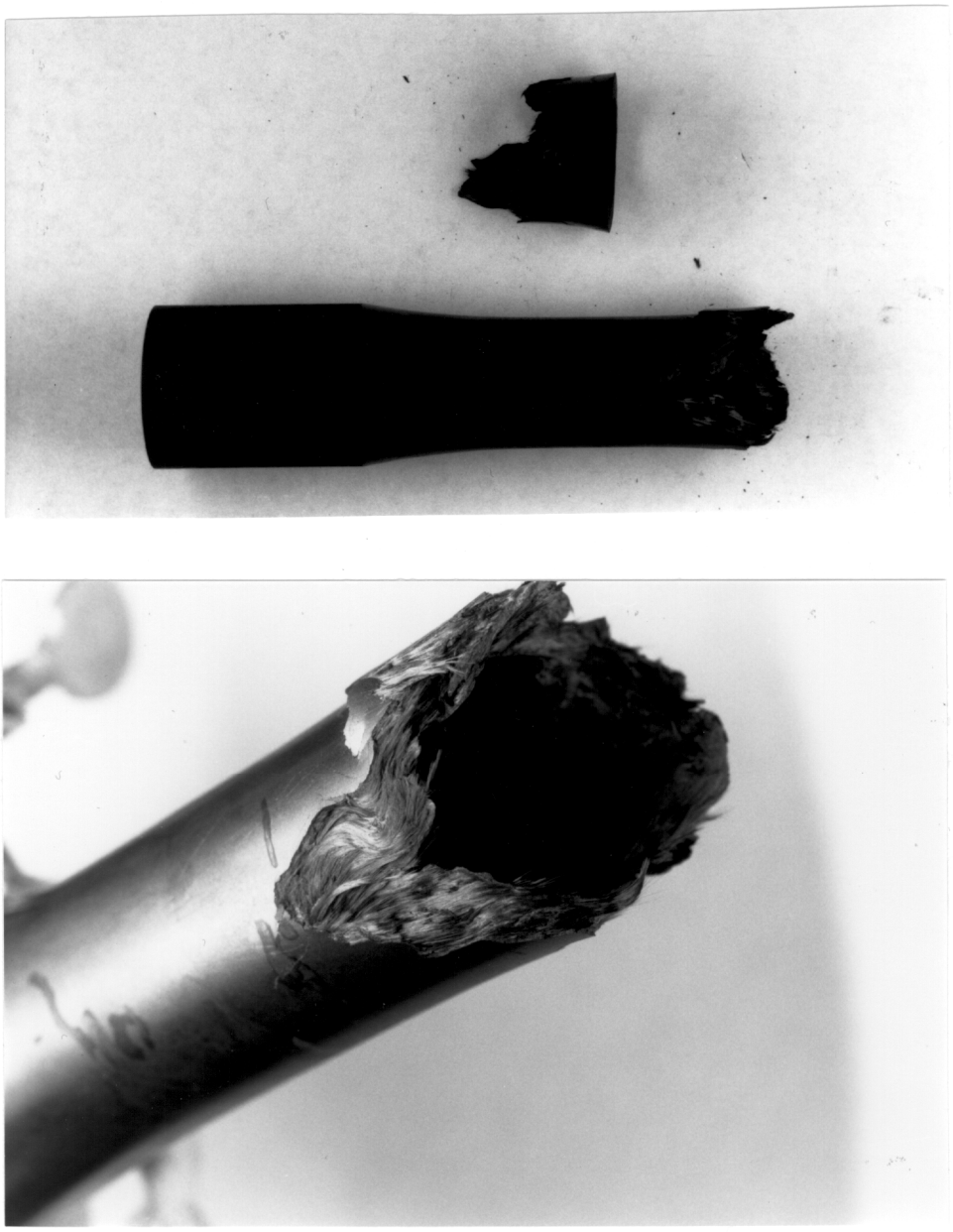

Figure 6.14 Specimen 261-89 After Failure.

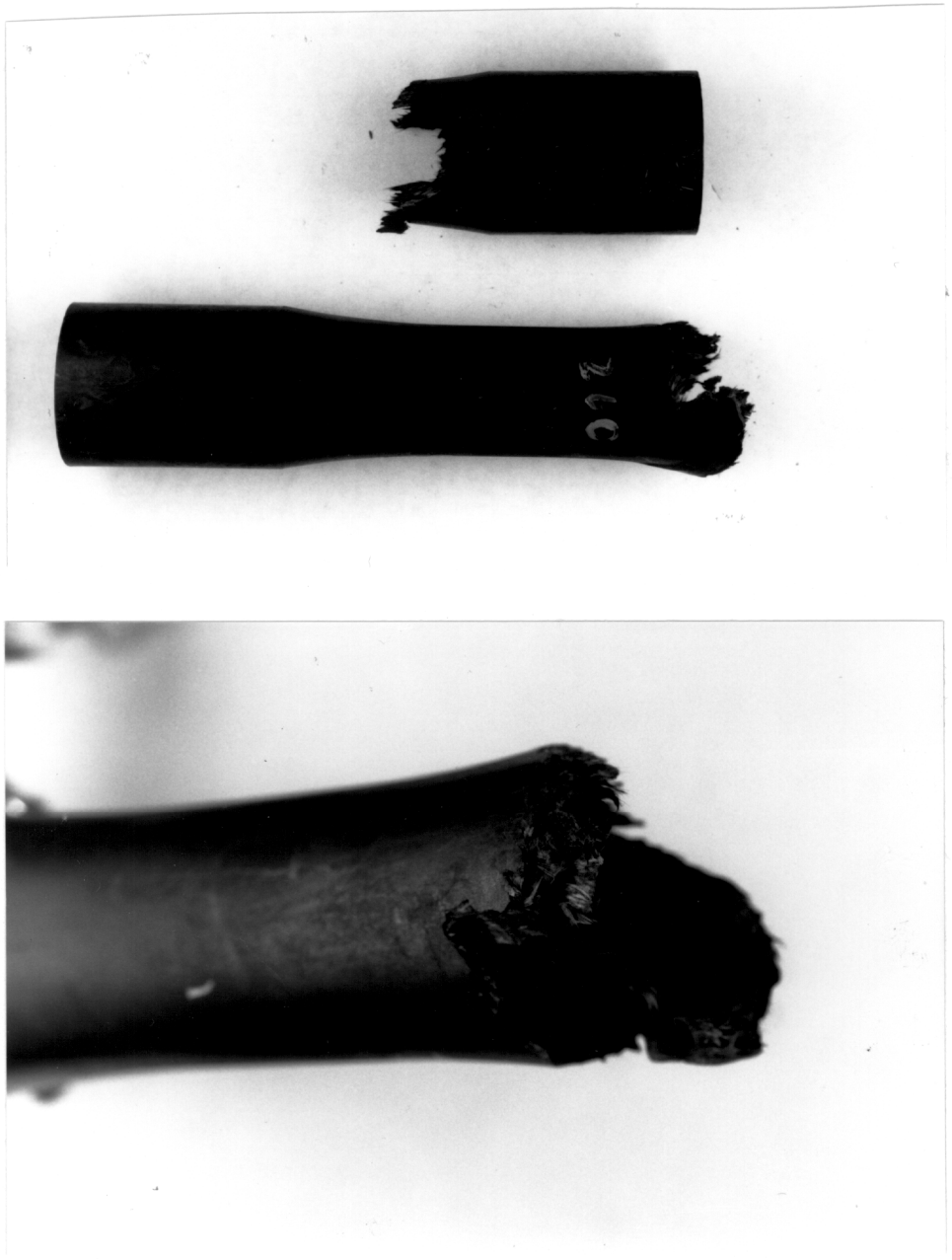

Figure 6.15 Specimen 260-89 After Failure.

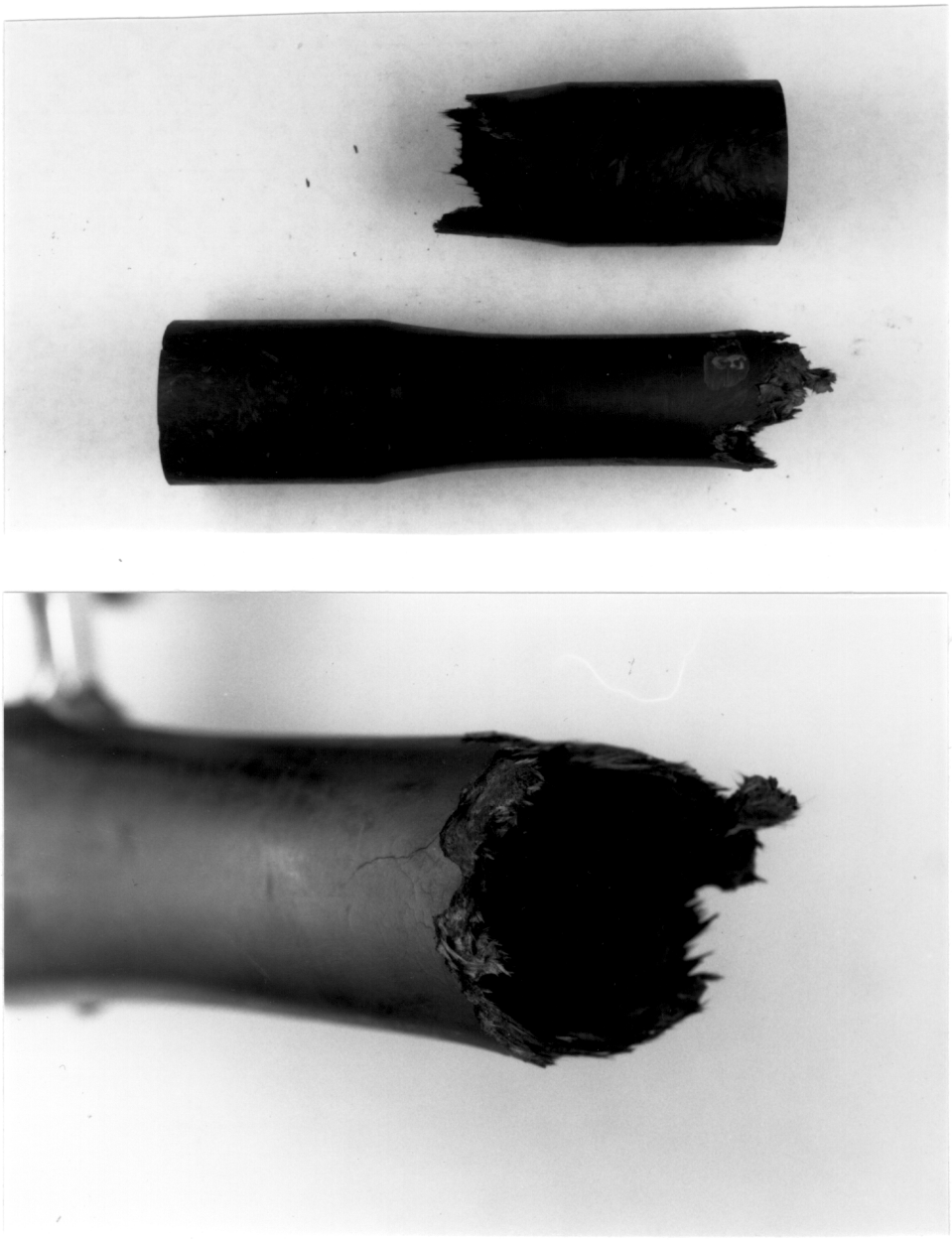

Figure 6.16 Specimen 258-89 After Failure.

comparison of the failure surfaces yields two major differences. First, the failure surfaces for Specimens 261-89 and 260-89 tend to vary in axial location around the circumference; whereas, the failure surface in Specimen 258-89 tends to be located at the same axial location around the entire circumference. Second, the location of the failure surface in Specimen 258-89 tends to be closer to the gage section than the other two failure surfaces.

A magnified examination of the failure surfaces indicate two different types of fiber pullouts. Examples of these fiber pullouts are shown in Figures 6.17 and 6.18. In Figure 6.17 from Specimen 118-89, the pullouts appear to be grouped in large fiber bundles where all of the fibers in a bundle are oriented in the same direction. The ends of these fiber bundles are fairly blunt and are primarily located on the upstream side of the failure surface. In addition, the downstream side of the failure surface appears as a wide, but shallow, canyon. The failure region from Specimen 260-89 shown in Figure 6.18 is slightly different. In this case, exposed fiber bundles are more straw-like, and the canyon along the failure surface in the downstream end of the specimen is much deeper and narrow than observed in Figure 6.17.

Correlation of the above fractography results and the micrographs of the sectioned specimen showing out-of-plane fiber swirling indicates the failure modes in Figures 6.17

Figure 6.17 Fiber Pullout Regions with Blunted Ends in Specimen 118-89.

Figure 6.18 Straw-like Fiber Pullout Regions in Specimen 260-89.

and 6.18 may be significantly different. Figure 6.19 presents a drawing of out-of-plane fiber swirling, and two possible failure modes in connection with this type of fiber swirling. In mode "A", the failure is located at the cusp of the fiber swirl and consists of a transverse failure of the matrix. This type of failure would produce the blunted fiber bundles and the wide, shallow canyons shown in Figure 6.17. A mode "B" failure occurs at the tail of the swirled fiber. This type of failure mode would produce the deeper canyons and the straw-like exposed fibers shown in Figure 6.18. Notice, the mode "B" failure would be located closer the gage section than the mode "A" failure.

In addition to the two failure modes described above, we saw several regions of "in-plane" failure modes. These types of failures occurred along the edge of particularly dominate fiber swirls. Figure 6.20 presents a micrograph of one of these failure regions where the fibers are oriented transversely to the loading direction of the tube. Evaluation of Figure 6.20 indicates a transverse failure of the matrix. Similarly, Figure 6.21 presents a micrograph of a failure region where the fibers are aligned with the loading direction. In this case, it appears we have a shear failure of the matrix.

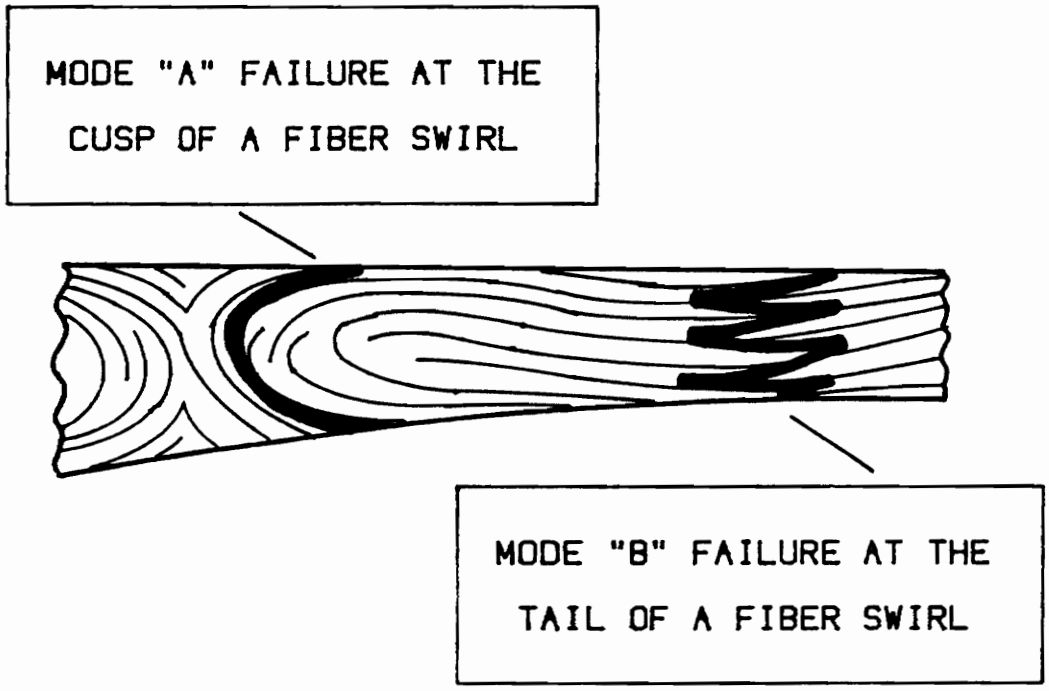

Figure 6.19 Possible Failure Modes Associated with Out-of-plane Fiber Swirling.

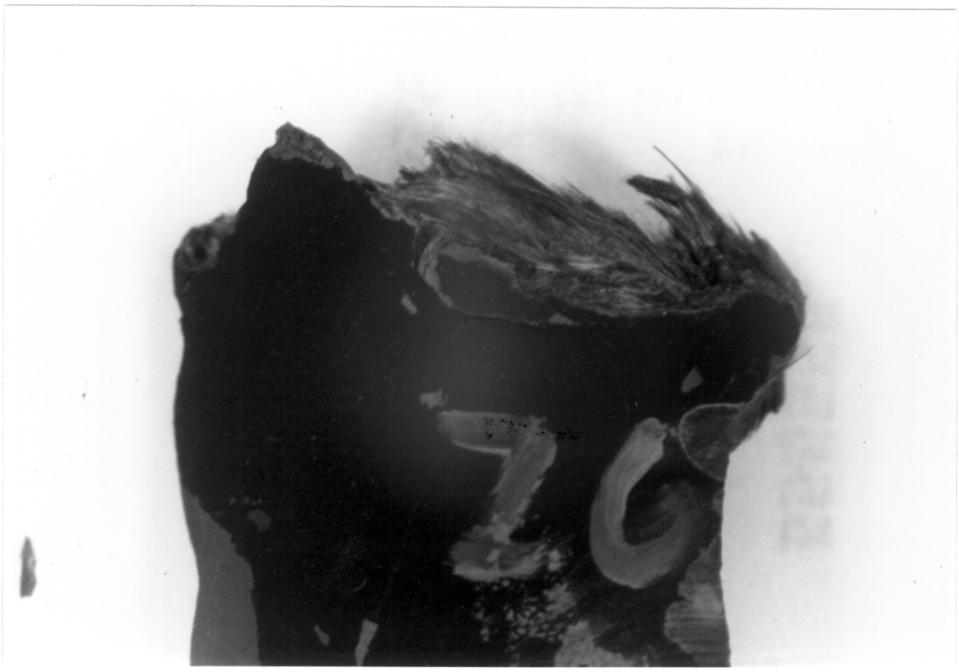

Figure 6.20 Micrograph of a Failure Region Where the Fibers are Oriented Transverse to the Loading Direction.

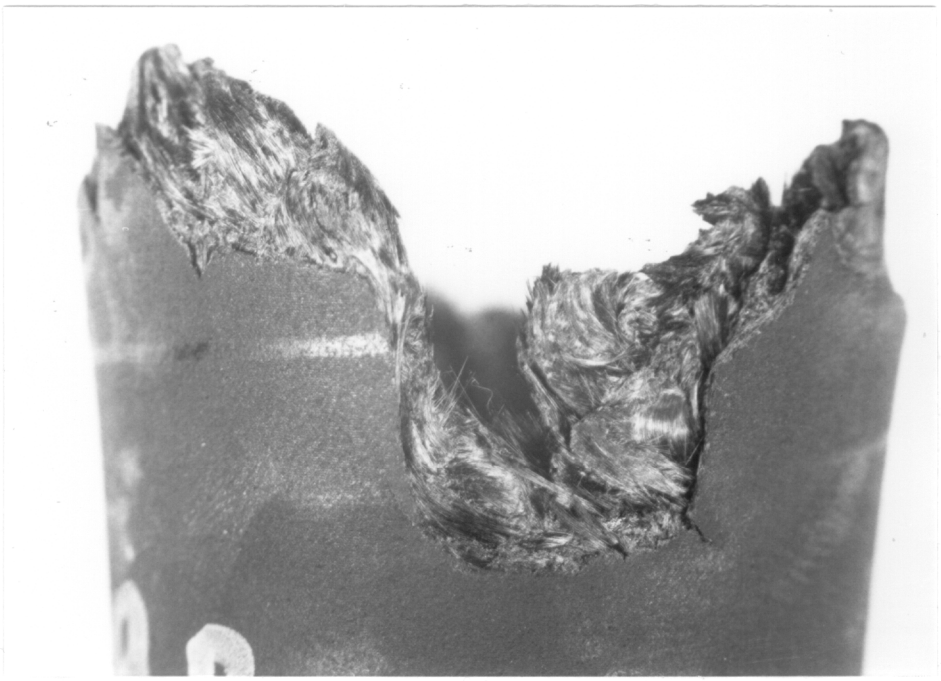

Figure 6.21 Micrograph of a Failure Region Where the Fibers are Aligned with the Loading Direction.

In all of these cases, highly magnified SEM images of fiber ends indicate the fiber-matrix interface at the end of the fiber has failed as opposed to a fiber breakage.

Although all the specimens exhibited a combination of the failure modes described above, the general trends in the failure surfaces of the quasi-static specimens and the high cyclic load specimens are different. The failure surfaces of the quasi-static and the cyclic specimen at 60% of the UTS tend to be dominated by "in-plane" failure modes and mode "A" out-of-plane failure modes shown in Figure 6.19. Conversely, the highly loaded cyclic specimens are dominated by the mode "B" straw-like fiber pullout and deep, narrow canyons. In addition, the amount of "in-plane" failures in the high cyclic load specimens seems significantly less, and the failure surfaces tend to be located closer to the gage section than the quasi-static specimens as expected with the mode "B" failures.

This change in failure modes between Specimens 258-89, cycled at 85% of UTS, and 260-89, cycled at 60% of UTS, could be the result of the wear-in phenomenon shown in Figure 6.22. Early in the load history, transverse cracks develop at the cusp of a fiber swirl. As the load is cycled, these matrix cracks propagate normal to the loading direction and into stronger regions of the material. The load is now transferred across the matrix cracks by fiber bridging. As a result, the stress

Transverse Cracks Develop at the Cusp of the Fiber Swirl

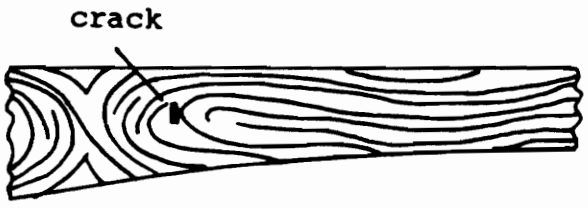

The Transverse Cracks Propogate as Matrix Cracks

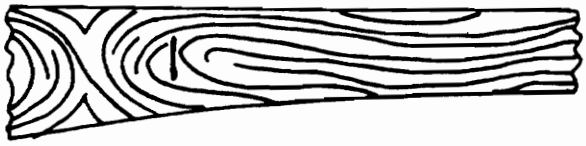

Load is Now Transfered by Fiber Bridging and the Stress Concentration at the Cusp is Reduced

The Failure Site is Then Moved Closer to the Gage Section and the Failure Mode Changes

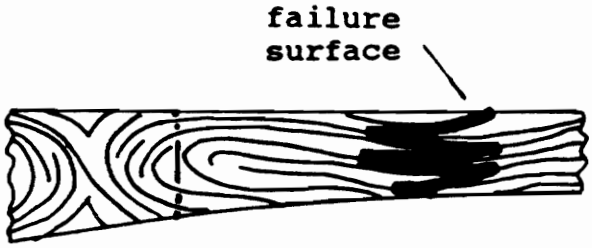

Figure 6.22 Postulated Wear-in Phenomenon for Specimen 258-89.

concentrations associated with the fiber swirl have been reduced, and the failure mode changes to a Mode "B" type failure.

In the case of Specimen 260-89 which was cycled at 60% of UTS, transverse cracks at the cusp of a fiber swirl were initiated. However, the load was not high enough to propagate the matrix cracks into the stronger regions of the material. As a result, the failure modes of Specimen 260-89, due to quasi-static loading after one million cycles, is very similar to the failure modes of the quasi-static specimens. Unfortunately, the limited number of specimens available in this program severely precluded any additional characterization or understanding of this wear-in mechanism. If this material is available for future programs, a thorough investigation of this wear-in mechanism is highly recommended and should prove to be very fascinating.

6.2 Experimental Results for the Bar Specimens.

In addition to the test series with the tubular specimens, a small test series was conducted on bar specimens machined from the downstream grip regions of Specimens 118-89 and 261-89. These specimens were used to determine the transverse strength of the material. The specimens were 1.90 inches long, 0.10 inches thick, and

0.25 inches wide. The 0.25 inch width corresponded to the radial thickness of the grip region. The tests were conducted in the 20 kip Instron, screw machine located in 129 Norris Hall. Unfortunately, an extensometer could not be mounted on the short gage length specimens. As a result, the tests were conducted for strength only. In each case, the specimens were pulled in stroke control up to failure and then removed from the test frame.

After testing, the specimens were inspected under a microscope for the failure location. As expected, many of the specimens failed in the grip regions or at an angle to the loading direction. The results for these specimens were omitted from the transverse strength calculations. Overall, seven specimens exhibited failures which were predominantly perpendicular to the load axis. Figure 6.23 presents a micrograph from one of these failed specimens. In order to calculate the transverse strength, we assumed the axial stress was evenly distributed across the width of the specimen and calculated the transverse strength as simply the applied load divided by the cross-sectional area. For this material, this assumption is fairly reasonable since the elastic modulus of the matrix material is fairly close to the fiber modulus. With this approach, we calculated a transverse strength of 2.57 Ksi, and this strength will be used in the progressive failure analysis described in the next chapter.

7.0 ANALYTICAL MODELING OF DAMAGE DEVELOPMENT IN COMPOSITE COMPONENTS

Quasi-static and fatigue failures of composite materials are a very complex and difficult problems to address. Unlike metals, for which failure is generally controlled by a single flaw growth, composite materials show a variety of failure modes and interaction between these modes which lead to failure. In addition, the internal stress state is highly dependent on the geometric configuration and the material. For injection molded components, the problem is further complicated by the non-uniform fiber distributions throughout the component.

In this section we develop an approach to predict the damage development within a composite component and determine the effects of the damage on strength, stiffness and life of the component. Due to the progressive nature of the damage development process, we perform a progressive failure analysis. In addition, to make the approach applicable to composite components with complex geometries and loadings, the analysis must be based on an approximation technique such as the finite element method. To meet these needs, we have developed a solution technique which parallels the ply discount schemes developed for laminated polymeric composites except we discount a failed element instead of a failed ply. The resulting approach

Figure 6.23 Failure Surfaces for a Specimen Exhibiting Predominantly Transverse Failure.

can handle complex geometries, complex loadings, and local material property degradations.

The remainder of this section contains detailed descriptions of the formulation, execution, and results of the method. Section 7.1 presents an overview of the method and the steps involved in the execution of an analysis. Section 7.2 describes the mechanics which form the basis of the analysis. Section 7.3 describes the interface with the finite element code. Section 7.4 presents the results of the method applied to an injection molded tube specimen subjected to quasi-static tensile loading. Section 7.5 presents results for the method applied to a layered thermoplastic matrix composite plate with a center hole subjected to quasi-static and cyclic loadings. The final section, Section 7.6, discusses the problem areas, limitations, and advantages of the approach.

7.1 General Methodology

The approach is based on the simple methodology depicted by the flow chart shown Figure 7.1. A computer program using this approach was developed on the Sun 3/60 machine and is written in C language. The analysis starts with the development of a standard finite element model using a typical preprocessor. The constructed model is then

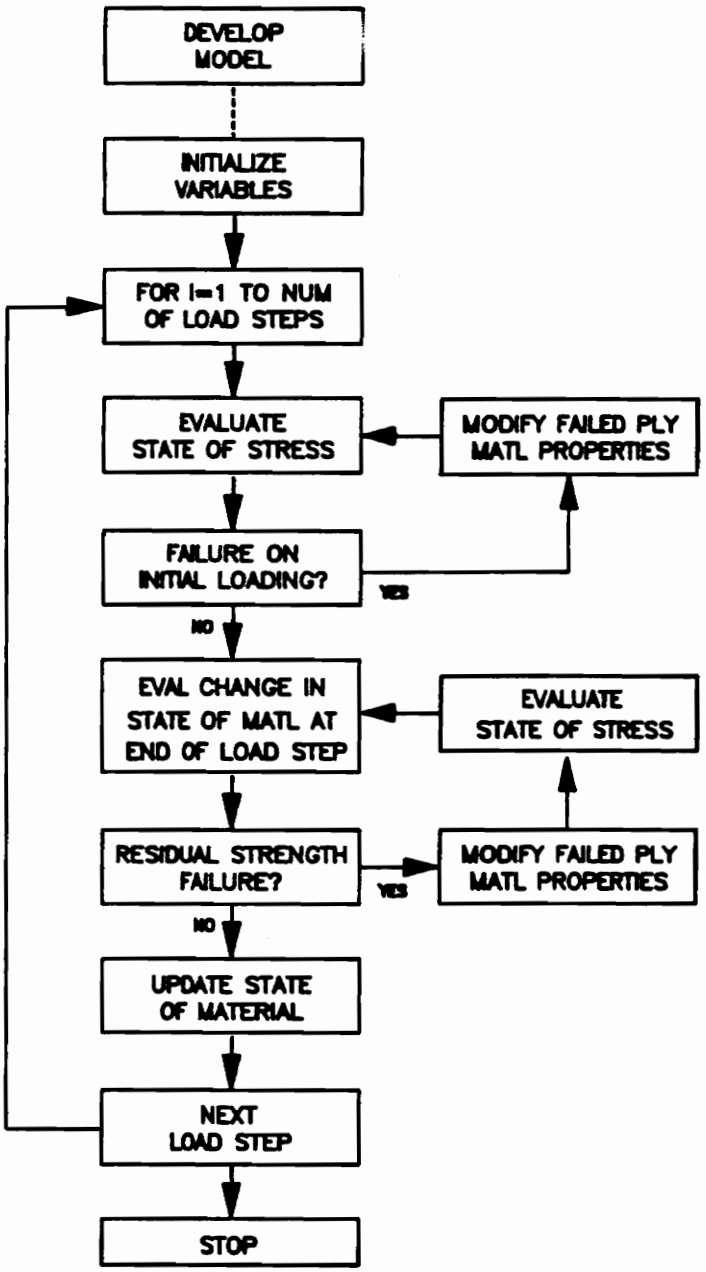

Figure 7.1 Flow Chart of the Analytical Solution Methodology.

written to a file which is subsequently broken into several smaller files with a text editor. The contents of these smaller files will be discussed later in the program. These steps are performed outside of the actual C program. Next, the global load history, S-N parameters, and output file names are specified in the initialization subroutine or procedure. The program is then compiled and executed.

During execution, the program generates a unit loading on the specified loaded elements and calculates the state of stress throughout the structure via a finite element solution for each load step. The stress results are then linearly scaled in order to produce the actual applied loading. Next, we check for element failures using a pre-selected failure criterion. If we have element failures, we determine the element which fails first and then degrade the stiffness of this failed element. The stress state is then re-calculated throughout the entire component, and the failure checks are repeated. Once the failure iteration procedure has been completed, we have the actual state of stress and the state of material throughout the component at the end of the load step.

In the evaluation of the element failures, two types of loadings must be considered. First, we must consider a load increase from one load step to another. Therefore, failures may be predicted in the first half cycle of the loadstep. We will refer to this type of failure as a

quasi-static type failure. The second type of failure is the result of the strength degradation due to the number of cycles in the load step. This type of failure will be termed a residual strength failure.

In the program, we will evaluate the quasi-static type failure based on the state of material at the beginning of the load step, and the residual strength failures will be evaluated based on the state of material at the end of the load step. Therefore, if we consider an incremental loading with no additional cycles in the load step, we do not need to calculate residual strength failure potentials since the residual strengths will not change over the load step. Likewise, if the applied global loads do not change from the previous load step, we do not need to calculate the quasi-static type failure potential since the stress states and failure potentials will be identical to the stress states and failure potentials at the end of the previous load step.

The main advantage of this approach is the simplicity of a linear elastic analysis and the capability of the finite element method to handle complex problems. The same idea can be extended to consider the damage development and life prediction in layered composite materials. For the layered analyses, we check for a ply failure within a layered element, and if a ply failure is predicted, we degrade the ply properties within the element as opposed to

the properties of the entire element. In both cases, by degrading a single element or ply, we can model the damage development on a local level throughout the component.

7.2 Mechanics

In the development of this approach many difficult selections were made with regard to mechanics. The mechanics issues can be divided into two distinct areas, stress evaluation and failure mechanics. The stress evaluation considerations primarily involved the selection of a finite code to solve for the stress distributions. In the area of failure mechanics, we had to consider failure modes to simulate, to select quasi-static and residual strength failure criteria, and to determine stiffness reduction schemes to model a failure. Each of these areas will be discussed in detail.

Although the damage development analysis is fairly involved, the stress evaluation portion of the analysis is a straight-forward linear elastic analysis of a structural component. Therefore, most finite element codes would be acceptable for this analysis, including many of the commercially available finite element codes such as MS-Nastran, ANSYS, ABACUS, Marc etc. The commercially available general-purpose codes also have the advantage of excellent pre- and post-processing capabilities.

For this work, we selected the ANSYS Finite Element Code[54] simply because we have a fair amount of experience with the code. For an injection molded component, the finite element model is constructed with 8-node brick elements (STIF45) where the fiber orientations in the element are specified using the ANSYS ESYS command. The most difficult portion of the analysis is the transfer of the fiber orientations, as measured on the radiographs, to the finite element model. In general, each of the fiber orientations must be specified individually.

For layered composite components, we selected the layered brick element (STIF42) over the layered shell elements since the in-plane shear stresses are significant for the examples we considered. The element formulation is based on classical lamination theory. The reader is referred to Reference 55 for the details of the element formulation and guidelines on the use of these elements.

The failure modes for composite materials can be very complex and show extensive amounts of interaction. However, for this analysis, we will limit the failure modes to fiber failure, matrix cracking parallel to fibers, and shear failure of the matrix. Other failure modes such as laminate buckling or delamination are not considered. For a wide variety of geometries and loading conditions, including the CMC tubes used on this investigation, these failure modes should dominate and, thus, produce acceptable

results. However, in some cases such as components subjected to compressive loading, other failure modes may dominate, and for these cases, the method must be modified to include these other critical failure modes, such as buckling and delamination.

As described earlier, we will consider two types of failure, quasi-static failure and residual strength failure. A quasi-static type failure is defined as a failure at the beginning of a load step due to a change in the applied global loads. Two different failure criterion are included in the analysis for quasi-static failure evaluation. The first criterion is the maximum stress criteria where failure is predicted when at leas one of the following conditions is satisfied:

$$\begin{aligned} S_1/X_t \geq 1, \quad S_1/X_c \geq 1, \quad S_2/Y_t \geq 1, \\ S_2/Y_c \geq 1, \quad S_3/Z_t \geq 1, \quad S_c/Z_c \geq 1, \\ |S_4|/S_{yz} \geq 1, \quad |S_5|/S_{xz} \geq 1, \quad \text{or} \quad |S_6|/S_{xy} \geq 1, \end{aligned} \tag{7.1}$$

where,

$S_1 \ldots S_6$ are stresses defined with respect to the material directions;

X_t and X_c are 1-dir tensile and compressive strengths;

Y_t and Y_c are 2-dir tensile and compressive strengths;

Z_t and Z_c are 3-dir tensile and compressive strengths;

S_{yz} is the shear strength in the y-z plane;

S_{xz} is the shear strength in the x-z plane;

S_{xy} is the shear strength in the x-y plane;

In order to accurately model the state of material and include the effect of strength reductions due to the cyclic loading, X_t, X_c, Y_t, Y_c, Z_t, Z_c, S_{yz}, S_{xz}, and S_{xy} are reduced according the expressions

$$\begin{aligned} X_t &= X_t^\circ * S_{r1} & X_c &= X_c^\circ * S_{r1} \\ Y_t &= Y_t^\circ * S_{r2} & Y_c &= Y_c^\circ * S_{r2} \\ Z_t &= Z_t^\circ * S_{r3} & Z_c &= Z_c^\circ * S_{r3} \\ S_{yz} &= S_{yz}^\circ * S_{r4} & S_{xz} &= S_{xz}^\circ * S_{r5} \\ S_{xy} &= S_{xy}^\circ * S_{r6} \end{aligned} \qquad (7.2)$$

where the $^\circ$ implies the quasi-static strength value for one half cycle, and S_{rj} is the normalized residual strength at the beginning of the load step. Calculation of S_{rj} will be discussed later.

The second, quasi-static failure criterion we included is the Hill Failure Criterion where failure is predicted when

$$(G+H)S_1^2+(F+H)S_2^2+(F+G)S_3^2+2LS_4^2+2MS_5^2+2NS_6^2 \geq 1 \qquad (7.3)$$

where,

$$2H = 1/X^2 + 1/Y^2 - 1/Z^2$$

$$2G = 1/X^2 + 1/Z^2 - 1/Y^2$$

$$2F = 1/Y^2 + 1/Z^2 - 1/X^2$$

$$2L = 1/S_{yz}^2$$

$$2M = 1/S_{xz}^2$$

$$2N = 1/S_{xy}^2$$

In this case, the selection of tension or compression values for X is less obvious. However, in this analysis, $S_1 \geq 0$ implies $X=X_t$, $S_1<0$ implies $X=X_c$, $S_2>0$ implies $Y=Y_t$, and so on. In addition, the strengths are again reduced according to the normalized residual strength value at the beginning of the load step.

Both the maximum stress criterion and the Hill criterion are available for these analyses. For highly three dimensional stress states, the results may be significantly affected by the selection of a failure criterion. However, for the examples considered in this dissertation, the loading is predominantly one dimensional, and we found relatively small differences in the results depending on the failure criterion we selected.

The second failure criterion we need to consider accounts for the strength degradation due to the cyclic loading. In this case, we used a normalized residual

strength reduction expression of the form

$$S_{rj} = 1 - \int_0^{\beta} (1-S_j/S_{uj})\, i(n/N)^{i-1} d(n/N) \qquad (7.4)$$

where,

S_j is the stress in the j-th direction for j=1,...,6;

S_{rj} is the j-th direction residual strength parameter;

S_{uj} is the quasi-static strength in the j-th direction;

n is the number of cycles imposed at stress S_j;

N is the cycles to failure at stress S_j;

$\beta = (n/N)$;

i is a sudden death parameter generally equal to 1.2,

We can expand the integral to get

$$S_{rj}{}^k = 1 - \int_0^{\beta^{k-1}} \ldots d(n/N) - \int_{\beta^{k-1}}^{\beta^k} \ldots d(n/N) \qquad (7.5)$$

or

$$S_{rj}{}^k = S_{rj}{}^{k-1} - \delta S_{rj}{}^k \qquad (7.6)$$

where $\delta S_{rj}{}^k$ is the decrement in residual strength during load step k, and

$$\delta S_{rj}{}^{k} = \int_{\beta^{k-1}}^{\beta^{k}} (1-S_j/S_{uj})\, i\,(n/N)^{i-1} d(n/N) \qquad (7.7)$$

If we assume S_j is constant over the entire load step, we can integrate this expression to get

$$\delta S_{rj}{}^{k} = (1-S_j{}^{k}/S_{uj})[(n^{k}/N^{k})^{i} - (n^{k-1}/N^{k-1}) \qquad (7.8)$$

Notice N^{k} and N^{k-1} are calculated from the stress-life expression based on the stresses $S_j{}^{k}$ and $S_j{}^{k-1}$ respectively. This expression for $\delta S_{rj}{}^{k}$ is the decrement in strength due to load step k. For example, the tensile strengthof the material in the fiber direction after load step k is given by

$$X_t = X_t{}^{\circ} * (S_{rj}{}^{k-1} - \delta S_{rj}{}^{k}) \qquad (7.9)$$

Similar expressions characterize the material strengths for X_c, Y_t, ... S_{xy}.

Once we have calculated the new material strength at the end of the load step, we can now use either the maximum stress criterion or Hill's criterion to calculate failure potentials for each element ply. If any of the failure potentials are greater than unity, failure is predicted.

In order to simulate a failure, we reduce the appropriate stiffnesses of the failed element or ply by 90

percent. The stiffnesses that are reduced correspond to the failure mode. Therefore, in the pre-processing phase of the method, we generate several sets of material properties. Each material property set corresponds to a specific failure mode for an element.

As previously discussed, we will consider three types of failure. These include fiber failure, matrix failure, and shear failure. In addition, these failure modes may be coupled. For example, if we predict a shear failure by the maximum stress criteria, we will assume the shear loads generate a matrix crack in the ply. Therefore, we will degrade the shear stiffness, the transverse stiffness, and the 2-3 Poisson's ratio by 90% to simulate the failed ply. Table 7.1 presents the coupled stiffness degradations for the various failure modes. The combined failure is defined as a total failure in all directions. For example, an element or ply that fails according to the maximum stress criterion in both the X and the Y directions will be assigned a material type 8. When using the Hill criterion, we assume the first predicted failure due to combined loading produces a matrix crack in the ply, and we degrade the appropriate stiffnesses associated with matrix failures. Once a matrix failure has been predicted, we neglect the interaction effects between the stresses and switch to a maximum stress criterion in order to predict the last potential failure mode: fiber failure.

Table 7.1 Stiffness Degradations for Various Failure Modes.

Failure Mode	Degraded Stiffnesses	Matl Type
No Failure	(none)	1
Max Str - X	E_1, G_{12}, NU_{23}, NU_{12}	6
Max Str - Y	E_2, G_{12}, NU_{23}	7
Max Str - S_{xy}	E_2, G_{12}, NU_{23}	7
Hill Theory	E_2, G_{12}, NU_{23}	7
Combined	E1, E_2, G_{12}, NU_{23}, NU_{13}, NU_{12}	8

In order to fully utilize the technique, we need a full array of material properties. These properties include quasi-static strengths for the longitudinal, transverse and shear directions. In addition, we would need Stress-Life curves for each of the directions to perform a cyclic analysis. Generation of the cyclic data to verify the approach is beyond the scope of this work and will not be considered in this report.

This completes the development of the mechanics for the solution process. In summary, the stress state is calculated with a linear elastic finite element model. Failure is then predicted with either a maximum stress criterion or a Hill's criterion at the element level. If a failure is predicted, the load redistribution due to failure is simulated by local element stiffness degradations. Notice the entire procedure is built on relatively simple, but sound, mechanics.

7.3 The ANSYS Interface

The program is written to specifically interface with the ANSYS finite element code. The ANSYS interface can be divided into four different categories: model development, solution execution, solution reading, and model modification. The finite element model is developed with the standard ANSYS preprocessor (PREP7). In PREP7, we

define the element types (STIF45 or STIF42), the nodes, the elements, sets of undamaged and damaged material properties, the displacement constraints, and the unit element pressure loadings. For injection molded components, we also need to input the fiber directions for each element using the ESYS command in PREP7. For layered components we need to generate real constant sets for each element which contain the thickness, orientation, and materials property set for each layer in the element.

Upon completion of the model development, the model is written to "file28.dat" using the CDWRITE command in PREP7. "file28" is then divided into four smaller files using a standard text editor (such as vi on the Sun 3/60). The first file must be named "prep7in1", and it will contain the element type information and the nodal information. The second file, "prep7in2", contains the element information including the material property set or the real constant set for each element depending on which type of component is being investigated. The third file, "prep7in3" contains the material properties for each material property set and the displacement constraints. The final file, "prep7in4", contains the real constant sets for each element. This file is not required for the analysis of injection molded components.

Solution execution is performed in a three step process. Using the C "system" command, we can execute the

commands in file "ansysbatch" which in turn executes the commands in the files "prep7bat", "solvebat", and "p27bat". "prep7bat" reads the files "prep7in1" through "prep7in4", assembles the new model, writes the solution execution file ("file03.dat"), and writes a "file28.dat" for this load step. Upon completion of "prep7bat", "file28.dat" is copied to file "prep7_xx" where xx is the load step. Therefore, after execution of the entire program, we can go back and use "prep7_xx" to resolve for the final state of stress associated this load step.

Once "prep7bat" is completed and "file28.dat" is copied, the file "solvebat" then performs the actual execution of the ANSYS analysis to determine the stress state. The finite element solution generates files "temp" and "file12.dat". "temp" is an ascii file which contains the solution printout. "file12.dat" is a binary file which contains the solution results for post-processing. "file12.dat" can be used to generate displacement plots, stress contour plots for a ply, etc. Once "solvebat" is completed, "file12.dat" is then copied to file "post1_xx" for later post-processing. The final execution file, "p27bat", calls the ANSYS post-processing routine POST27 and generates a file containing the stress state at the element or ply centroid in the material directions. This stress state file is then copied to file "p27out_xx".

Upon completion of "ansysbatch" we need to read the stresses at the center of each element from the stress state file. The file will contain a large amount of extraneous data which we do not need. Therefore, we first scan through the file until we find the element stress results. Next, we read the element results in a matching format to determine the centroidal stresses. The element or ply stresses are used throughout the remainder of the analysis for failure evaluations and residual strength degradations.

During execution of the C program, we must modify the finite element model to change the load history and simulate damage progression. In order to simulate the damage development, we degrade the material properties in the failed element or ply by assigning a new material property set containing reduced stiffnesses to the failed element or ply. The C program then writes a new "prep7in2" or "prep7in4" file with the modified element information and then solves the finite element problem with this new set of material properties to produce the modified state of stress throughout the structure.

In summary, the ANSYS input files are generated outside of the program and then are modified corresponding to the damage state. The ANSYS output files are read into the program in order to determine the stress state and to predict additional damage development in the component.

Overall, the ANSYS interface is simply a large amount of input and output file manipulation.

7.4 Application of the Method to the Injection Molded Tubes

As a first example, we applied the modeling technique to an injection molded tube subjected to quasi-static loading. A finite element model was constructed to represent the tube. Eight node brick elements (Stif45) were used to model the 5.0 inch portion of the tube extending outside the grips. A picture of the model is shown in Figure 7.2. For these models, we assumed the radial stress gradients were small. Therefore, one element through the thickness was sufficient.

The most difficult area in the construction of the model involved the determination of the fiber orientations based on the x-ray radiograph of specimen 118-89. For this analysis, we attempted to transpose the finite element grid over the x-ray radiograph and then assign a fiber orientation to each element (Figure 7.3). The arrow head in each element points in the direction of the elements fiber direction. In some cases, a dominating fiber orientation was not evident, and we assigned the element fiber orientation based on the orientations in the adjoining elements. In this analysis, the out-of-plane

Figure 7.2 The Finite Element Model of the Tube.

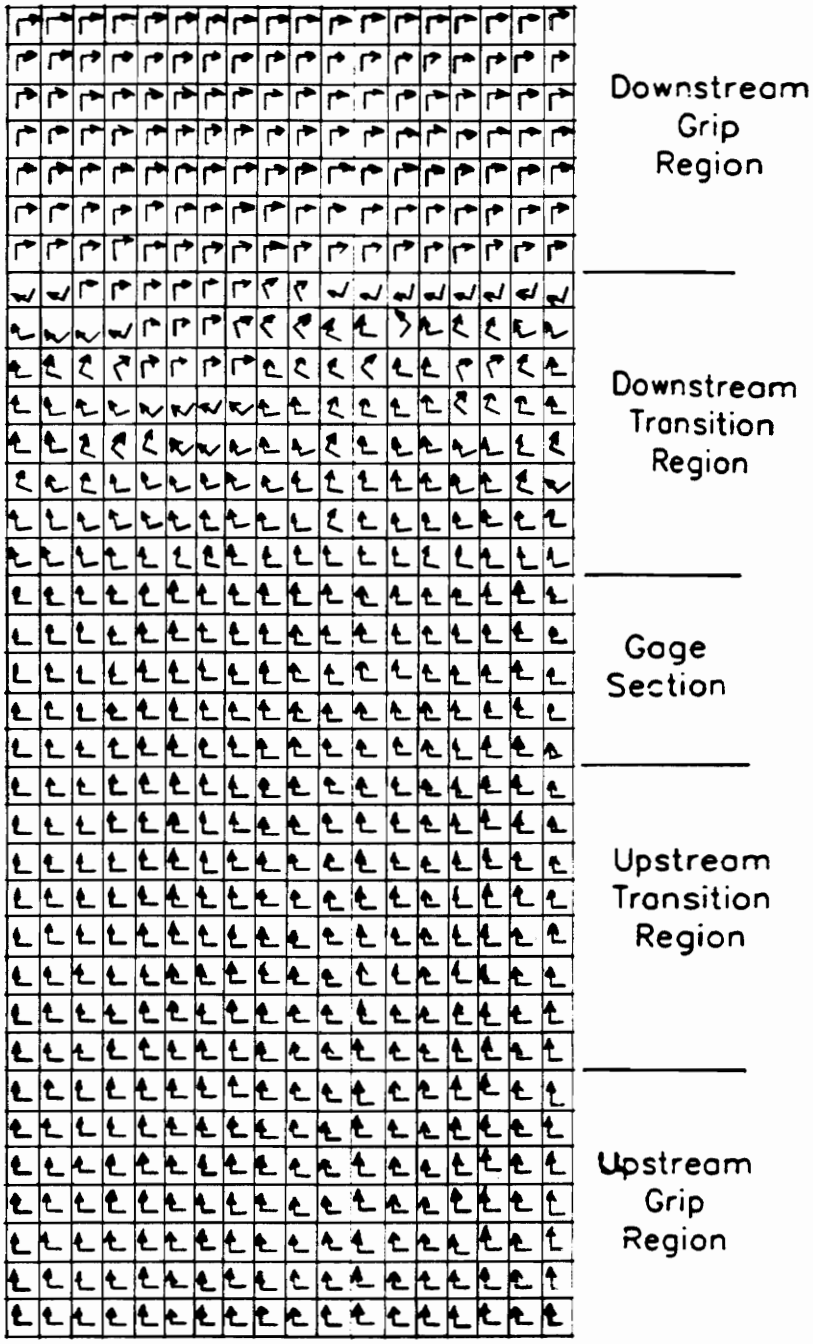

Figure 7.3 Material Axes for the Elements in the Model.

material properties were oriented in the radial direction.

The elastic properties for the undamaged material were based on the information provided by UTRC described in Chapter 3, and are summarized in Table 7.2. Notice the properties are presented in material coordinates. These undamaged elastic proprieties were identified as material property set 1.

The longitudinal tensile and shear strengths for the failure analysis were based on the data provided by UTRC, and the transverse tensile strength was based on the tension bar test results described in Chapter 6. These strengths are also summarized in Table 7.2. For the tensile loading investigated in this program, the radial tensile strength and the compressive strengths were not required.

The Hill failure criteria was used throughout the analysis, and if a failure was predicted, we assumed a 99% degradation factor for the longitudinal and transverse stiffness properties. Other failure modes were not included in the model.

The boundary conditions for the model consist of UZ=0.0 displacement constraints along the bottom edge of the model. In addition, two nodes were fixed to eliminate any rigid body motion. The loads were applied in a two step process in order to simulate the loading sequence in a servo-hydraulic test frame. In the model, one end of the

Table 7.2 Material Properties for the Tube Analysis.

Undamaged Material - Material Property Set 1

E_1 = 8500 ksi	G_{12} = 800 ksi	NU_{12} = .30
E_2 = 5000 ksi	G_{13} = 800 ksi	NU_{13} = .43
E_3 = 5000 ksi	G_{23} = 800 ksi	NU_{23} = .43

Tensile and Shear Strength Properties

X_t = 15.0 ksi	Y_t = 2.57 ksi	S = 5.50 ksi

Damaged Material - Material Property Set 8

E_1 = 85.0 ksi	G_{12} = 8.0 ksi	NU_{12} = .30
E_2 = 50.0 ksi	G_{13} = 8.0 ksi	NU_{13} = .43
E_3 = 50.0 ksi	G_{23} = 8.0 ksi	NU_{23} = .43

specimen was given a uniform displacement, and the finite element analysis is performed to determine the stress state throughout the specimen and the reaction forces at the imposed displacements. The reaction forces are then summed to calculate the total load (P_m) on the model. Next, a scale factor is determined by dividing the required applied load (P_t) for the load step by P_m, and finally, all the stresses throughout the model are linearly scaled to produce the stress state required for the load step. This linear scaling of the stress state is acceptable due to the linearity of the modeling approach. Notice, for short specimens, this loading scheme can be significantly different than simply applying a uniform pressure distribution across the end of the specimen for short specimens.

For this analysis, we will present the analytical results in the form of damage maps. A shaded element in a damage map indicates a predicted failure for that element. The initial predicted damage is shown in Figure 7.4 and occurs at 1470 pounds. This damage is located in a heavily swirled region seen on the radiograph (Figure 6.1). The next failure is predicted at 1510 pounds and propagates until the specimen is completely failed. The first several failure locations at the ultimate load of 1510 pounds are shown in Figure 7.5.

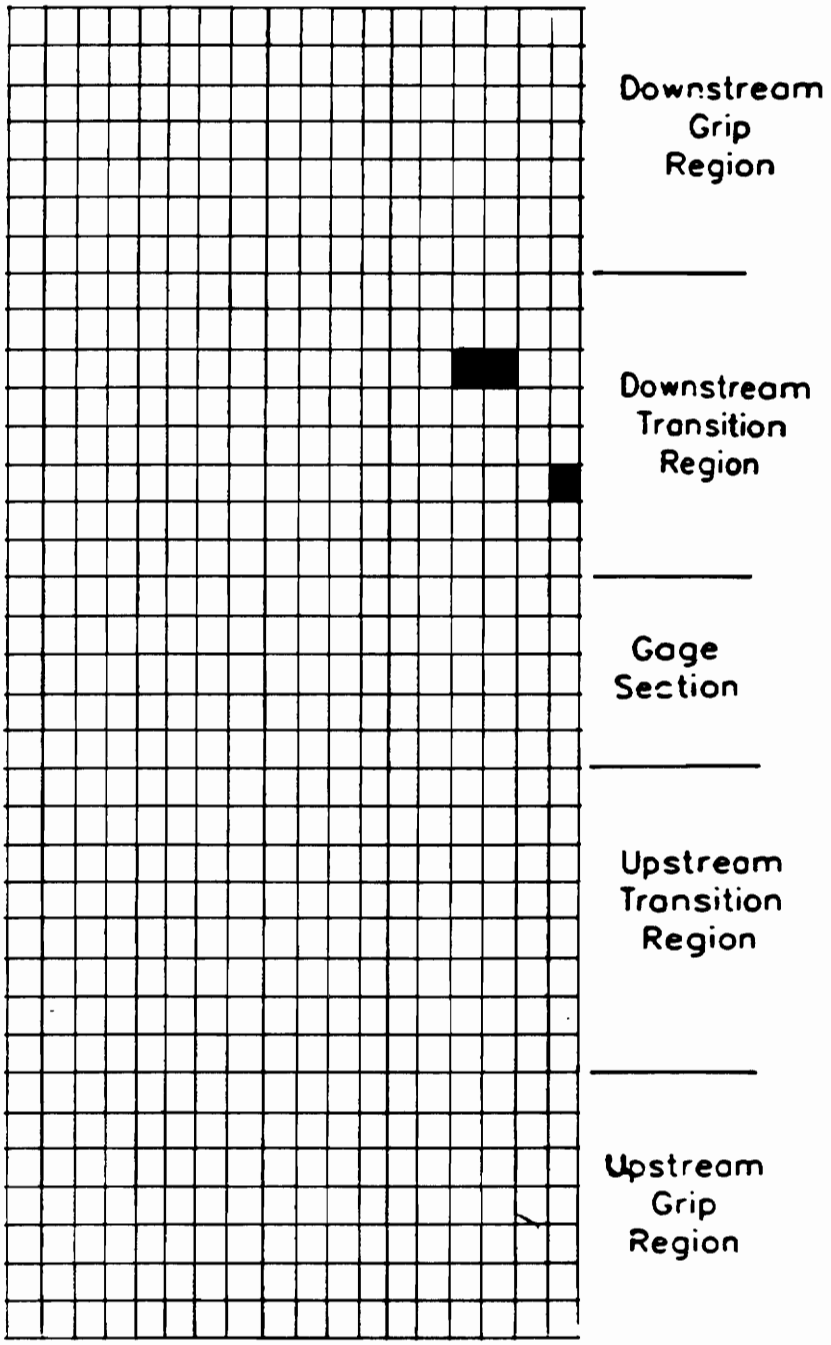

Figure 7.4 Predicted Location of the Initial Damage.

Comparison of the analytical and experimental results shows a mixed correlation between the two results. On one hand, the predicted failure loads are significantly lower than the measured failure loads. The first element failure is predicted at 1470 pounds axial force, whereas, in the actual test specimen, the first failure, as indicated by an increase in the acoustic emissions activity, was thought to occur at approximately 2400 pounds. The ultimate loads at failure show even a greater discrepancy, In this case, the predicted ultimate load for the tube is 1510 pounds, and the measured ultimate load is 4150 pounds. Sources of these discrepancies will be discussed in Section 7.6. Comparison of the predicted and actual failure surfaces show a much better correlation. Figure 7.6 overlays the failure surface on the predicted failure path as determined from an X-ray radiograph of the failed tube. Notice the correlation between the predicted and experimental results is excellent.

7.5 Application of the method to layered Composites Components

In addition to the injection molded tube example discussed in the previous section, we applied the method to a 1.5 inch wide, layered thermoplastic matrix composite plate, with a 0.375 inch diameter center hole subjected to

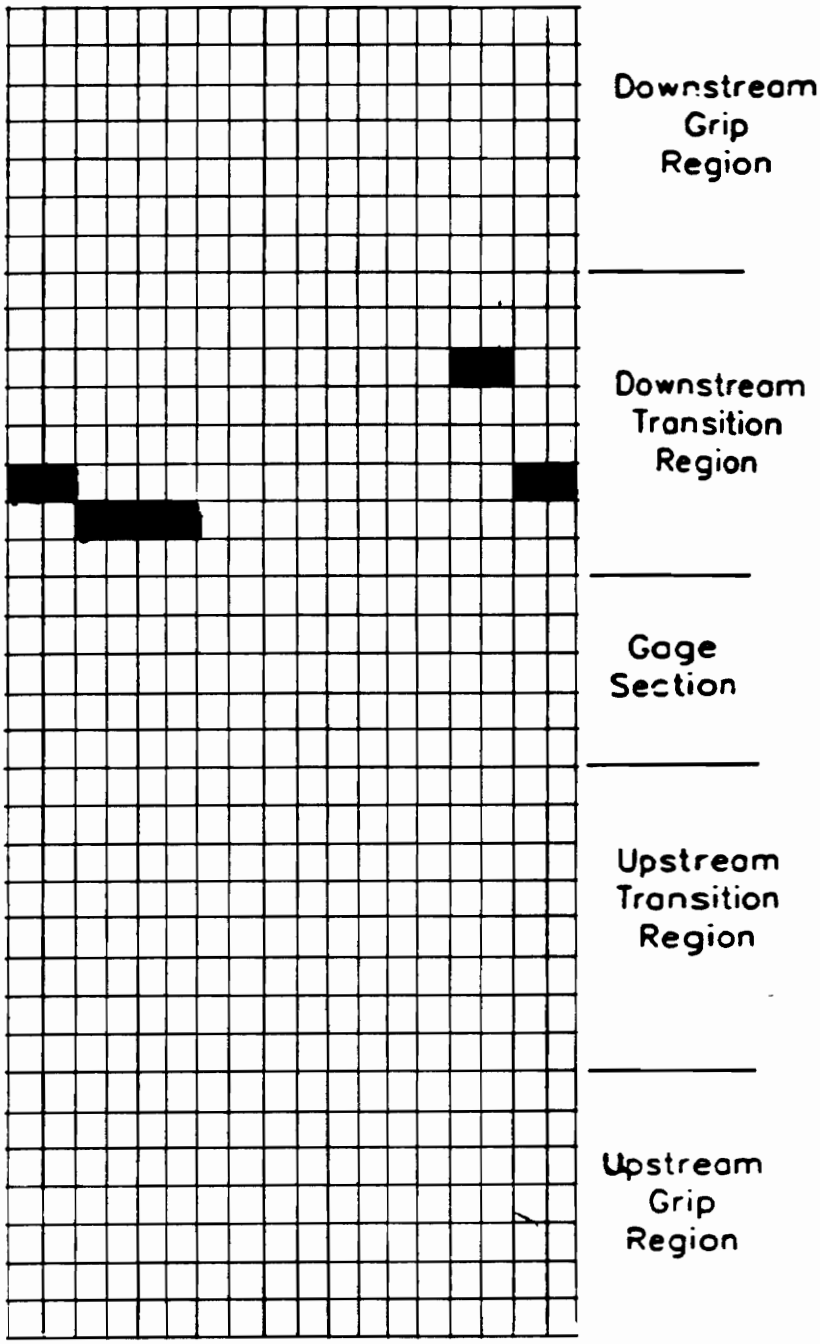

Figure 7.5 Predicted Damage Sites at 1510 Pounds.

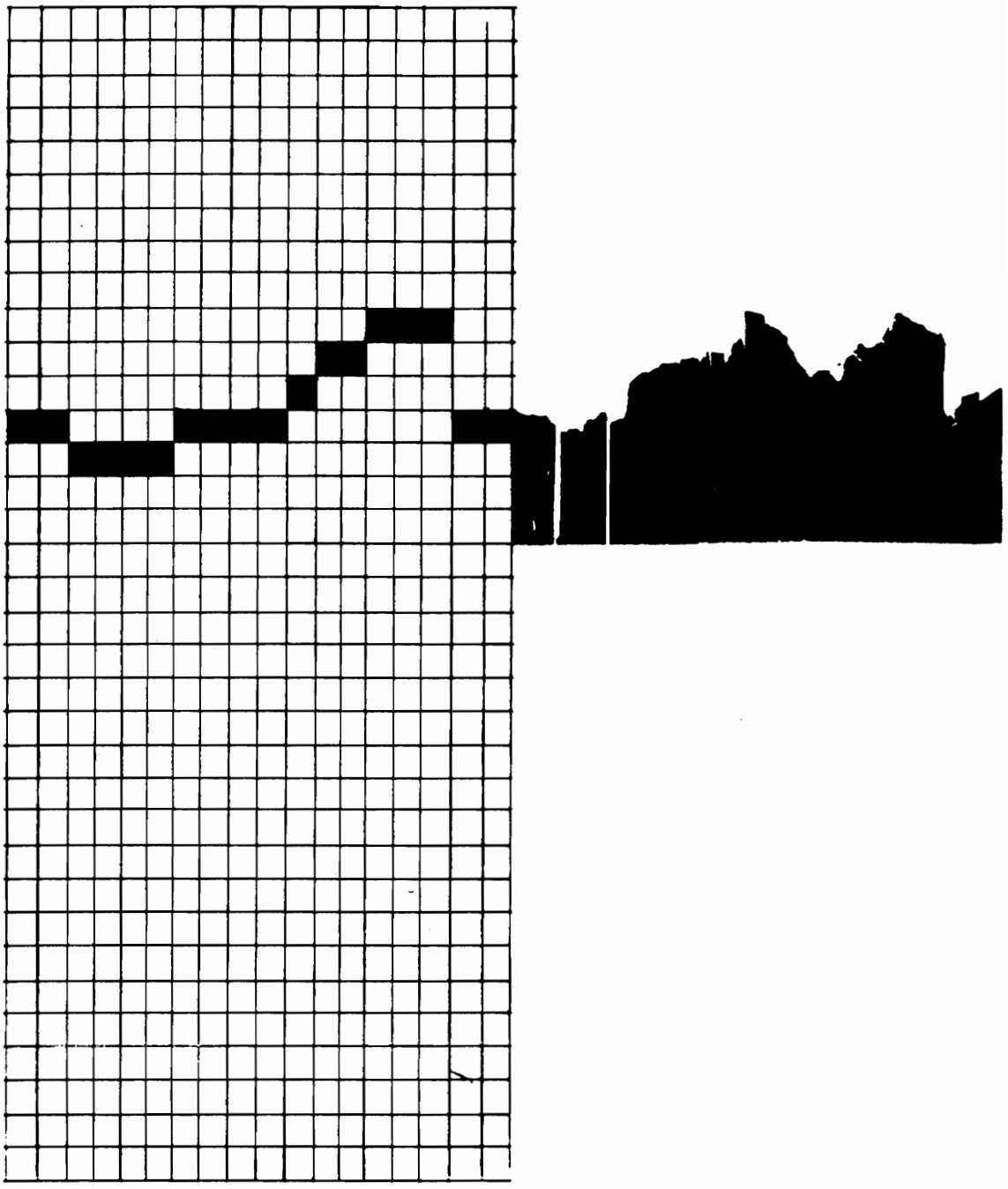

Figure 7.6 Comparison of the Predicted and the Observed Failure Locations.

axial tension. The dimensions of the specimen and the global coordinate system are shown in Figure 7.7. The plate contained 8 plies of a T650-42/Radel-X material in a $[0/+45/0/-45]_s$ stacking sequence. The ply thickness for this material is 0.00525 inches giving a total laminate thickness of 0.042 inches. Two load cases were considered. The first load case investigates the effects of quasi-static loading, and the second load case considers cyclic loading at 77% of the quasi-static strength.

The laminate was modeled with the full plate, finite element model shown in Figure 7.8. Displacement constraints were imposed at x=-L/2 in order to fix one edge of the model and to restrict the out of plane motion. As with the tube model, we applied a unit displacement along the edge x=L/2 and then summed the calculated force resultants along the edge x=L/2 in order to determine the scaling factor for the stresses throughout the model.

The majority of the material properties and S-N curve parameters used throughout this analysis were taken from Reference 56. Unfortunately, compression and shear properties were not available. Therefore, we assumed the compression strengths and S-N parameters were identical to the tensile properties, and for a shear fatigue response, we estimated the shear S-N curve midway between the axial and the transverse properties. These properties are material set 1 and are summarized in Table 7.4.

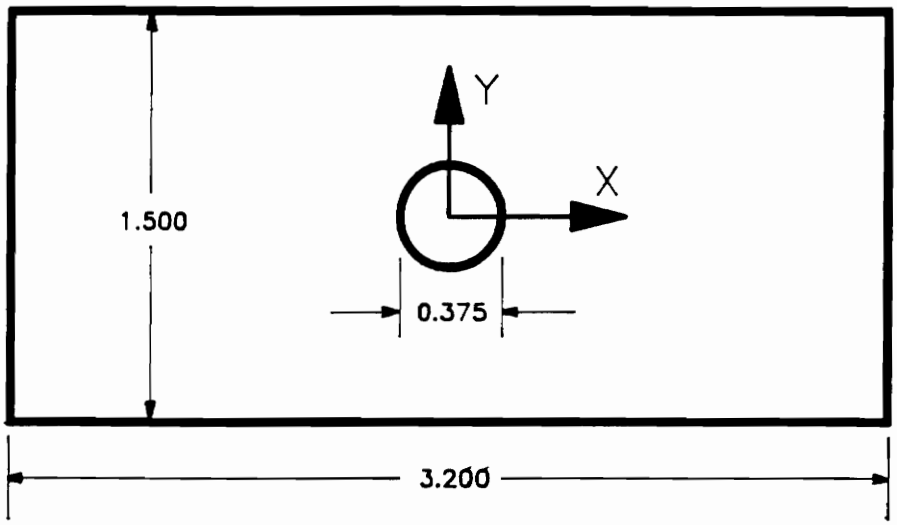

Figure 7.7 Specimen Dimensions and Global Coordinates for the Layered Composite Model.

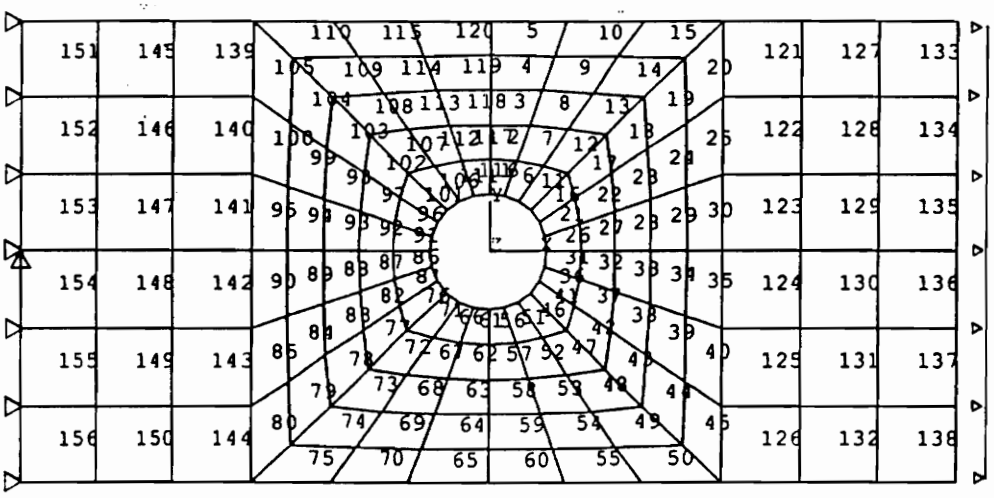

Figure 7.8 Finite Element Model for the Layered Plate.

Table 7.3 Material Properties for the Layered Model.

Undamaged Elastic Properties

E_1 = 22900 ksi	NU_{12} = .38	G_{12} = 830 ksi
E_2 = 1085 ksi	NU_{13} = .38	G_{13} = 830 ksi
E_3 = 1085 ksi	NU_{23} = .45	G_{23} = 300 ksi

Lamina Strengths

X_t° = 320 ksi	Y_t° = 10.56 ksi	Z_t° = 10.56 ksi
X_c° = 320 ksi	Y_c° = 10.56 ksi	Z_c° = 10.56 ksi
S_{xy} = 15.00 ksi	S_{xz} = 15.00 ksi	S_{yz} = 15.00 ksi

S-N Paramters: $\log(S_i/S_{ui}) = B_i * \log(N_i) + A_i$

A_{1t} = 0.0	A_{2t} = 0.0	A_{3t} = 0.0
B_{1t} = -0.0263	B_{2t} = -0.0946	B_{3t} = -0.0946
A_{1c} = 0.0	A_{2c} = 0.0	A_{3c} = 0.0
B_{1c} = -0.0263	B_{2c} = -0.0946	B_{3c} = -0.0946
A_4 = 0.0	A_5 = 0.0	A_6 = 0.0
B_6 = -0.060	A_6 = -0.060	B_6 = -0.060

In order to simulate a transverse or shear failure in a ply, we degraded the transverse stiffness, the shear stiffness and the out-of-plane Poisson's ratio. These resulting material properties were then identified as material set 7 and are shown in Table 7.5. In order to simulate a longitudinal or fiber failure, we degraded all of the stiffnesses and the Poisson's ratios. These degraded material properties were then identified as material type 8 and are also shown in Table 7.5.

Two different load histories were investigated to demonstrate the capabilities of this modeling approach. The first loading case considers the progressive failure of the laminate under quasi-static loading, and the second loading case investigates the damage development due to fatigue loading at 77% of the ultimate tensile strength. In both cases, we used a maximum stress criteria throughout the analyses, and the analyses were terminated when we had the first fiber failure in a 0° ply.

The solution procedure generates a vast amount of information for post-processing, and it is difficult to select which portion of this information provides the best insight into the capabilities of the modeling technique. For this dissertation, we focused on the damage progression throughout the load history which will be presented in the form of damage maps. A shaded element in a damage map indicates either transverse or shear failure. Since both

Table 7.4 Material Property Sets for Failed Elements

Shear and Transverse Failure - Material Set 7

E_1 = 22900 ksi	NU_{12} = .38	G_{12} = 830 ksi
E_2 = 108.5 ksi	NU_{13} = .38	G_{13} = 83 ksi
E_3 = 1085 ksi	NU_{23} = .045	G_{23} = 300 ksi

Fiber and Combined Failure - Material Set 8

E_1 = 2290 ksi	NU_{12} = .038	G_{12} = 83 ksi
E_2 = 108.5 ksi	NU_{13} = .038	G_{13} = 83 ksi
E_3 = 108.5 ksi	NU_{23} = .045	G_{23} = 30 ksi

failures are assigned the same degraded material property set after failure, we do not differentiate between the two failures in the damage maps. Both analyses were terminated at the first fiber failure in a zero degree ply.

Figures 7.9 and 7.10 present damage maps for the quasi-static loading case at 69.6 ksi and 70.4 ksi respectively. These are the only predicted damage states in the material before final failure at 78 ksi. As is typically observed in the laboratory for quasi-static specimens, we predict a very small amount of damage located just along the edge of the hole prior to final failure.

The second load case for the plate model considers a cyclic loading at a maximum stress of 60 ksi, which is 77% of the laminate UTS. Figures 7.11 through 7.14 present the damage maps at 100, 1000, 10000, and 50000 cycles respectively. Failure for this load case is predicted at 56100 cycles. If we did not include the damage development and simply based the fatigue life on the stress state in the undamaged laminate, we would predict a life of over 5.2 million cycles to failure. Clearly, the damage development process significantly affects stress state within the laminate and the predicted performance of the laminate.

Figure 7.15 presents the effect of damage development and loading on the 0° ply stress of element 1, which is at the edge of the hole. For this figure, the stress is normalized based on the 0° ply stress (193 ksi) at the edge

0

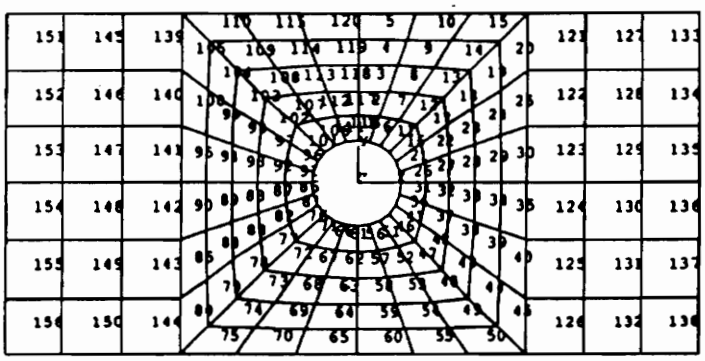

+45

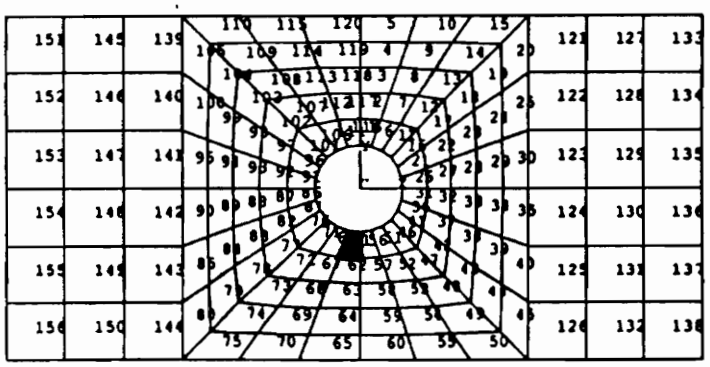

-45

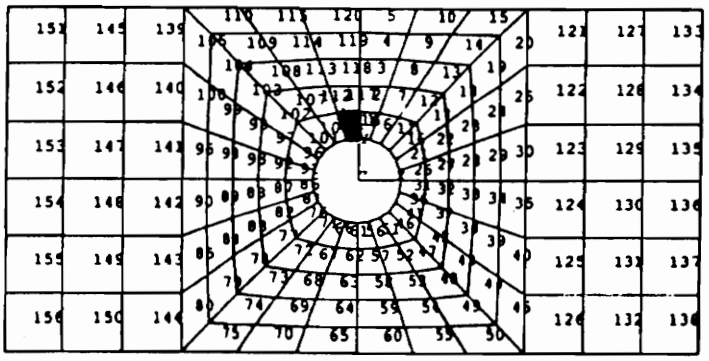

Figure 7.9 Damage Maps for Quasi-static Loading at 69.6 Ksi.

0

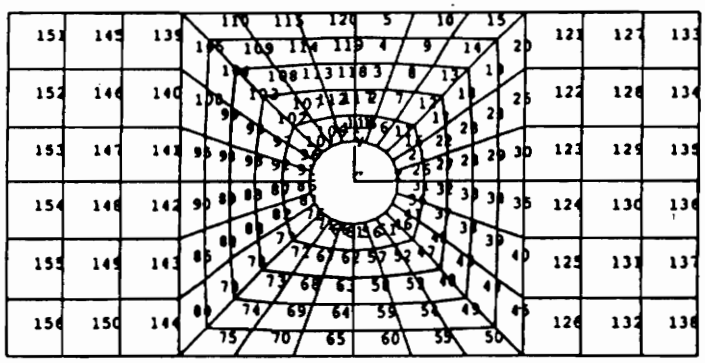

+45

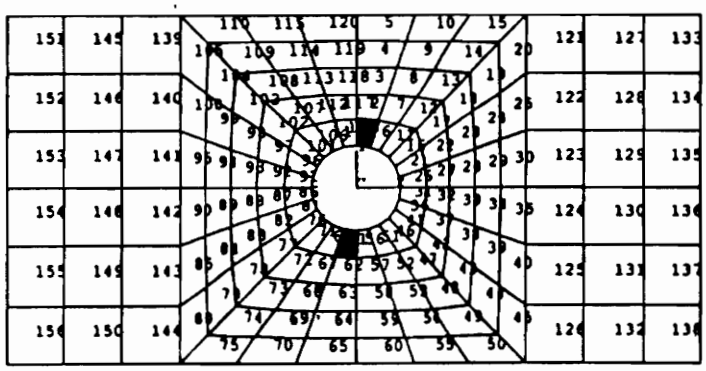

-45

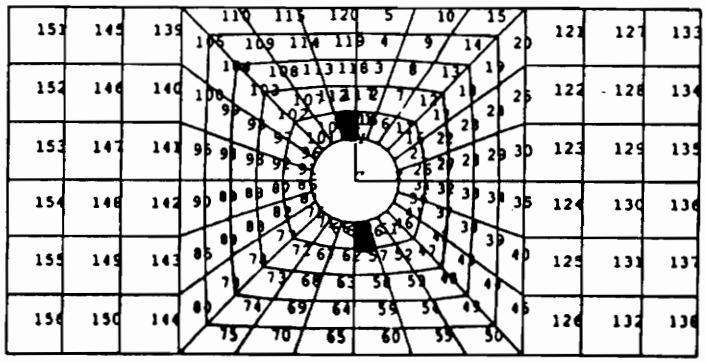

Figure 7.10 Damage Maps for Quasi-static Loading at 70.4 Ksi.

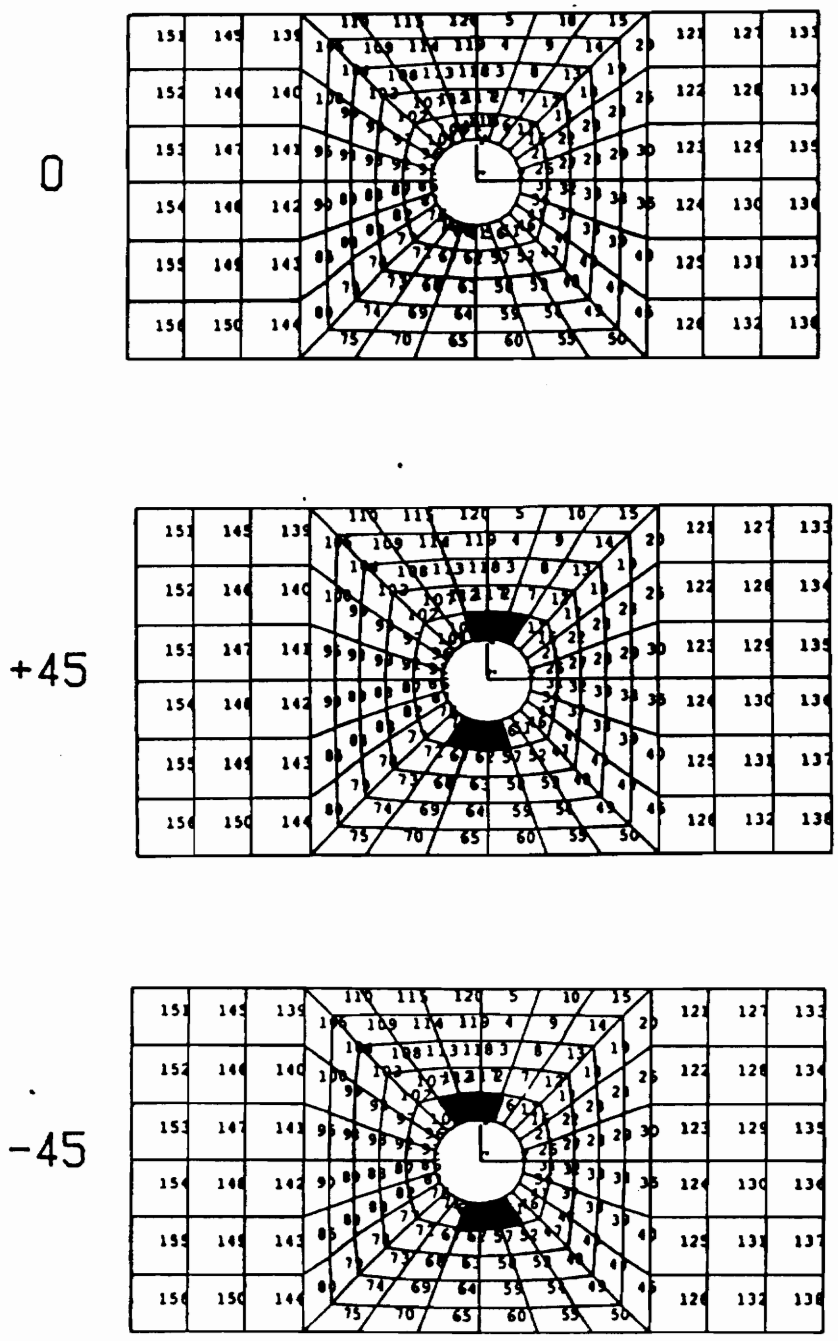

Figure 7.11 Damage Maps for Cyclic Loading at 77% of UTS after 100 Cycles.

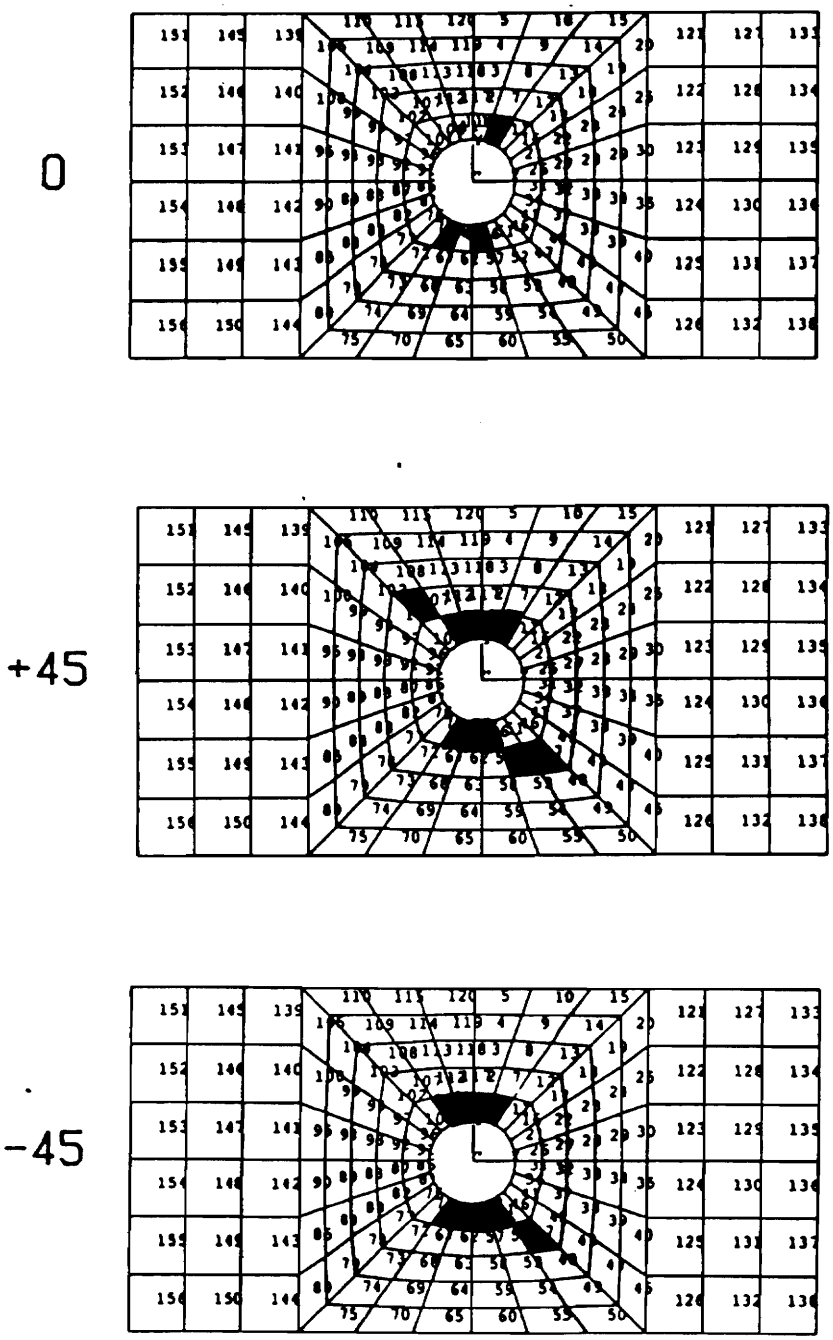

Figure 7.12 Damage Maps for Cyclic Loading at 77% of UTS after 1000 Cycles.

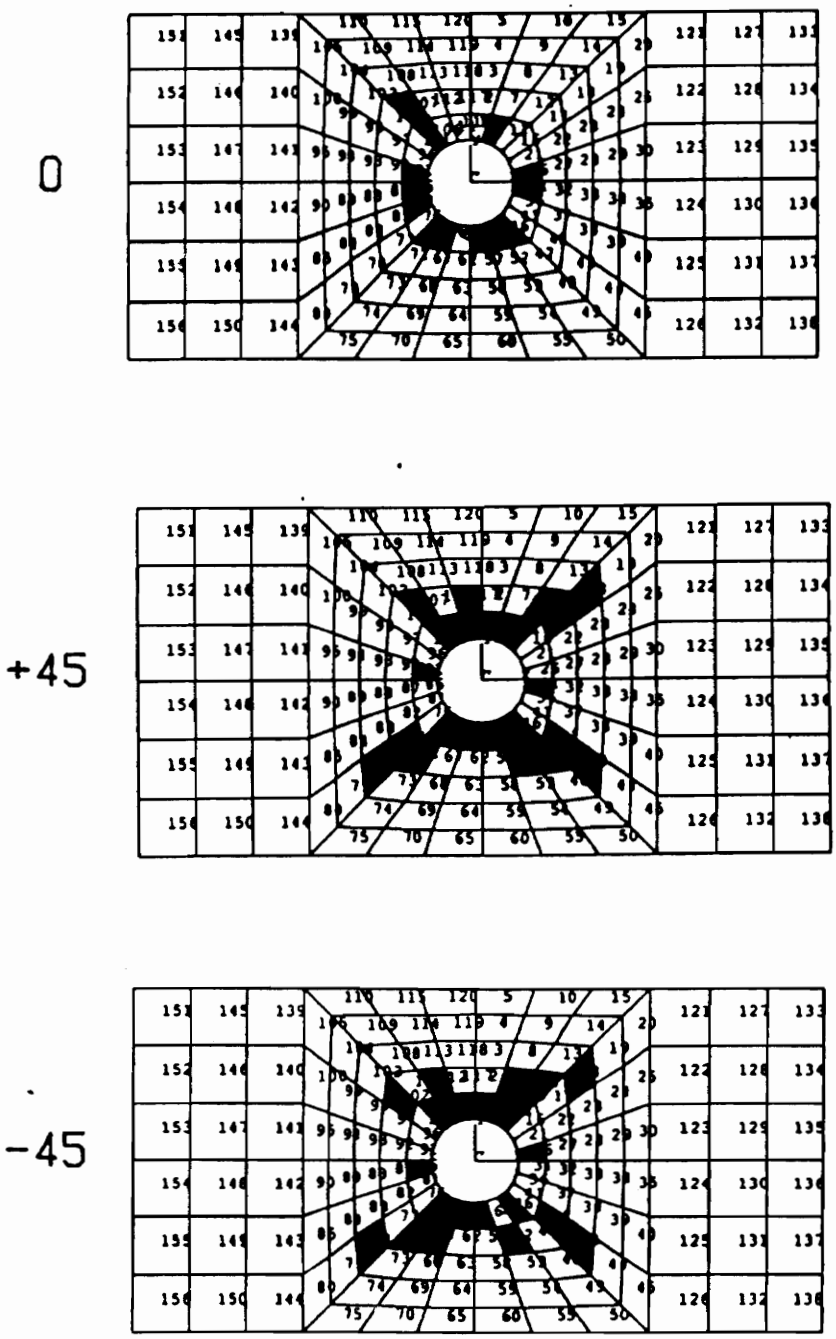

Figure 7.13 Damage Maps for Cyclic Loading at 77% of UTS after 10,000 Cycles.

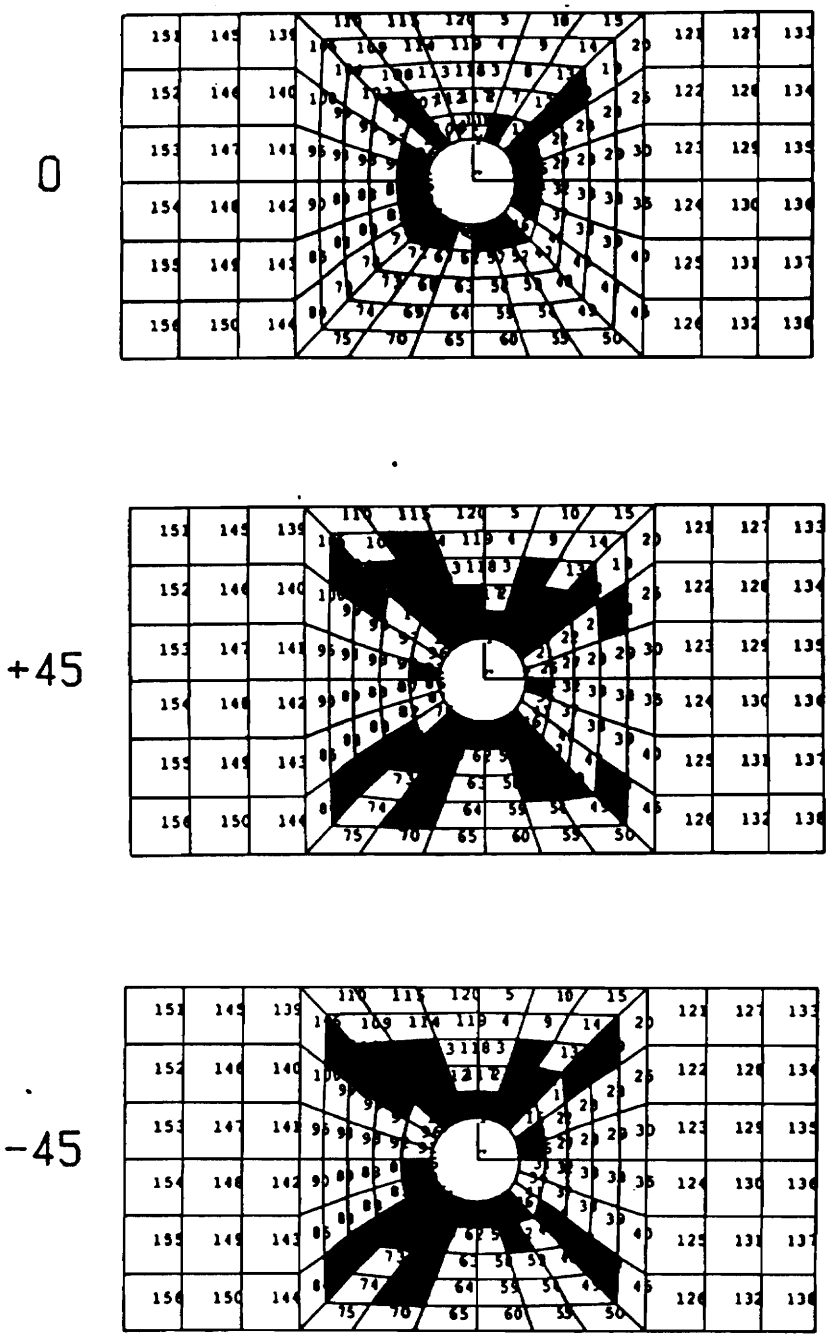

Figure 7.14 Damage Maps for Cyclic Loading at 77% of UTS after 50,000 Cycles.

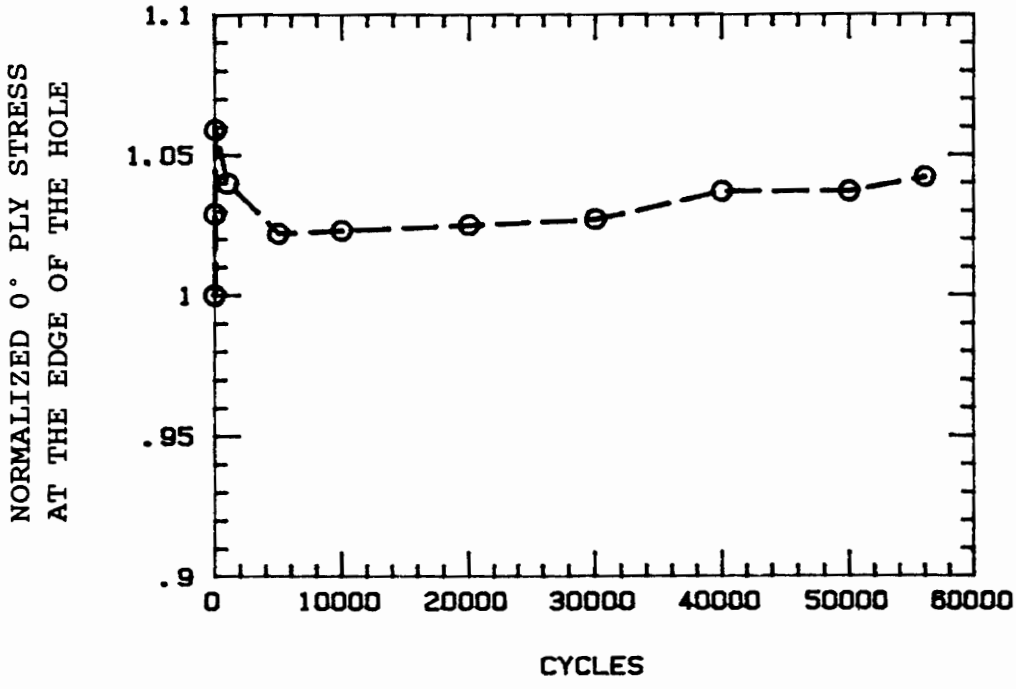

Figure 7.15 Change In the Normalized 0° Ply Stress at the Edge of the Hole Throughout the Predicted Life.

of the hole for the undamaged laminate. Evaluation of Figure 7.15 indicates a 6% increase in the stress in the 0° plies. This increase is due to localized failure of the ±45 plies and the load redistribution from the failed plies to the 0° plies. After this initial increase, the stress in the 0° plies decreases in the first 10,000 cycles. The reduction in the stress shown is the result of a reduction in the stress concentration factor around the hole due to damage development. Subsequent damage development between 10,000 and 56,100 cycles produces little change in the stress concentration factor at the edge of the hole. However, the increased damage in the ±45° plies continues to redistribute load into the 0° plies as evidenced by the slight increase in the stress shown in Figure 7.15.

Evaluation of the cyclic loading results indicates a combination of some expected and some questionable results. On one hand, the predicted damage patterns agree very well with expected results. Very early in the load histories, we predict failures in the 45° plies and splitting in the 0° plies. As the failure progresses, we predict the development of the butterfly damage pattern around the hole, which is typical of laminates with 45° plies. On the other hand, we do not predict fiber failures in the 45° plies extending from the edge of the hole. As a result,

the stress concentration factor at the hole does not decrease as we expected.

One possible source of this error is in the way in which shear failures were modeled. In these models, we treat a shear failure in the same manner as a transverse failure by primarily reducing the shear and transverse stiffness. However, shear failure can also be accompanied by fiber failure, and this type of failure mode is not addressed in the model. Unfortunately, the modeling of shear failures within a laminate is an extremely complex task which is beyond the scope of work for this program. Nevertheless, it is a task which needs to be addressed in order to accurately model damage development in complex components on a local level.

7.6 Discussion of the Modeling Approach

In the development of this type of modeling approach, two classes of problem areas arose. The first class of problem areas deals with the material considerations, and the second class involves mechanics issues. In the case of injection molded components, the material considerations such as material properties and fiber orientations dominated. Throughout the entire program, we lacked a good set of material properties due to the limited availability of material. The properties we did have were primary based

on data provided by UTRC and were taken from either hot-pressed chopped molding compound, hot pressed graphite paper and glass, or injection molded specimens with a random fiber orientation. The applicability of these properties to the injection molded tubes with fairly well-defined local fiber orientations is certainly suspect. In addition, the in-plane transverse and shear strengths were based on specimens dominated by through-the-thickness properties. As a result, it is difficult to determine if the lack of correlation between the predicted and the experimental results is due to the modeling approach or the material properties used in the model.

Similarly, the limited ability to determine fiber orientations could be another source of large errors. Although the radiographs give an excellent indication of the global trends in the fiber orientations, the local fiber orientations for most of the specimen were extremely difficult, and sometimes impossible to accurately quantify. For a large number of the elements, we could not identify a distinct fiber orientation and therefore, had to assume an orientation based on the neighboring elements. Secondly, several elements had more than one apparent fiber orientation, and we simply noted the dominate orientation. Lastly and probably most importantly, the radiographs were limited to the in-plane fiber swirling. The out-of-plane fiber swirling was not indicated and not modeled.

Unfortunately, this out-of-plane swirling greatly influenced the failure mode of the specimen as described in the previous chapter.

As an alternative to reading the fiber orientations from a radiograph, we could couple the damage development analysis with an injection molding analysis for chopped fiber reinforced components. A good three-dimensional analysis of the injection molded tube may also predict the out-of-plane fiber swirling in addition to the in-plane swirling. The output of the injection molding analysis would provide the fiber orientations required for the damage development analysis. In addition, since the fiber orientations would be analytically determined, we can completely investigate the performance of the part prior to fabrication and, therefore, use the damage development analysis as a design tool.

For the layered composites with continuous fiber reinforcement, most of the above material concerns are eliminated. As a result, the complexity of the problem is severely reduced, and we believe the predicted and experimental results would begin to correlate very nicely. Nevertheless, some mechanistic issues, such as the handling of shear failures described earlier, may still need to be addressed.

If these problems can be resolved, the model can be easily expanded to investigate a multitude of very complex

situations. Based on the power of the finite elements and number crunching capabilities of modern computers, we can easily extend the method to complex components such as nozzles, curved plates, turbine blades, attachments and so on. We can also investigate a wide variety of complex loadings including thermal gradients and shocks.

With a little bit of ingenuity, we can model other failure modes such as delaminations. For example, rather than using one brick element through the thickness, we can divide the laminate into sub-laminates were delamination is most likely to occur and use one brick element per sub-laminate. The sub-laminates can then be joined with coupled nodes. When delamination is predicted, we can uncouple the nodes. Another, more sophisticated, alternative would be to connect the sub-laminates with gap elements that initially have tensile and compressive stiffness. If we predict delamination, we can then modify the gap element to only have compressive stiffness.

With this type of modeling approach, we can then begin to thoroughly investigate the effects of damage development in complex engineering structures. These investigations will be based on good, sound principles of mechanics without correlation parameters and phenomological models. In addition, the analysis is built entirely on ply property information which should be consistent from one structure to another and readily available in the laboratory. In

summary, this type of model will enable the engineer to analytically predict the performance of a complex engineering structure which may experience large amounts of damage without the need for full-scale component testing.

8.0 SUMMARY AND CONCLUSIONS

This dissertation is the culmination of a three year research program on the properties and performance of ceramic composite components. The program was a pioneering effort into the characterization and modeling of complex components. As a result, we were required to perform a broad-based investigation into areas such as specimen design, test facility development, test method development, and analytical model development. All of these areas required careful research and a fair amount of trial and error to extend the field beyond the limited characterization and modeling of laboratory coupons.

Very early in the program, we established a well-defined set of specific objectives. All of these objectives have been met and, in most cases, exceeded. A test specimen representing a complex, ceramic composite component has been designed and fabricated. As a visual result of this research effort, a biaxial test facility has been constructed and demonstrated. The test frame is equipped with hydraulic grips capable of the precision alignment required for the successful testing of CMC's. In addition, the entire facility is integrated with a digital computer for test control and data acquisition. Once equipped with the high temperature furnace and the capacitance extensometer, Virginia Tech will possess the

only facility in the country capable of multiaxial testing of CMC's at elevated temperatures.

Throughout this program, we were required to develop destructive and nondestructive test methods for CMC's which provide accurate, repeatable, and meaningful results with a minimum of difficulty. In all cases, the developed test methods are based upon existing practices and have been extended to a complex, ceramic matrix composite engineering component.

The experimental program has identified several interesting capabilities and limitations of the selected material system. The critical, performance limiting defect in the specimens is the fiber swirling in the downstream transition region resulting from the injection molding process used to manufacture the CMC tubes. If we can eliminate this problem by a modification in the specimen design or fabrication process, we can increase the performance of the specimens beyond their current limitations. In spite of the current limitations, the fatigue performance of the specimens was much better than we expected, and the wear-in phenomenon exhibit by the high cyclic load specimen was fascinating.

The analytical modeling portion of the program was both very encouraging and disappointing at the same time. We set out to develop a strength prediction model for the injection molded components and ended up with a general

approach for the prediction of damage development in complex engineering components subjected to complex loadings. The approach successfully predicted the damage development patterns in both the injection molded CMC tube and the notched, thermoplastic matrix composite plate. In addition, the modeling effort has identified the need for generalized analysis techniques applicable to complex, injection molded, composite components with nonuniform fiber distributions and orientations. Unfortunately, the complete verification and application of this approach is well beyond the scope of this work and probably could involve several dissertations. As a result, we had to accept the disappointing fact that the verification of this modelling approach will be left to future research programs.

Although we have accomplished the objectives originally developed for this program, we have identified several areas which require additional research. If injection molding of complex geometry, CMC components is be a viable manufacturing process, we need to be able to predict and eventually eliminate the fiber swirling. In parallel, we need to develop processes to fabricate continuously reinforced CMC's into complex engineering components. Hot pressing works well for laboratory coupons. However, the engineering community requires more complex shapes than flat panels.

In the areas of test facility development and test method development, the next logical step is to extend the methods developed in this program to elevated temperature conditions. The two areas which need the most work are high temperature extensometry and in-situ NDE. The extensometry issues may be resolved with the capacitance extensometer; but in-situ NDE is a very complex issue which will probably require years of research. In addition, the through the thickness variations in injection molded components need to be nondestructively identified and characterized.

Although the glass material with chopped fiber reinforcement is not a highly desirable material for very high temperature applications, the limited testing in this program identified some behavioral aspects which could provide the incentive for future materials development programs. If we could identify the damage mechanism which produces the wear-in phenomenon, we may be able to determine methods to improve the performance of this and other brittle matrix composites.

The final area of future research is the application and verification of the damage development modeling approach. The natural step in this process is to apply the model to a polymeric composite such as presented in Section 7.5 and then to experimentally verify the results. Once the technique has been proven on the relatively simple case

of a plate with a center notch, we can then apply the method to a much more complex component such a nozzle with flanges, cutouts, and complex loadings.

Overall, this program has been a pioneering effort in the area of mechanical performance of ceramic composite components. Throughout the entire program, we have tried to keep focused on the idea of complex components as opposed to laboratory coupons. As a result, many of the concepts and methods developed in this program are directed towards engineering applications, as opposed to pure scientific research. However, as the art and science associated with the application of ceramic composites continues to develop, these types of programs are essential to transitioning from properties of materials to the performance of engineering components.

9.0 REFERENCES

1. ASTM D 3039 - 76; "Standard Test Method for Tensile Properties of Fiber-Resin Composites", 1989 Annual Book of ASTM Standards, Vol 15.03; pp. 117-121.

2. Brennan, J. J. and Prewo, K. M.; "Silicon Carbide Firbre Reinforced Glass-ceramic Matrix Composites Exhibiting High Strength and Toughness", Journal of Materials Science, Vol. 17; 1982; pp. 2371-2383.

3. Prewo, K. M., Brennan, J. J., and Layden, G. K.; "Fiber Reinforced Glasses and Glass-Ceramics for High Perfromance Applications", Ceramic Bulletin, Vol. 65, No. 2; 1986; pp. 305-313.

4. Singh, R. N. and Gaddipati, A. R.; "Mechanical Properties of a Uniaxially Reinforced Mullite-Silicon Carbide Composite", Journal of the American Ceramic Society, Vol. 71, No. 2; 1988; pp. C100-C103.

5. Wang, A. S. D. and Barsoum, M.; "Matrix Cracking Initiation in Brittle-Matrix Composites - Experiment and Predictions", Symposium on High Temperature Composites - Proceedings of the American Society for Composites; Dayton, Ohio; June, 1989; pp. 166-175.

6. Harris, J. N. et. al.; "GT-1 Development of Advanced Fiber Reinforced Ceramics", Fossil Energy Materials Program - Semiannual Progress Report for the Period Ending March 31, 1989; July, 1989; pp. 53-64.

7. Sterret, S. S.; Presentation at the Annual Review for the Mechanical Behavior of Composites at Elevated

Temperatures, Wright Patterson Air Force Base; Dayton, Ohio; August 29, 1989.

8. Bartolotta, P. A., Brindley, P. K., and Ellis, J. R.; "Verification of High-Temperature Structural Analysis Procedures", Proceedings of the HITEMP Review; Cleveland, Ohio; November, 1988; pp. 399-415.

9. Holmes, J. W., Kotil, T., and Foulds, W. T.; "High Temperature Fatigue of SiC Fiber-Reinforced Si_3N_4 Ceramic Composites", Symposium on High Temperature Composites - Proceedings of the American Society for Composites; Dayton, Ohio; June, 1989; pp. 176-186.

10. Hartman, G. A., Zawada, L. P., and Russ, S. M.; "Techniques for Elevated Temperature Testing of Advanced Ceramic Composite Materials", Proceedings of the 5th Conference on Testing in Hostile Environments - Society of Experimental Mechanics; Costa Mesa California; March 1988; pp. 31-38.

11. Phillips, D . C. and Davidge, R. W., "Test Techniques for the Mechanical Properties of Ceramic Matrix Fibre Composites", Transactions and Journal of the British Ceramic Society, Vol. 85; 1986; pp. 123-130

12. Castelli, M. G., et.al.; "Development of Thermomechanical Testing Techniques for Advanced Composites", Proceedings of the 2nd Annual HITEMP Review; Cleveland, Ohio; October 31 - November 2, 1989; pp. 43-1 to 43-14.

13. Kotil, T. and Holmes, J. W., "A Technique for Measuring High-Frequency Elevated Temperature Fatigue Strains in Ceramic Composites", to be published.

14. Larsen, D. C., Stuchly, S. L. and Adams, J. W., Evaluation of Ceramics and Ceramic Composites for Turbine Engine Applications, AFWAL-TR-88-4202; December, 1988.

15. Ellis, R. and Gayda, J.; "Test Methods Overview", Proceedings of the 2nd Annual HITEMP Review; Cleveland, Ohio; October 31 - November 2, 1989; pp. 11-1 to 11-14.

16. Stinchcomb, W. W. (Editor); Mechanics of Nondestructive Testing; Plenum Press, New York, 1980.

17. Tsangarakis, N., Gruber, J. J. and Nunes, J.; "Non-destructive Evaluation of Fatigue Damage in Alumina Fiber Reinforced Aluminum", Journal of Composite Materials, Vol 19; May, 1985; pp. 251-268.

18. Klima, S. J.; "Nde of Advanced Ceramics", Materials Evaluation, Vol. 44; April, 1986; pp. 571-576.

19. Klima, S. J., Baaklini, G. Y. and Abel, P. B.; Nondesrtuctive Evaluation of Structural Ceramics, NASA-TN-88978; 1987.

20. Ellingson, W. A., et.al.; Recent Developments in Nondestructive Evaluation for Structural Ceramics, ANL/FE-87-2; Argonne National Laboratory; Argonne, IL; May, 1987.

21. Walter, J. B., and Lott, L. A. "Nondestructive Evaluation of Advanced Cermic Composite Materials", Proceedings of the Fossil Energy Materials Conference, ORNL/FMP-87/4; Oak Ridge, TN; August, 1987.

22. Faudree, M., et. al.; "Characterization of Damage and Fracture Processes in Short Fiber BMC Composites by Acoustic Emission", Journal of Composite Materials, Vol 22; December, 1988; pp. 1170-1195.

23. Larsen, D. C., Stuchly, S. L. and Adams, J. W., Evaluation of Ceramics and Ceramic Composites for Turbine Engine Applications, AFWAL-TR-88-4202; December, 1988.

24. Pepper, R. W. and Shahood, T. W.; "Correlation of NDE Results on Metal/Matrix and 2-D Carbon-Carbon Composites", Symposium on High Temperature Composites - Proceedings of the American Society for Composites; Dayton, Ohio; June, 1989; pp. 223-232.

25. Williams, J. H., Sampson S. L. and Wang, T. K.; "Quantitative Nondestructive Evaluation of Automotive Glass Fiber Composites", Journal of Composite Materials, Vol. 16; 1982; pp. 20-39.

26. Vipond, R. and Daniels, C. J.; "Nondestructive examination of Short Carbon Fibre-reinforced Injection Molded Thermoplastics", Composites, Vol. 16, No. 1; January, 1985; pp. 14-18.

27. Ellingson, W. A., et. al.; "ANL-1 - Development of Nondestructive Evaluation Methods for and Effects of Flaws on the Fracture Behavior of Structural Ceramics",

Fossil Energy Materials Program - Semiannual Progress Report for the Period Ending March 31, 1989, ORNL/FMP-89/1; July, 1989; pp. 11-33.

28. Kautz, H. E. and Klima, S. J.; "NDE of Ceramic Matrix Composites", Proceedings of the 2nd Annual HITEMP Review; Cleveland, Ohio; October 31 - November 2, 1989; pp. 42-1 to 42-11.

29. Minford, E. and Prewo, K. M.; "Fatigue Behavior of Silicon Carbide Fiber Reinforced Lithium-Alumino-Silicate Glass-Ceramics", Tailoring Muliphase and Composite Ceramics - Proceedings of the Twenty-first University Conference on Ceramic Science; Pensylvania State University, University Park, PA; July 1985; pp. 561-570.

30. Prewo, K. M.; "Fatigue and Stress Rupture of Silicon Carbide Fibre-Reinforced Glass-Ceramics", Journal of Materials Science, Vol. 22; 1987; pp. 2695-2701.

31. Wang, S. S., Chim, E. S.-M. and Zahlan, N. M.; "Fatigue Crack Propagation in Random Short-Fiber SMC Composite", Journal of Composite Materials, Vol. 17; May, 1983; pp. 250-266.

32. Wang, S. S., Goetz, D. P. and Corten, H. T.; "Shear Fatigue Degradation and Fracture of Random Short-Fiber SMC Composite", Journal of Composite Materials, Vol. 18; January, 1984; pp. 2-20.

33. Freidrich, K., et.al.; "Fatigue Behavior of Aligned Short Carbon-Fibre Reinforced Polyimide an

Polyethersulphone Composites", Journal of Materials Science, Vol 20; 1985; pp. 3353-3364.

34. Freeman, R. B.; "Shear Fatigue Evaluation of SMC"; Proceedings of the 42nd Annual Conference, Composites Institute, The society of the Plastics Industry, Inc; February 206, 1987; pp. 1-5 of Session 11-B.

35. Wang, S. S., Suemasu, H. and Chim, E. S. M.; "Analysis of Fatigue Damage Evolution and Associated Anistotropic Elastic Property Degradation in Random Short-Fiber Composite", Journal of Composite Materials, Vol. 21; December, 1987; pp. 1084-1105.

36. Wang, S. S. and Chim, E. S. M.; "Fatigue Damage and Degradation in Random Short-Fiber SMC Composite", Journal of Composite Materials, Vol. 17; March, 1983; pp. 114-134.

37. Lang, R. W., Manson, J. A. and Hetrzberg, R. W.; "Mechanisms of Fatigue Fracture in Short Glass Fibre-Reinforced Polymers", Journal of Materials Science, Vol. 22; 1987; pp. 4015-4030.

38. Hahn, H. T.; "On Approximations for Strength of Random Short Fiber Composites", Journal of Composite Materials, Vol. 9; October, 1975; pp. 316-326.

39. Fukuda, H. and Chou, T.; "A Probabilistic Theory for the Strength of Short Fibre Composites", Journal of Materials Science, Vol 16; 1981; pp. 1088-1096.

40. Hedgepeth, J. M.; Stress Concentrations in Filamentary Structures, NASA TN-D882; Langley Research Center, Hampton VA; 1961.

41. Hedgepeth, J. M. and Van Dyke, P.; "Local Stress Concentrations in Imperfect Filamentary Composite Materials", Journal of Composite Materials, Vol. 1; 1967; pp. 294-309.

42. Fukuda, H. and Chou, T.; "Stiffness and Strength of Short Fibre Composites as Affected by Cracks and Plasticity", Fibre Science and Technology; 1981; pp 243-256.

43. Manders, P. W. and Chou, T. W.; "The Strength of Aligned Short-Fiber Carbon, Glass and Hybrid Carbon/Glass Composites", Progress in Science and Engineering of Composites ICCM-IV; Tokyo, Japan; 1986; pp. 1075-1082.

44. Sanadi, A. R. and Piggott, M. R.; "Interfacial effects in Carbon-Epoxies. Part 1: Strength and Modududls with Short Aligned Fibres", Journal of Materials Science, Vol. 20; 1985; pp. 421-430.

45. Sanadi, A. R. and Piggott, M. R.; "Interfacial effects in Carbon-Epoxies. Part 1: Strength and Modududls with Short Random Fibres", Journal of Materials Science, Vol. 20; 1985; pp. 431-437.

46. Wang, S. S., et. al.; "Fracture of Random Short-Fiber SMC Composite", Journal of Composite Materials, Vol. 17; July, 1983; pp. 299-315.

47. Kageyama, K. and Chou, T.; "Modeling and Analysis of Fracture Toughness of Short-Fiber Reinforced Ceramic-Matrix Composites", 6th International Conference on Composite Materials ICCM-VI; London; 1987; pp. 2.60-2.69.

48. ANSYS PC-Linear Finite Element Code, Revision 4.3; Swanson Analysis Systems, Incorporated; 1988.

49. Hyer, M. W.; "Hydrostatic Response of Thick Laminated Composite Cylinders", Journal of Reinforced Plastics and Composites, Volume 7, July 1988; pp 321-340.

50. Dunyak, T. J., Reifsnider, K. L., and Stinchcomb, W. W.; An Examination of Selected NDE Methods for Ceramic Composite Tubes, ORNL/Sub/87-SA946/01, Virginia Polytechnic Institute and State University; Blacksburg, VA; April, 1990.

51. Marshall, D. B. and A. G. Evans; "Failure Mechanisms in Ceramic-Fiber/Ceramic-Matrix Composites", Journal of the American Ceramic Society, Volume 68, Number 5, May 1985; pp 225-231.

52. Bakis, C. E.; "Fatigue Response of Notched Composite Laminates Subjected to Tension-Compression Loading," Master of Science, Virginia Polytechnic Institute and State University; October 1984.

53. "ASTM Designation: E 1012-89 Standard Practice For Verification of Specimen Alignment Under Tensile Loading", Annual Book of ASTM Standards American Society for Testing and Materials, Vol 03.01; April 1989; pp 770-776.

54. Ansys 4.4 Finite Element Code, Revision 4.4; Swanson Analysis Systems, Incorporated; 1989.

55. Ansys 4.4 Theoretical Manual; Swanson Analysis Systems, Incorporated; 1989.

56. Osiroff, R.; Damorheaology: Creep-Fatigue Interaction in Composite Materials; A Dissertation Submitted to the Faculty of Virginia Polytechnic Institute and State University, Blacksburg Virginia; June 1990.

10.0 Appendix: Test Facility Specifications

The multiaxial test facility was designed and built by the Instron Corporation for high temperature testing. The servo-hydraulic facility is uniquely suited for axial-torsion testing of ceramic matrix composite tubes at temperatures up to 1500°C. Features of the facility include:

- Instron S2-7858 high stiffness, axial/torsional load frame with load capacities of 100 kip axial and 50 in/kips torsional. The stiffness of the frame is rated at 5.0×10^6 lbs/in axial and 3.8×10^6 in-lbs/deg torsional at 40 inches separation between crosshead and baseplate.

- Top mounted, high stiffness, axial/rotary actuator load rated at 50 kips axial and 25 kip-in torsional.

- Biaxial load cell rated at 50 kip axial and 25 kip-in torsional.

- Six channel servo-controller provides options for axial load, strain or stroke control and rotary torque, strain, or angular displacement control. Control mode, range, selection, and range change can be set while system is in operation.

- Digital readout of all channel signals.

- Multiple waveform function generator with frequency range between DC and 1000 Hz.

- Intelligent computer/test system interface incorporating a general purpose interface bus.

- PC computer (IBM and Hewlett Packard) compatible software for machine operation and control, data storage, and data post-processing.

- On-line PC computer: Hewlett Packard Vectra with color monitor, printer, and math coprocessor.

- High Temperature furnace: short furnace design with Kanthal elements rated at 2730°F maximum temperature.

- Specially designed axial/torsion hydraulic grips for gripping ceramic tubes based on the existing Instron design for high temperature ceramic rods.

- High temperature, axial extensometer to be upgraded to provide axial/torsional capability.

VITA

Thomas John Dunyak was born on March 23, 1959 in Morgantown, West Virginia and spent most of his childhood in Bethel Park, Pennsylvania. In 1977, he graduated from Bethel Park Senior High School and enrolled in the College of Engineering at Virginia Tech. Mr. Dunyak earned an BS in Engineering Science and Mechanics in 1981 and a MS in Engineering Mechanics in 1983. After his masters program, he worked in the Structural Mechanics Group at the Westinghouse Advanced Energy Systems Division. Mr. Dunyak left Westinghouse in September of 1987 and returned to the Engineering Mechanics Department at Virginia Tech as a PhD candidate.

Mr. Dunyak married Terri Cehelnik in 1984 and has two daughters, Ashley born in 1985, and Marissa born in 1990.